# Thin Film Annular Flow: Nucleate Boiling and Obstruction Wake Dryout

by

Joseph Farrell

A dissertation submitted in partial fulfillment of

the requirements for the degree of

Master of Science

(Mechanical Engineering)

at the

UNIVERSITY OF WISCONSIN-MADISON

2025

Date of final oral examination: April 30, 2025

The dissertation is approved by the following members of the Defense Committee:
Allison J. Mahvi, Assistant Professor, Mechanical Engineering
Arganthaël Berson, Assistant Teaching Professor, Mechanical Engineering
Gregory F. Nellis, Professor, Mechanical Engineering

*Dedicated to Mom and Dad*

# ACKNOWLEDGMENTS

I would like to thank my committee members Professors Allison Mahvi, Arganthaël Berson, and Greg Nellis. There's a lot of information to go through here, but I hope you find it as interesting as I do. A particular thanks goes to my co-advisors Allison and Arganthaël. Our weekly discussions have been truly invaluable, and I am constantly grateful. I've learned a lot in just two years, and everything is supported by you both.

Jason and Roman, I could not have asked for better mentors to introduce me to the lab. Everything in this thesis is truly built off the back of your hard work and knowledge. Jason, it feels like you've built the base of everything I use daily, and your codebase taught me everything I now know about MATLAB. Roman, your enthusiasm for and knowledge of annular flow is contagious, our calls always help me realize that my data is actually pretty cool.

Thank you to all the students in the LET+S Lab for being the first to hear about my data. Verbalizing my thoughts to you all has been an invaluable way of getting everything in my brain into a somewhat logical argument. Everything I've presented has first been filtered by your thoughtful feedback. I've also been lucky to work with fantastic undergraduate students Alec and Megan. Alec, helping with the loop rebuild, reorganizing the LabView, and the other many, many tasks you've been around to do have all been a huge help. Megan, I'm very excited to have the falling film facility up and running again thanks to you.

I would also like to acknowledge the Naval Nuclear Laboratory and Evan Hurlburt for constantly supporting this project and trusting me to add to its legacy.

Everything shown below is a combination of the hands and minds of many people. Thank you to everyone I've been lucky enough to meet and work with.

## ABSTRACT

Nucleate boiling in thin film annular flow is a complex phenomenon that many energy systems utilize and a variety of heat transfer mechanisms influence. While the fundamentals are rooted in the comparatively well-understood fields of pool and flow boiling, thin film flow boiling introduces additional challenges that make the heat transfer behavior hard to predict. Considering this, we analyze the foundational aspects of nucleate boiling and examine how flow parameters – such as liquid film thickness, system pressure, surface tension, channel geometry, mass flow rate, and applied heat flux – affect the intensity of nucleate boiling in thin annular films. Additionally, recent research identifies disturbance waves as a significant factor in enhancing bubble nucleation, yet the underlying mechanisms driving this phenomenon remain undefined. Therefore, the insights and deficiencies of three theories seeking to explain wave-based nucleation are extensively considered. Furthermore, this work investigates the effect of obstructions under annular two-phase flow conditions flowing through a vertical, upward channel. We characterize the flow around a large (D=2.5 mm) and a small (D=1.25 mm) cylindrical obstruction in direct contact with the heated wall, tested with two different diameters, using high-speed video, temperature measurements, and optically based liquid film thickness measurements. The experiments investigate the flow phenomena over a range of operating conditions from those conducive to nucleate boiling and to those where nucleate boiling is fully suppressed. The results indicate that the obstruction induces sustained film dryout with the size, shape, and number of dryout areas dependent on flow conditions. Additionally, dryout in the wake does not always yield a severe reduction in heat transfer coefficient.

# TABLE OF CONTENTS

# LIST OF TABLES

# LIST OF FIGURES

# LIST OF SYMBOLS AND ABBREVIATIONS

| Nomenclature |
|---|
| $A_c = Tube\ cross\ sectional\ area$ |
| $b = Height\ of\ bubble\ nucleus$ |
| $Bo = Boiling\ number$ |
| $c_p = Specific\ heat\ capacity\ at\ constant\ pressure$ |
| $c_{pixel} = Pixel\ to\ [m]\ scaling\ factor$ |
| $Co = Convection\ number$ |
| $D = Channel\ diameter$ |
| $D_b = Bubble\ diameter$ |
| $D_h = Hydraulic\ diameter$ |
| $D_i = Inner\ tube\ diameter$ |
| $D_{obs} = Obstruction\ diameter$ |
| $e = Entrainmed\ liquid\ fraction$ |
| $F = Reynolds\ factor$ |
| $F_{fl} = Kandlikar\ fluid\ surface\ parameter$ |
| $Fr = Froude\ Number$ |
| $g = Gravity$ |
| $G = Mass\ flux$ |
| $h = Heat\ transfer\ coefficient$ |
| $h_{fg} = Latent\ heat\ of\ vaporization$ |
| $j = Superficial\ velocity$ |
| $k\ = Thermal\ conductivity$ |
| $L_{cond} = Conduction\ Lenth$ |
| $M = Molecular\ weight$ |
| $Nu = Nusselt\ number$ |
| $P = Pressure$ |
| $Pr = Prandtl\ number$ |
| $\Delta P_{sat} = P_{sat}(T_w) - P$ |
| $q'' = Heat\ flux$ |
| $R = Light\ ring\ radius$ |
| $r_b = Bubble\ radius$ |
| $r_c = Radius\ of\ cavity\ mouth$ |

$R''_{cond} = Conduction\ resistance\ per\ unit\ area$

$Re = Reynolds\ number$

$S = Suppression\ factor$

$T = Temperature$

$T_{le} = Local\ equivalent\ saturation\ temperature$

$\Delta T_{sat} = T_w - T_{sat}$

$u = Velocity$

$We = Weber\ number$

$x = Local\ vapor\ quality$

$y = Distance\ from\ heating\ surface$

## Greek Symbols

$\delta = Instantaneous\ liquid\ film\ thickness$

$\bar{\delta} = Time - averaged\ liquid\ film\ thickness$

$\delta_{TL} = Limiting\ thermal - layer\ thickness$

$\eta = \dfrac{\delta_{TL} - y}{\delta_{TL}}$

$\theta = T - T_\infty$

$\theta_{crit} = Angle\ of\ total\ internal\ reflection$

$\theta_w = T_w - T_\infty\ at\ incipience\ of\ boiling$

$\mu = Dynamic\ viscosity$

$\Pi = Perimeter$

$\rho = Density$

$\sigma = Surface\ tension$

$\sigma = Standard\ deviation$

$\varphi = Angle\ of\ bubble\ wall\ with\ respect\ to\ the\ horizontal$

## Subscripts

$b = Of\ the\ bubble$

$CB = Convective\ boiling$

$cr = Critical$

$Dry = Of\ the\ dry\ test\ section$

$eff = Effective$

$ext = Measured\ on\ the\ exterior$

$f = Fluid$

$g = Gas$

$in = At\ the\ test\ section\ inlet$

$l\ = Liquid$

$lf = Liquid\ film$

$lo\ = For\ saturated\ liquid\ flow$

$NB = Nucleate\ boiling$

$NBD = Nucleate\ boiling\ dominant$

$sat = Saturation\ properties$

$up = Upstream\ of\ obstruction$

$v = Vapor$

$w = Heated\ surface$

$\infty = Bulk$

# CHAPTER 1: INTRODUCTION

## 1. Annular Two-Phase Flow

In the introduction of their textbook, Hewitt and Hall-Taylor state, "It will be seen from this discussion that the annular flow regime occupies an extremely important place in two-phase flow systems, probably more important than any other flow pattern" [1]. In many flow boiling systems, the working fluid is progressively vaporized as it flows along the heated channel. The flow transitions from a single-phase liquid, through intermediate regimes, eventually reaching annular two-phase flow. This regime is characterized by a thin liquid film along the channel walls with a vapor core containing entrained liquid droplets [1]. Due to its association with high heat transfer coefficients and its proximity to dryout type critical heat flux (CHF) – a potentially dangerous flow regime that results in a sudden drop in heat transfer coefficient – many groups have studied the annular forced convective evaporation regime depicted in Fig. 1 [2]. Similarly, there has been significant past work on subcooled and saturated nucleate boiling, along with the transition to film boiling, where a vapor layer separates the heated wall from the liquid coolant.
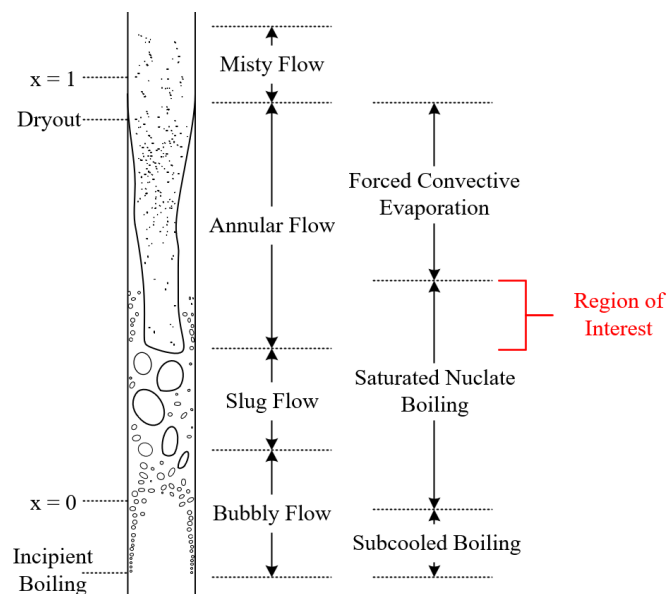
**Fig. 1:** Two-phase flow and boiling regimes for a vertical pipe adapted from [3]

Few studies have focused on the transition between saturated nucleate boiling and forced convective evaporation. Consequently, the location and heat transfer characteristics of this transitional region are underexplored despite their relevance to the failure mechanism in flow boiling systems. *Chapter 3* serves to explain the mechanics of thin film nucleate flow boiling with particular attention paid to how flow parameters influence the intensity of boiling. *Chapter 4* then demonstrates limited thin film nucleate boiling made possible by facility upgrades directed by the information presented in *Chapter 3*.

In the forced convective evaporation regime, the two-phase mixture may transition from the annular to the intermittent dryout regime with applied heat flux [4]. The loss of the liquid film on the heated surface significantly reduces wall heat transfer, resulting in a sharp rise in wall temperature, marking CHF [1]. Traditionally, CHF is considered a singular condition at which there is a severe reduction in heat transfer coefficient in association with the frequency of dryout events [5]. However, the data presented in *Chapters 5* and *6* introduce a complication: obstructed annular flow can exhibit a progressive reduction in HTC with increasing heat flux rather than a single critical threshold. Furthermore, dryout can be sustained locally without severe degradation in heat transfer performance. These findings suggest that existing CHF definitions may be inadequate for describing obstructed annular flow, and additional mechanisms must be considered.

## 2. Thin Film Nucleate Boiling

Nucleate boiling in a flowing system is usually observed near the entrance of the flow channel, where the intensity of vaporization governs the development of subsequent flow regimes. A typical progression of two-phase flow patterns is shown in Fig. 1. If the liquid is subcooled at the flow inlet, bubble nucleation will begin when the heat flux is high enough that the wall temperature is suitably above the fluid saturation temperature (sufficient superheat). Under certain

conditions, nucleated bubbles do not lift off from the heater surface, instead rapidly merging with neighboring nucleation sites. These large, coalesced vapor bubbles can prevent new liquid from reaching the cooling surface, creating a Departure from Nucleate Boiling type failure. Under other conditions, the bubbles may depart from the wall, coalescing in the middle of the flow channel, eventually yielding the annular flow pattern whose failure is determined by the progressive evaporation of the liquid film [3], [6], [7], [8]. In annular flow, the liquid film is cooled primarily by convective evaporation at the interface between the liquid film and the vapor core. If the heated surface is not adequately cooled by convective evaporation alone, phase change through bubble nucleation in the liquid film will persist into the annular regime [3]. However, if convective evaporation can remove enough superheat from the liquid film, bubble nucleation can be locally or systemically suppressed [3]. This transition between churn and annular flow contains a complex set of competing phenomena that promote or suppress nucleate boiling in the thin film. Understanding the physics that yields these flow transitions is critical for the design of heat transfer equipment for a range of applications, from chemical processing to nuclear power systems [9], [10].

Several reviews have addressed various aspects of flow boiling, including two-phase flow regime predictions [11], nucleate boiling heat transfer [12], [13], bubble dynamics in subcooled flow boiling [14], [15], churn [7] and mist (dryout) flow regimes [8], droplet entrainment in annular flow [16], [17], and the impact of surface modifications [18], [19]. No work, however, combines literature for nucleate boiling and annular flow. Nucleate boiling in thin films remains understudied, and current descriptions of the transition to evaporative boiling rely on fragmented experimental data. A recent holistic method, heat flux partitioning, evaluates individual heat transfer contributions in nucleate boiling, marking a shift from empirical to physics-based models

[20], [21]. *Chapter 3* expands on that approach by consolidating knowledge on nucleate boiling in thin films to support future modeling efforts.

**3. Obstructed Annular Flow**

Much of the foundational literature on CHF focuses on uninterrupted, straight channels, which has led to several correlations to predict CHF [22], [23], [24], [25], [26]. However, in many practical applications, the channel geometry or flow conditions diverge from their experimentally validated range. Recent efforts have aimed to create more flexible, widely applicable phenomenological models, yet these remain limited to unmarred flow channels [4], [9]. This work demonstrates that current CHF definitions fail to describe flow behavior when small obstacles (relative to the channel size) disrupt the liquid film. Given that field conditions seldom represent controlled experimental setups, the present work diversifies the academic database, providing a basis for further development of future physics-based models.

Single-phase flow around an obstruction can offer insights into obstructed annular flows. While not a perfect analogy, single-phase flow around objects in the flow field has been thoroughly studied. For objects in laminar flow, the flow field in the wake depends on the shape of the obstruction, the local Reynolds number, and the distance from the obstruction as seen in Fig. 2 [27]. After the boundary layers separate from the cylinder, swirling vortices interact with the free stream and diffuse by viscous action into the surrounding fluid [28]. The Navier-Stokes equations show that the boundary layers grow proportionally to the square root of the distance from the obstruction and that viscous interactions decrease the peak velocity deficit proportionally to the inverse of the square root of the distance from the obstruction [29].
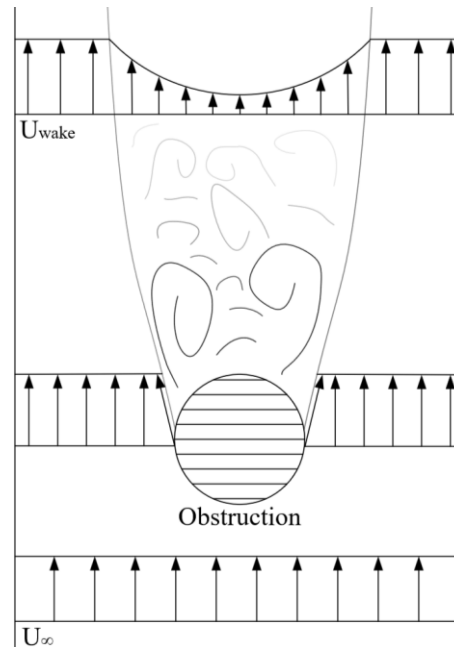
**Fig. 2:** Schematic of cylindrical obstruction-induced flow velocity deficit

The literature on obstructed annular flow predominately examines the effects of obstacles on CHF in nuclear applications, replicating reactor conditions such as pressure, mass flux, wall heat flux, and length scales. Zahlan explores the disruption of the liquid film by different obstacles (blunt and streamlined) in direct contact with the heated wall in a vertically oriented circular tube using HFC-134a as the coolant [30]. Zahlan observes that flow obstacles significantly decrease the film-boiling wall temperatures and push the location of CHF downstream. Ami et al. support Zahlan's conclusion, finding that the CHF increased due to the presence of an obstacle, tested using water with the obstacle oriented in the center of a vertical tube [31]. Additional studies into obstacles placed in the vapor core have reported an enhanced deposition rate of droplets from the vapor core stemming from increased turbulence [32]. Investigations of grid spacers have found that CHF does not occur downstream of the spacer due to liquid accumulation, increased droplet deposition rate, and easy rewetting of any dryout by disturbance waves [33], [34], [35]. The literature regarding obstructions in annular two-phase flow consistently reports performance

enhancements and delayed CHF due to flow obstructions. However, these experiments typically occur at mass fluxes, G, larger than the current experiments (G ≤ 170 kg/m²-s compared to G ≥ 500 kg/m²-s). It has been reported that at lower mass fluxes (G ≤ 1000 kg/m²-s) CHF enhancements due to flow obstacles disappear or become negative [36].

In addition to prior studies focused on nuclear applications, there is work on the impact of obstructions in gravity-driven thin film flow. In Stokes flow down an inclined plane, metastable dry arches form, where the shape of the liquid rim is determined by a balance between the liquid weight and surface tension [37], [38]. This arch shape aligns well with the wetted wake behind an obstruction in a gravity-driven thin film, and a single-phase wake (Fig. 2) [39]. Another common feature in simulations of gravity-driven thin film flow is the buildup of liquid film at the stagnation point of the obstruction and the formation of a trough immediately downstream of the obstruction [40], [41], [42], [43]. The size of the peak and trough is proportional to the obstacle size and inclination angle, with larger obstacles and steeper flows exaggerating changes in film thickness [43].

## 4. Research Questions

This thesis investigates two primary topics: what factors influence nucleate boiling in thin annular liquid films, and how a cylindrical obstruction affects dryout behavior in annular flow. *Chapter 3* summarizes the current state of the literature regarding nucleate boiling in thin liquid films, particularly those present in annular flow. After discussing the fundamentals of the boiling cycle and the complexities presented by annular flow, there is a deeper examination of how fluid properties and operating conditions impact bubble nucleation and how these relationships are used in correlations that predict the relative importance of nucleate boiling and film evaporation in annular flows. Additional complexities are introduced by considering the influence of flow

features specific to thin films such as disturbance waves. Insights from this review guided modifications to the experimental setup and allowed for the direct observation of annular flow nucleate boiling detailed in *Chapter 4*.

     *Chapter 5* shifts focus to the second research question, examining how an obstruction alters liquid film dynamics. A parametric study over a range of mass fluxes ($130 - 170$ kg/m$^2$-s), inlet vapor qualities ($0.63 - 0.95$), and two different diameter obstructions (1.25 and 2.5 mm) is used to identify deficiencies in the liquid film and the absence of disturbance waves in the obstruction wake. This information is then related to dryout incipience in the wake using the resultant wall temperature rise to report the wake heat transfer coefficient. *Chapter 6* integrates the findings from the previous chapters, combining observations of the liquid film behavior in the wake of obstructions from *Chapter 5* with the characteristics of liquid films that support nucleate boiling as discussed in *Chapters 3* and *4*. In doing this, we identify and create a preliminary model to predict the changes in obstruction wake dryout based on liquid film thickness and velocity.

# CHAPTER 2: EXPERIMENTAL FACILITY

## 1. Flow Loop Description

A schematic of the flow loop used for all data acquisition is shown in Fig. 3. The working fluid, R-245fa, is a low-pressure refrigerant selected for its similar surface tension and density ratio to high-pressure steam. Starting from the storage tank, the subcooled liquid refrigerant is split into two flow streams. The first flow path keeps the refrigerant in the liquid phase and pumps it to a mixing tee. In the second flow path, the refrigerant is vaporized and superheated before entering the mixing tee to produce a two-phase refrigerant flow at a desired mass flux and quality. The mixing tee was specifically designed to generate annular two-phase flow while minimizing entrainment by injecting the subcooled liquid into the vapor flow through small holes around the perimeter of the channel wall. After the tee, the two-phase mixture travels vertically upward into the development section to ensure a fully developed flow before transitioning smoothly into the measurement area [44]. Finally, the two-phase mixture is condensed back into the storage tank to complete the cycle.

The facility shown in Fig. 3 has been slightly modified from previous reports using this facility ([2], [4], [45], [46]) to allow for thicker liquid films to support nucleate boiling. A full description of the facility changes may be found in *Appendix A*. In brief, a PID controlled valve was installed on the chilled water side of the condenser to stabilize the saturation temperature when heating the liquid film. Additionally, a larger liquid-side pump was plumbed in parallel with the existing pump, using a three-way valve to direct the flow into a selected pump.
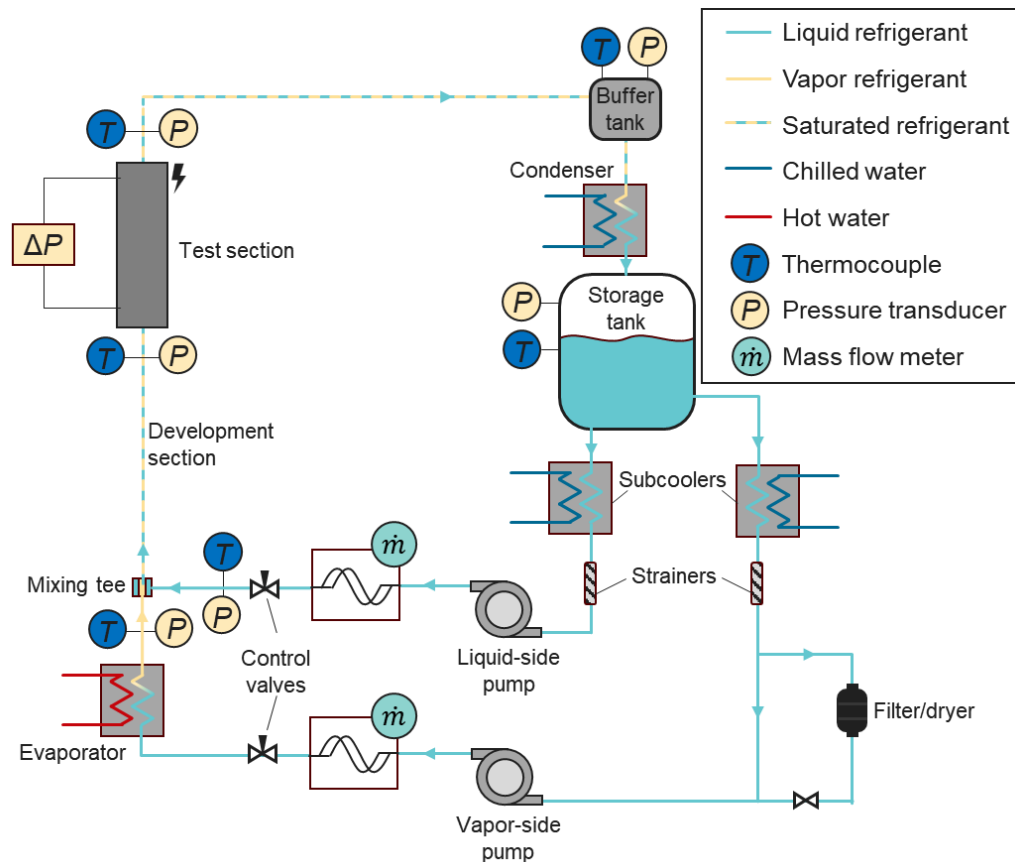
**Fig. 3:** Two-phase flow loop facility diagram

In the test section, thermocouples measure the external wall temperature, which allows extrapolation of the interior wall temperature. Pressure transducers provide both differential and absolute pressure readings. Liquid film thickness is measured non-invasively using the total internal reflectance method, recorded with high-speed video. High-speed imaging also captures dynamic film behavior, particularly during dryout events. A detailed description of the measurement techniques employed in the test section is provided in *Appendix G*, while Table 1 summarizes the associated measurement uncertainties.

**Table 1**: Maximum uncertainties of process measurements

| Parameter | Symbol | Uncertainty |
|---|---|---|
| Absolute pressure | $P$ | 0.25% |
| Mass flux | $G$ | 2.3% |
| Temperature | $T$ | 0.25 ˚C |
| Effective heat flux | $q''_{eff}$ | 1.5% |
| Inlet vapor quality | $x_{in}$ | 0.001 |
| Local quality | $x$ | 0.003 |
| Film thickness [45] | $\delta$ | 8.6 µm |
| Reynolds number [a] | $Re_{lf}$ | 2.2% |

[a]Reported as the maximum calculated error

## 2. Test Section

The test section is a 0.525 m long rectangular channel with a cross-sectional area of 36 mm x 12 mm, yielding a hydraulic diameter of 18 mm. The two wider walls of the test section are transparent glass windows coated with fluorine-doped tin oxide to allow for electrically controlled resistance heating of the inner surface of the walls. A thermal resistance model using temperature data gathered on the outside of the glass windows is used to calculate heat flux into the refrigerant and the HTC. More detail regarding the thermal resistance network and specifics of the flow loop can be found in Morse et al. [2]. Notably, the effective heat flux is the heat flux received by the two-phase flow accounting for environmental losses.

These experiments analyze the effect of a cylindrical obstruction on the flow. Two diameters were tested, the large cylinder had a diameter of 2.5 mm (6.94% of the channel width), and the small cylinder had a diameter of 1.25 mm (3.47% of the channel width). Fig. 4 (a) and (b)

show diagrams of the cylinder positioned in the flow. The obstruction support assembly was mounted to the outlet of the test section and designed to support the center of the obstacle approximately 420 mm downstream from the test section inlet. An obstacle was attached to a spring-loaded assembly to ensure no liquid traveled between the obstacle and the glass window. Tests were performed with the obstruction support but without the obstruction cylinder inserted and compared with data taken in the test section free of any obstructions or supports. This data can be seen in *Appendix D* and showed that the support system does not significantly impact flow behavior or dryout conditions for the operating conditions studied in this work.
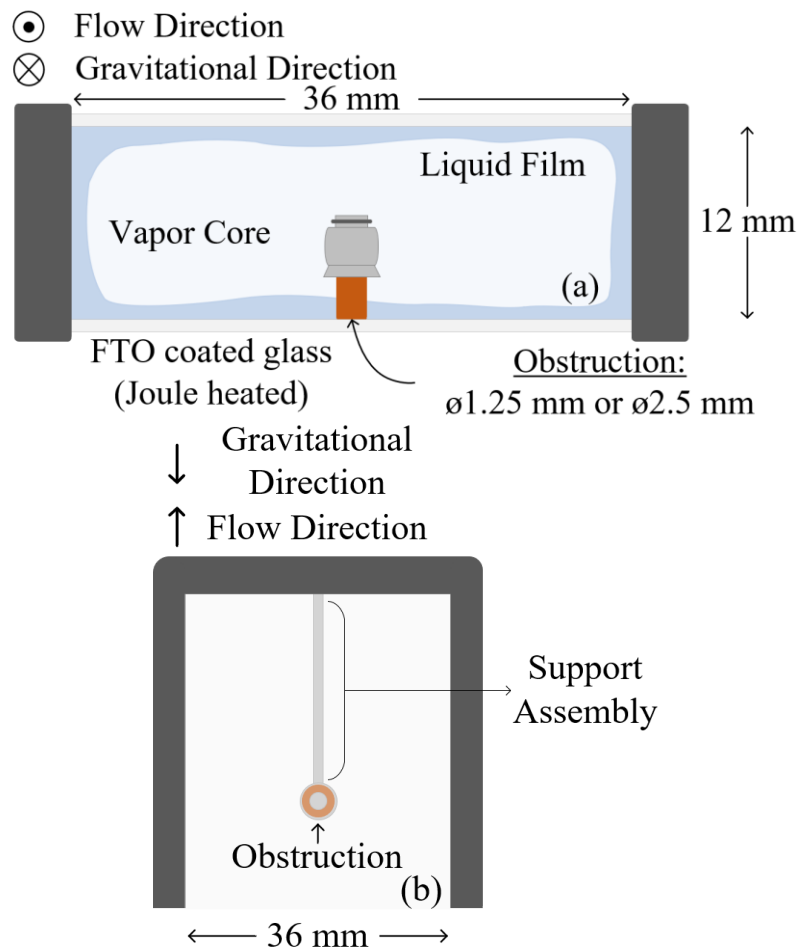


**Fig. 4:** Diagram of the test section from (a) the top view and (b) the front view

# CHAPTER 3: REVIEW OF NUCLEATE BOILING IN THIN LIQUID FILMS

## 1. Introduction

This chapter is a copy of the article submitted to the Internation Journal of Heat and Fluid Flow under the title "Nucleate boiling in the thin liquid films present in annular flow" with minor formatting changes. A description of authors respective contributions are as follows:

- Joseph Farrell: Investigation, Writing – Original Draft, Writing – Review & Editing, Visualization, Investigation.

- Evan T. Hurlburt: Conceptualization, Project Administration, Funding Acquisition.

- Arganthaël Berson: Conceptualization, Writing – Review & Editing, Supervision.

- Allison Mahvi: Conceptualization, Writing – Review & Editing, Supervision, Project Administration.

## 2. Fundamentals of Flow Boiling

### 2.1 The Boiling Cycle

The features present in annular flow such as disturbance waves, a thin liquid film, and the bulk fluid motion of annular flow make nucleate boiling difficult to predict. Therefore, the fundamentals of the nucleate boiling process will first be described without those considerations before layering in the complexities associated with liquid flow and thin films.

Boiling, or ebullition, follows a quasi-periodic cycle under favorable conditions [47]. First, superheated liquid next to the heated surface vaporizes in nucleation cavities [48]. These cavities are typically imperfections or roughness on the surface of the wall. As heat is continuously added to the vapor embryo, the bubble grows primarily along the surface of the wall. The initial stages of growth are governed by the surface tension of the liquid [48]. Later stages of bubble growth

occur in the radial direction away from the heated surface as buoyancy forces increase, resulting

in expansion opposite to the gravitational force. Eventually, the bubble grows large enough to pull

away from the heated surface due to the increased influence of buoyancy forces. During this phase,

the dry region under the bubble is reduced, and a microlayer of liquid forms between the bottom

edge of the bubble and the wall (Fig. 5). The microlayer is easily superheated and vaporized which

contributes to further bubble growth and results in very high heat removal rates from the heated

surface in the microlayer region [48]. As buoyancy becomes more dominant with bubble growth,

the bubble eventually will detach from the wall overcoming the surface tension force. When the

bubble detaches, cold liquid surrounding it rushes in to fill the void and the ebullition cycle repeats

[48]. This quasi-periodic cycle has a waiting period between bubble departures for the liquid to

reach the required superheat depending on fluid properties such as its density, surface tension,

latent heat of vaporization, and surface heat flux [48]. Fig. 5 provides a diagram illustrating the

cross-section of a bubble after significant growth and generalizations about the modes of heat

transfer occurring.
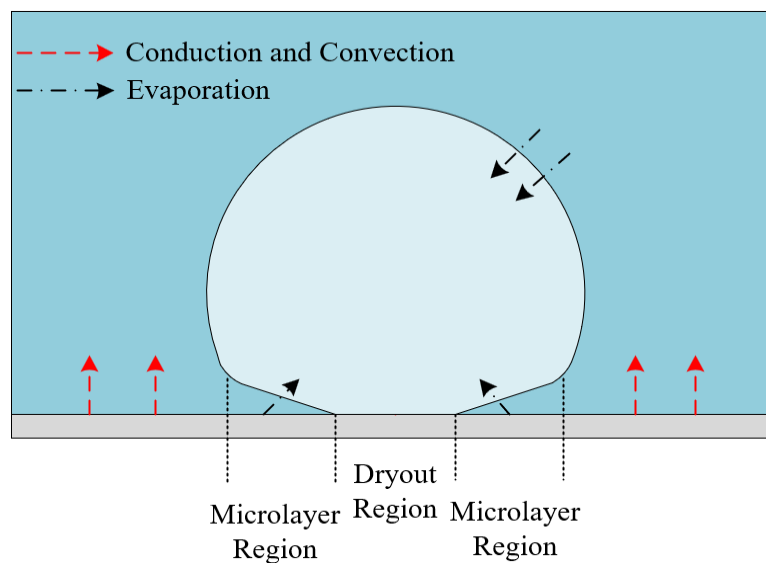


**Fig. 5:** Cross section of a simple growing bubble and associated heat transfer mechanisms, adapted from [48].

**2.2 Flow Boiling**

Nucleate flow boiling exhibits similar cyclic characteristics to those described above with added complexities arising from the bulk motion of the liquid. As shown in Fig. 1, nucleate boiling typically occurs at low to moderate vapor qualities before being suppressed by forced convective evaporation at higher qualities [3]. With motion in the liquid, it becomes necessary to define the point at which the vapor produced through boiling significantly influences the liquid motion, thus changing local boiling conditions. Vaporization of liquid in nucleation cavities marks the onset of nucleate boiling with bubble departure from the wall denoted as the onset of significant void. Any two-phase flow textbook contains equations describing the conditions required for this flow regime; however, these equations are typically empirical, and true mechanistic models of flow boiling systems are rare. Although the onset of nucleate boiling has been heavily studied, few correlations and no mechanistic models predict the suppression of nucleate boiling at higher vapor qualities.

One reason for the lack of mechanistic models of flow boiling is the complexity of the flow phenomena. Models of flow boiling must account for the shear forces between the liquid and the bounding walls which can bend and distort bubbles, altering the size of the microlayer region. This leads to uneven bubble growth and a less predictable boiling cycle (Fig. 6). The shear force can also cause bubbles to slide along the heated wall and merge with neighboring nucleation sites [20], [49]. Additionally, properties like the boundary layer thickness and the mass flow rate impact ebullition in flow boiling. *Chapter 3 Section 3* discusses the relative importance of these flow parameters as they pertain to nucleate flow boiling.
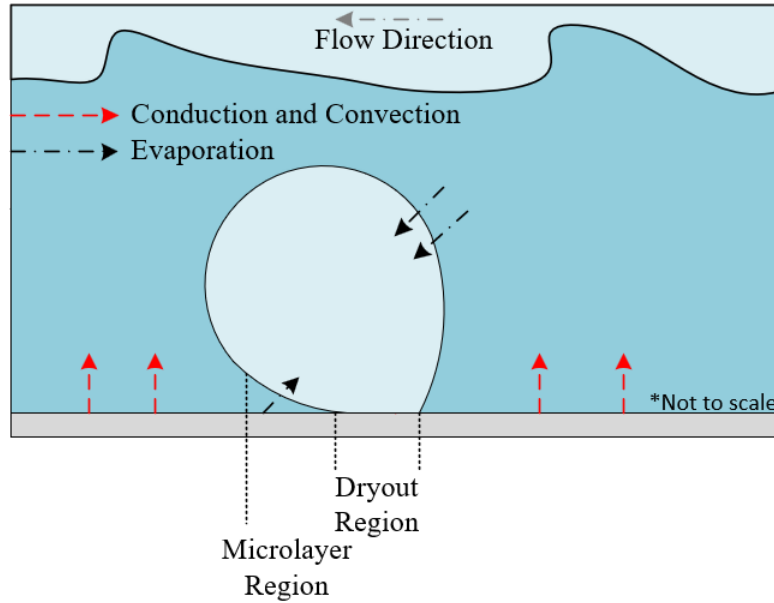
**Fig. 6:** Cross section of a growing bubble and heat transfer mechanisms for flow boiling adapted from [48].

## 2.3 Annular Flow Boiling

Before nucleate boiling in annular flow can be properly discussed, a basic understanding of the structure of annular flow is necessary. Annular flow is characterized by a relatively slow-moving thin liquid layer which is heavily influenced by viscous interactions with the surrounding walls and a relatively high-velocity vapor core containing entrained liquid droplets [9]. The liquid film has multiple flow features, the most prominent of which are waves. There are two primary categories of waves: disturbance waves and ripple or capillary waves. These waves are critical to understanding all phenomena observed in annular flow, including nucleate boiling. Le Corre [9] is a useful resource that can help to address deeper inquiries into the nature of waves in annular flow.

Disturbance waves are thicker than capillary waves and have been described as packets of well-mixed liquid traveling along the viscous sublayer in the liquid flow [1], [50]. Disturbance waves travel at a higher velocity than the rest of the liquid film as they are more subject to the

shear stresses from the fast-moving vapor core [2]. This shear stress relationship also means that wave velocity and frequency are directly dependent on the superficial liquid and vapor velocities, where superficial is defined as the mean velocity if just that phase flowed in the channel [51]. Wave velocity is also dependent on vapor quality [45]. As the liquid film thickness decreases with increasing quality, disturbance waves slow down before disappearing entirely and the liquid-vapor interface becomes smooth [45]. Important for this review, disturbance waves have a strong impact on nucleate boiling and mass transport between the liquid film and vapor core [9], [52]. In contrast, ripple waves have little impact on the thermal and hydrodynamic properties of annular flows. Ripple waves tend to be short-lived and low velocity [9]. They are usually created in the wake of a disturbance wave and are then overcome by the next disturbance wave [9]. These waves do not increase local mixing or significantly impact local liquid film thickness and thus will not be considered throughout the rest of the review [9].

The mechanisms of nucleate boiling in the annular flow regime are complex. The formation of a thin film fundamentally changes the balance of heat transfer mechanisms, increasing the importance of film evaporation. Vaporization from the liquid film can be so efficient in the annular flow regime that an imparted heat flux will no longer provide sufficient superheat to sustain nucleate boiling [53]. In the annular flow region, there is a constant oscillation in local flow parameters caused by the passage of disturbance waves making a true prediction of what is occurring in the system difficult. Understanding boiling in this regime is nonetheless critical to accurately predicting the total heat transfer associated with annular flow. Additionally, the creation, venting, and collapse of these bubbles can contribute to localized flow instabilities and the transport of mass in the form of liquid droplets from the liquid film to the vapor core [1].

**3. Mechanisms that Influence Boiling**

**3.1 Nucleation Cavities**

Nucleate boiling begins with the activation of a cavity on the heated surface. A foundational study of nucleation cavities and the boiling cycle was conducted by Hsu [54]. Although Hsu's criterion for nucleate boiling was originally developed for pool boiling, it is frequently used for flow boiling conditions including thin liquid films [55]. Hsu found that cavities should feature sharp elevation changes to trap pockets of gas on the surface. Surface roughness significantly affects both the incipience of boiling and the number of active nucleation sites. An active nucleation site is a surface cavity with a finite waiting period, meaning the subcooled liquid surrounding the nucleation cavity will eventually superheat and vaporize. This only occurs when the liquid surrounding the bubble nucleus, or embryo, is warmer than the vapor bubble temperature, resulting in a net heat flux into the bubble. The end of the waiting period is defined as the beginning of bubble growth. Hsu developed several equations related to the activation of nucleation sites which are widely used as the baseline for defining the criteria for when nucleate boiling occurs. Some of the more important equations are compiled in Table 2. Not only must the radius of the cavity fall between the minimum and maximum values as determined by the equations seen in Table 2, but also a cavity with a shorter waiting period is always preferred over neighboring cavities with longer waiting periods. In these equations, the various *C* constants represent different trigonometric relationships relating the angles between the edge of the bubble and the heated surface, capturing how the bubble shape changes throughout the growth process. The theta values indicate the difference between the local saturation temperature ($\theta_{sat}$) or the wall temperature ($\theta_w$) and the bulk temperature of the fluid which represents the degree of fluid superheating. The *A* constant incorporates how the fluid properties such as surface tension ($\sigma$), saturation temperature

$(T_{sat})$, latent heat of vaporization $(h_{fg})$, and density $(\rho)$ all play a role in the heat required for the onset of boiling. The parameter $k$ is the thermal conductivity of the fluid, while $b$ is the height of the bubble nucleus. The parameter $\delta_{TL}$ is the limiting thermal layer height which will be discussed in detail next.

**Table 2**: Combination of Hsu's equations [54]

| *Criterion for Incipience of Boiling:* | *Minimum Active Cavity Radius:* |
|---|---|
| $$q'' = \frac{k}{\delta_{TL}}\left[\theta_{sat} + \frac{2AC_3}{\delta_{TL}} + \sqrt{\left(2\theta_{sat} + \frac{2AC_3}{\delta_{TL}}\right)\left(\frac{2AC_3}{\delta_{TL}}\right)}\right]$$ | $$r_{c,min} = \frac{\delta_{TL}}{2C_1}\left[1 - \frac{\theta_{sat}}{\theta_w} - \sqrt{\left(1 - \frac{\theta_{sat}}{\theta_w}\right)^2 - \frac{4AC_3}{\delta\theta_w}}\right]$$ |
| *Cavity Radius:* | *Maximum Active Cavity Radius:* |
| $$r_c = \frac{b}{C_1} = \frac{\delta_{TL}(1 - \eta_b)}{C_1}$$ | $$r_{c,max} = \frac{\delta_{TL}}{2C_1}\left[1 - \frac{\theta_{sat}}{\theta_w} + \sqrt{\left(1 - \frac{\theta_{sat}}{\theta_w}\right)^2 - \frac{4AC_3}{\delta\theta_w}}\right]$$ |
| *Constants:* $$C_1 = \frac{1 + cos\,(\varphi)}{sin\,(\varphi)}$$ $$C_3 = 1 + cos\,(\varphi)$$ | $$A = \frac{2\sigma T_{sat}}{h_{fg}\rho_v}$$ |

## 3.2 Limiting Thermal Layer

Hsu also helped define the required heat flux to activate a nucleation cavity with favorable geometry [54]. This heat flux must be sufficient to ensure that the saturation temperature corresponding to the pressure inside the bubble nucleus is met or exceeded across the entire surface area of the bubble. The thickness of liquid where this criterion is satisfied is defined as the limiting thermal layer thickness representing the maximum bubble size. If the thermal layer is sufficiently thick, the bubble can grow large enough to detach from the surface and nucleate boiling occurs. The relationship between bubble size and thermal layer thickness can be seen in Fig. 7. The total thickness of the thermal layer is dependent on flow-based turbulence within the system and disturbances generated by detaching bubbles. Bubble disturbances are determined by the bubble growth rate, maximum bubble size, and frequency of departure. Strong turbulence drives the liquid

temperature near the heated surface towards the bulk liquid temperature reducing the availability of superheated liquid for bubble growth. In Fig. 7, the solid line represents the liquid temperature at different distances from the wall, $y$, assuming a linear temperature drop from conduction in the near wall region. The dashed line is a representation of the local saturation temperature, $T_{le}$. Hsu postulated that for a vapor embryo to grow into a full bubble, the local saturation temperature of the liquid surrounding the bubble should be at least equal to the saturation temperature corresponding to the pressure inside of the bubble, $\rho_v$. The local equivalent saturation temperature profile (equation (3)) is derived from the use of the Young-Laplace equation (equation (1)) and a linearized Clausius-Clapeyron equation (equation (2)):

$$p_v - p_l = \frac{2\sigma}{r_b} \tag{1}$$

$$T_{le} - T_{sat} = \frac{2\sigma T_{sat}}{r_b \rho_v h_{fg}} \tag{2}$$

$$T_{le}(y) = T_{sat}(p_l)(1 + \frac{2\sigma}{h_{fg} r_b \rho_v}) \tag{3}$$

where $r_b$ is the bubble radius, which is equal to the cavity radius, $\sigma$ is the liquid surface tension, $h_{fg}$ is the latent heat of vaporization, $T_{sat}$ is the saturation temperature derived from the liquid pressure, $p_l$ [56], [57]. The intersections between the solid and dashed lines represent the maximum and minimum nucleation cavity radii where the liquid temperature exceeds the local saturation temperature allowing vaporization and bubble growth. If a cavity cannot sustain a bubble at the minimum condition, it will not activate, and no vaporization will occur at that site until conditions change. The maximum condition does not necessarily indicate that the bubble will detach from the wall at that size; rather, it depicts the theoretical maximum size of activatable cavities as bubble departure is still primarily governed by buoyancy and shear forces.
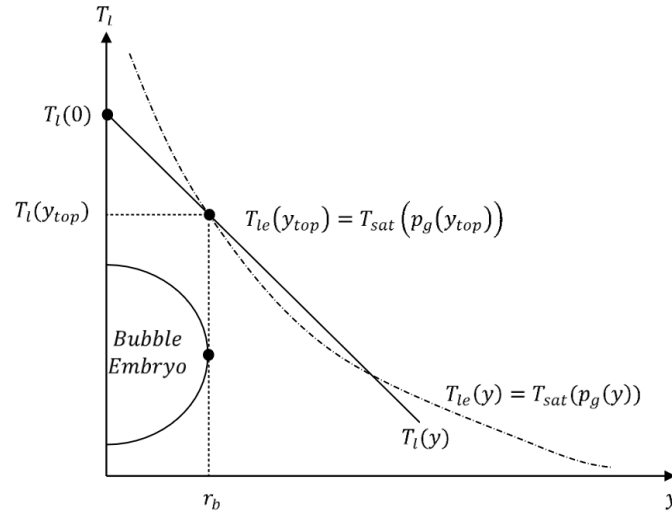
**Fig. 7:** Hsu's criterion for nucleate boiling. Liquid temperature at the top of the bubble embryo $T_l(y_{top})$ must meet or exceed local saturation temperature $T_{le}(y_{top})$ [57].

In annular flow, the constantly changing liquid conditions due to wave-based mixing also mean that, for a given nucleation site, bubble growth rates and frequencies of departure can widely vary. The size of the limiting thermal layer also creates competition among nucleation cavities that satisfy the cavity radius requirements. A smaller thermal layer results in a narrower range of cavities that meet the criterion for nucleate boiling. Competition exists because cavities exert a zone of influence over other nearby potential nucleation sites. If one cavity is active, it locally extracts heat from the surrounding liquid preventing other nearby sites from obtaining the superheated liquid necessary to grow. If the thermal layer shrinks, current active cavities may become inactive, and local smaller cavities that were previously inactive will become active.

When applying Hsu's criterion to annular flow boiling, the active cavity must satisfy the limiting thermal layer constraints, which compete with the thickness of liquid available and forced convection evaporation at the liquid-vapor interface. Considering this, small bubbles may shrink rather than grow at short distances from the heater, suppressing nucleate boiling. This behavior results from insufficient superheat given the sharp temperature profile present in annular liquid

films [58]. Additionally, the liquid-vapor interface is very close to the heater, allowing bubbles to grow nearly to the size of the liquid film and directly vent into the vapor core. This venting induces additional bubble nucleation not observed in other types of boiling conditions [58]. If the liquid film is thin enough, small vapor bubbles resulting from venting, bubble breakup, or wave rollover can act as nucleation sites at relatively low wall superheat for any gas that reaches the superheated liquid region [58] [59].

Forced convective evaporation by the vapor core can also suppress nucleate boiling in the system. If there is strong convective evaporation at the liquid-vapor interface, it will cool the liquid film to the point where the limiting thermal layer is insufficient for sustained bubble growth [53]. This balance between convective boiling and nucleate boiling is also influenced by the saturation temperature (see *Chapter 3 Section 4.3*), blurring the line between the two regimes and making it dependent on flow conditions. The suppression point depends on local values of quality, mass flux, and wall superheat making the suppression of nucleate boiling a local phenomenon [53]. Authors Su et al. have defined a nucleation cavity of radius $r_c$ as fully suppressed in annular flow using a time fraction, comparing the cumulative time when nucleate boiling is observed to the total data collection time [53]. They established an arbitrary threshold at a time fraction of 0.5 to determine when the system could be considered suppressed and used this to define the heat flux that would locally suppress nucleate boiling in annular flow,

$$q'' = 4.2 \frac{Nu}{(1-Nu)^{0.9}} \frac{k_l}{r_c \Delta T_{le,sat}} \tag{4}$$

where the Nusselt number can be defined as

$$Nu = \frac{h r_c}{k_l} \tag{5}$$

and

$$\Delta T_{le,sat} = T_{le} - T_{sat}. \tag{6}$$

Other correlations for the suppression of nucleate boiling have been developed by Sato and Matsumura and reformatted by Carey into equations (7)-(9) below [47], [60]. They were not created to capture the same level of nuance in the point of suppression but are still useful in seeing how each flow parameter can affect suppression. The quality at which nucleate boiling is suppressed in a flow can be expressed as,

$$x_{supp} = \frac{\gamma}{1 + \gamma} \tag{7}$$

where the constant $\gamma$ is equivalent to

$$\gamma = \left(\frac{\rho_v}{\rho_l}\right)^{0.56} \left(\frac{\mu_l}{\mu_v}\right)^{0.11} \left(\frac{q'' k_l h_{fg} \rho_v}{98 \sigma T_{sat} h_{lo}^2}\right)^{2.22} \tag{8}$$

when there is uniform wall heat flux, or

$$\gamma = \left(\frac{\rho_v}{\rho_l}\right)^{0.56} \left(\frac{\mu_l}{\mu_v}\right)^{0.11} \left[\frac{k_l h_{fg} \rho_v (T_w - T_{sat})}{28 \sigma T_{sat} h_{lo}}\right]^{2.22} \tag{9}$$

for isothermal boundary conditions. In these equations, $h_{lo}$ is the single-phase convection coefficient if the entire flow was liquid. The single-phase convection coefficient could be calculated through many different correlations depending on flow conditions, but for convective vaporization of water in a vertical tube,

$$\frac{h}{h_{lo}} = 3.5 \left(\frac{1}{X_{tt}}\right)^{0.5} \tag{10}$$

where $X_{tt}$ is the turbulent-turbulent Martinelli parameter expressed as

$$X_{tt} = \left(\frac{1-x}{x}\right)^{0.9} \left(\frac{\rho_v}{\rho_l}\right)^{0.5} \left(\frac{\mu_l}{\mu_v}\right)^{0.1} \tag{11}$$

Equation (10) is only valid when nucleation boiling has been fully suppressed, but it can be combined with an onset of nucleate boiling equation developed by Sato and Matsumura to yield equations (7)-(9) [47], [60]. While the correlation from Sato and Matsumura may be useful for the quick and rough identification of suppression, it is empirical and does not consider the localized nature of suppression due to other important flow parameters such as disturbance waves. The model from Su et al. allows for local deviations through the explicit inclusion of the limiting thermal layer depicting the relationship between liquid film height, thermal layer height, and the possibility for nucleate boiling.

## 3.3 Flow Parameters

This section describes how flow parameters influence nucleate boiling in the annular regime. Specifically, the impact of liquid film thickness, pressure, surface tension, channel geometry, mass flow rate, and applied heat flux will be discussed.

### 3.3.1. Liquid Film Thickness

In some models of heat transfer in annular flow, the liquid film is treated as a conduction resistance between the heated wall and the liquid-vapor interface if the liquid film thickness is less than the thermal boundary layer, as observed between disturbance waves [4]. The thickness of the liquid film is then proportional to this effective conduction resistance, directly influencing the convective evaporation rate for a given wall superheat as it affects the liquid film temperature at the interface [61]. A thicker liquid film typically results in a higher film temperature which promotes nucleate boiling.

The two key flow properties that influence liquid film thickness are vapor quality and pressure (via changes in the density ratio). A high-quality film has more vapor and a thinner liquid layer which favors convective evaporation [61]. However, simply increasing the vapor quality to yield a thinner film is not the whole story. The total volume of the flow that is vapor, also known as the void fraction, can give a more accurate representation of the liquid film thickness. As void fraction increases, the vapor takes up a larger volume of the channel, meaning the liquid film thickness must decrease [62]. Fig. 8 shows how void fraction changes with vapor quality for a variety of different fluids. For refrigerants and low-pressure water, the density ratio is low (0.0065 for R245fa at 150 kPa and 0.0058 for steam at 1 MPa), causing the void fraction to rise rapidly with small changes in quality [62]. Thus, void fraction is highly dependent on vapor quality at low values, but past qualities around 0.3, further increases have minimal impact on the liquid film thickness. As the pressure approaches the critical pressure, the density ratio approaches one, and the void fraction-quality relationship becomes more linear. For comparison, in Fig. 8, the density ratio of $CO_2$ is 0.5, while the density ratio of steam at 7 MPa is 0.05. The larger density ratio leads to slower changes in the void fraction during boiling as shown in Fig. 8.
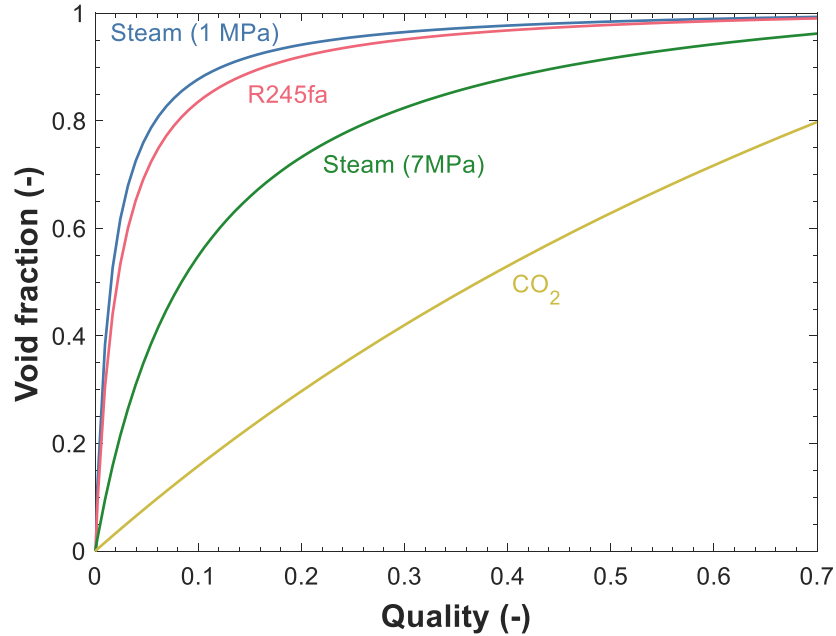
**Fig. 8:** Annular flow void fraction as a function of vapor quality using Thome correlation [63] for steam at 1 and 7 MPa, R245fa at 150 kPa and $CO_2$ at 7000 kPa. Adapted from [62]

3.3.2. Pressure

In addition to the impact pressure has on void fraction and liquid film thickness, it can also indirectly influence other parameters important in annular flows. The relationship between pressure, saturation temperature, and nucleate boiling is the clearest and most direct. As shown in Fig. 7 and in the combination of the Young-Laplace equation (equation (1)) with the Clausius-Clapeyron equation (equation (2)), nucleate boiling is present when the liquid temperature exceeds the local equivalent saturation temperature [54], [56], [57]. This saturation temperature is a function of the gas pressure inside the bubble. As system pressure increases, so too will the saturation temperature, necessitating higher liquid temperatures to exceed the saturation temperature and achieve boiling. Further discussion of the relationship between pressure and nucleation through changes in saturation temperature can be found in *Chapter 3 Section 4.3*. The effects of pressure are also indirectly observed in every aspect of a flow by its influence on

thermophysical properties such as surface tension, density, conductivity, viscosity, quality, heat capacity, enthalpy, etc., which are discussed in the subsequent sections.

### 3.3.3. Surface Tension

A large portion of classical work focusing on nucleate boiling in liquid films focuses on wavy falling films, which provide insights into what occurs in annular flows. One of the primary findings of these studies is the impact of surface tension on nucleate boiling. Low surface tension fluids are more likely to splash liquid from their wave crests which reduces the mass of the wave and its flow rate [64]. When the flow rate decreases, there is a reduction in the convective heat transfer coefficient tipping the balance toward nucleate boiling [64]. A lower surface tension also increases the relative influence of gravitational forces on the liquid. Gravitational effects lead to higher degrees of stratification, meaning less mixing occurs in the liquid film, enhancing nucleation [61]. Additionally, wave velocity and longitudinal size both decrease with decreases in surface tension [51]. Local heat transfer coefficients are dependent on wave turbulent diffusivity, and any changes to it may lead to inconsistent boiling [50]. Further discussion of the waves in thin films and their relationship to nucleate boiling is included in *Chapter 3 Section 4*.

Surface tension is the capacity of a liquid to resist external force, meaning that decreasing surface tension fundamentally diminishes a liquid's cohesive force and promotes dispersion. Consequently, surface tension is inversely related to wettability. Variations in surface wettability significantly alter boiling properties such as the size of the liquid microlayer (as discussed in *Chapter 3 Section 2.1*) and the total dry area. The effects of surface tension and wettability in flow boiling have only recently begun to be studied. Given that flow boiling introduces new forces to determine bubble departure, the relationship between wettability and heat transfer is complex. In microchannel experiments performed by Li et. al [65], the dryout characteristics of the surface

changed depending on surface wettability. For conditions where an untreated hydrophilic surface experienced dryout and a deterioration in heat transfer performance, a superhydrophilic surface at identical conditions did not exhibit the same degradation. Additionally, the superhydrophilic surface maintained a consistent heat transfer coefficient through a uniform distribution of the liquid-vapor interface at varying input heat flux or mass flux which was not observed for untreated surfaces. Similar results are observed in conventional sized channel experiments. Upot et. al [66] increased surface wettability with a low surface tension fluid through structuring the surface on a micrometer to nanometer scale. Comparing the structured channels to smooth channels, increased favorable potential nucleation cavities, enhanced turbulence, and thinner liquid films in the stratified and annular regimes boosted heat transfer by factors greater than two while moderately increasing pressure drop. While this is still a relatively nascent area of investigation, it appears that increasing the surface wettability could increase heat transfer at the cost of pressure drop.

3.3.4. Channel Geometry

Channel geometry can affect various aspects of annular flow, including the velocity profile in the liquid film, average liquid film thickness, wave heights, and wave frequency [67]. As discussed throughout this review, these changes can impact nucleate boiling in the annular flow regime. Tran et al., performed an experiment comparing different channel geometries and sizes and found that, in a small circular channel (D = 2.46 mm), heat transfer was dependent on heat flux rather than mass flux over a quality range 0.2 - 0.8. This indicates nucleation is more dominant than convective effects in small channels over a wider range of vapor qualities than what is seen in large channels (see *Chapter 3 Sections 3.3.5* and *3.3.6* for a more detailed explanation). Additionally, the authors found there was little difference in local heat transfer coefficient between rectangular and circular channels with the same hydraulic diameter for the majority of the

perimeter [68]. Although channel geometry changes the distribution of the liquid film (circular channels have a more uniform film than rectangular channels, which have differences in liquid film thickness between the corner of the channel and the sides), the overall impact on local heat transfer coefficient is small [2].

### 3.3.5. Mass Flow Rate

Mass flow rate also significantly influences annular flow behavior and bubble nucleation. Zajec et al. quantified the bubble nucleation behavior in their study on subcooled boiling of R245fa in an annular horizontal channel  [69]. Although this study is in the bubbly flow regime, it still gives interesting insights into bubble nucleation behavior applicable to annular flows. Zajec et al. found that mass flow rate changes the convective heat transfer coefficient in a similar manner to external flow. The higher heat transfer coefficient decreases the wall superheat, making bubble nucleation challenging [69]. Even though higher heat transfer coefficients are typically associated with high mass fluxes as illustrated in Fig. 9 (a), they are also associated with a decrease in the total vapor void. At high mass fluxes, enhanced convective heat transfer reduces the maximum bubble size thereby lowering the total vapor void. Vapor void in this experiment must come from bubbles as it does not have a vapor core (subcooled boiling) [69]. The trend accounts for the change in bubble size distribution depicted in Fig. 9 (b). As the liquid mass flux increases, the bubbles transition from a bimodal volume distribution to a single peak with a smaller average size. If the trends were to be extrapolated to higher mass fluxes, the average bubble size would continue to decline, ultimately leading to the full suppression of nucleate boiling [69].
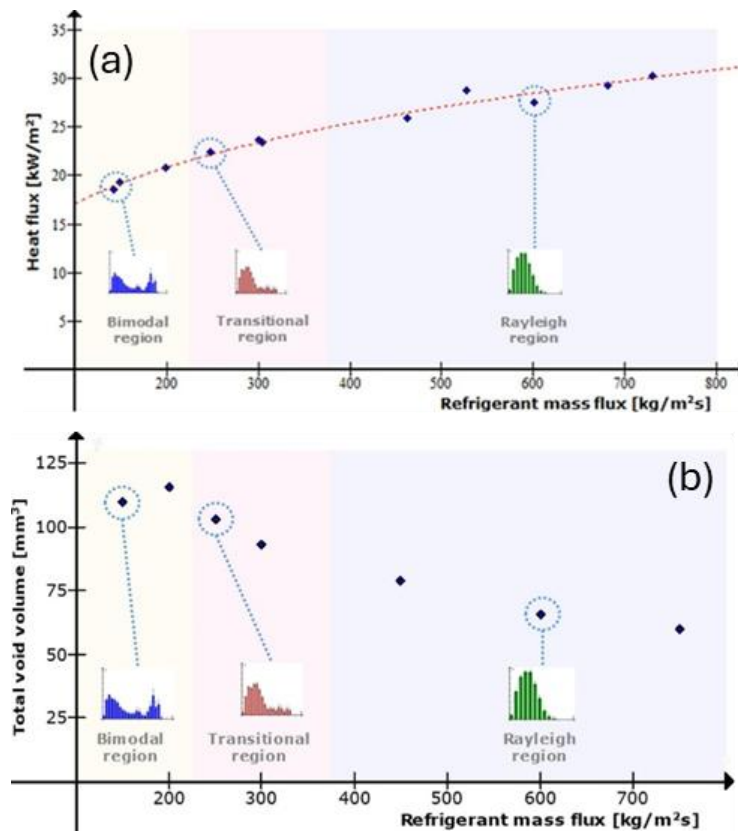
**Fig. 9: (a)** Dependence of the heat flux on refrigerant mass flux, **(b)** Dependence of the total void volume on the mass flux. Developed for R245fa in horizontal annular flow at 1.8 bar and average void fraction of 2.3% where bimodal, transitional, and Rayleigh describe the type of statistical distribution of bubble radii [69].

While Zajec et al. thoroughly investigated very low vapor quality flows, other researchers have noted that the influence of mass flow rate on bubble nucleation seems to be dependent on the vapor quality. At low vapor qualities, where nucleate boiling is the dominant heat transfer mechanism, mass velocity appears to have no promoting or suppressing effect [61], [70]. Heat transfer is primarily due to the number of active nucleation sites and remains largely unchanged by mass flux [70]. In contrast, at higher vapor qualities (0.2-0.8) where convective boiling is dominant, mass flux has more of an influence on the frequency of bubble nucleation because it significantly contributes to the suppression of nucleate boiling through convective heat transfer

[61], [70]. If nucleate and convective boiling contribute similarly to the heat transfer, the heat transfer coefficient is dependent on mass flow rate [61].

### 3.3.6. Heat Flux

The last flow parameter discussed here is the most intuitive because there is very little difference between pool boiling and annular thin film boiling. At high heat fluxes, the heated surface is very superheated leading to a thick limiting thermal boundary layer [61], [70]. This condition facilitates the formation of nucleation sites which grow quickly, increasing the frequency of bubble departure [61], [70]. The strong relationship between heat flux and nucleate boiling is such that high heat fluxes will delay the point of the suppression of nucleate boiling even at high vapor qualities [70]. Fig. 10 shows the relationship between applied heat flux and the point of suppression of nucleate boiling. As Bediako et al. report, convective boiling dominates when the heat transfer coefficient depends on vapor quality and mass flux while nucleate boiling dominates when there are minimal effects of mass flux and vapor quality [71]. As the heat flux increases, the heat transfer coefficient gradually loses dependency on the vapor quality. At the highest heat fluxes shown in Fig. 10, there is zero slope of the heat transfer coefficient over a range of vapor qualities indicating the dominance of nucleate boiling. The point at which the heat transfer coefficient becomes dependent on vapor quality could be interpreted as the point of nucleate boiling suppression.
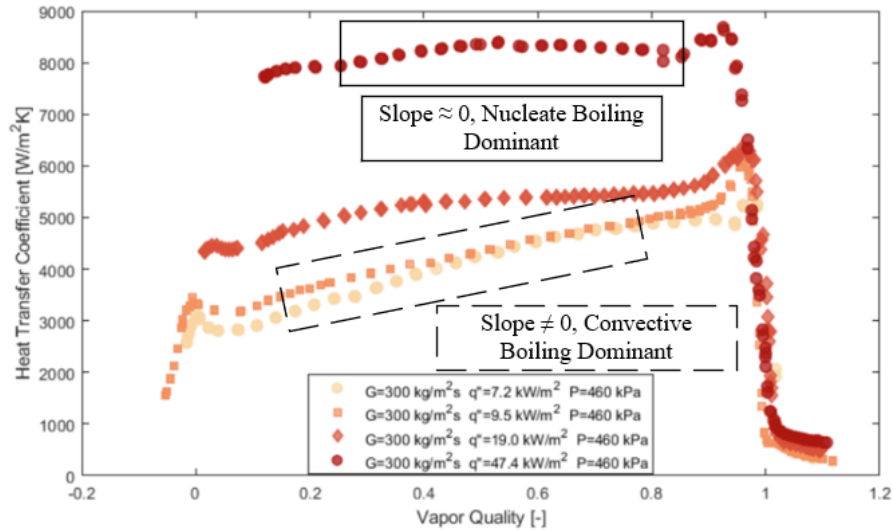
**Fig. 10:** Heat transfer coefficient of R134a at varying applied heat flux, adapted from [71]

Increasing heat flux also accelerates the transition from liquid to vapor. As the flow is constrained by the pipe walls, the vapor phase cannot expand and is forced to accelerate in the flow direction [70]. This enhances heat exchange between the vapor and liquid phases leading to increased heat removal from the wall. While this could theoretically provide some suppression of nucleate boiling, it remains dominant until such high vapor qualities are reached that the bulk liquid temperature reduces below the necessary superheated levels via film evaporation [70]. The uniformity of incoming heat flux is another contributing factor. Local superheating in the liquid layer occurs when a non-uniform heat flux is applied to the liquid. Having a gradient decreases competition between neighboring potential nucleation sites as each area may develop unique optimal nucleation site conditions [70]. This means that one particularly suitable nucleation site will have reduced influence on its neighbors as it is not the preferred nucleation site under neighboring conditions. All of this allows for more total active nucleation sites and significantly enhanced nucleate boiling under non-uniform heat flux [70].

**3.4 Correlations for Nucleate Boiling**

The fluid properties and operating conditions discussed above are often incorporated into correlations to capture the relative impact of nucleate boiling. Table 3 shows a few classical and widely applicable correlations for predicting the heat transfer coefficient associated with nucleate flow boiling. The heat transfer coefficient serves as a proxy for the frequency or intensity of nucleate boiling. Although each of these models predicts the heat transfer coefficient differently, they all reflect the dependencies discussed in *Chapter 3 Section 3.3*.

For instance, all presented correlations indicate that an increase in the liquid-vapor density ratio leads to a higher heat transfer coefficient, which is related to changes in the void fraction and average film thickness. The influence of vapor quality is also evident, particularly in the work of Kandlikar, Kim and Mudawar, and Liu et al., where quality is inversely proportional to nucleate boiling heat transfer coefficient, consistent with the expected relationship to film thickness. Although not as clearly visible in the other correlations, the Chen correlation clearly shows the inverse relationship between surface tension and nucleate boiling. Furthermore, these correlations capture the directly proportional effect of applied heat flux on nucleate boiling intensity.

Additionally, the correlations from Chen and Liu et al. also include the constant, *S*, representing the degree of suppression of nucleate boiling derived from a curve fit by the authors [3], [72]. This factor is primarily a fitted correlation but shows that a well-mixed flow (characterized by a large Reynolds number) exhibits a greater degree of suppression. The nucleate boiling correlation developed by Liu et al. was originally derived by Jung et al. from pool boiling data, but Liu utilized the suppression factor to modify this correlation for annular flow boiling [73]. The correlation from Liu et al. combines the contributions from both convective and nucleate

boiling utilizing curve fit factors, *F* and *S*, to capture the relative importance of each type of boiling to the total heat transfer coefficient.

**Table 3**: Heat Transfer from Saturated Nucleate Boiling in Annular Flow

| **Chen (1966)** [22] |
|---|
| $$h_{NB} = 0.00122 \left\{ \frac{k_l^{0.79} c_{p,l}^{0.45} \rho_l^{0.49} g^{0.25}}{\sigma^{0.5} \mu_l^{0.29} h_{fg}^{0.24} \rho_v^{0.24}} \right\} \Delta T_{sat}^{0.24} \Delta P_{sat}^{0.75} S$$ $$S = \frac{1}{1 + 2.56 \times 10^{-6} (Re_l F^{1.25})^{1.17}}$$ $$F = \left( \frac{Re}{Re_l} \right)^{0.8}$$ |
| **Kandlikar (1990, 1991)** [23] |
| $$h_{NBD} = \left[ 0.6683 Co^{-0.2} (1-x)^{0.8} f_2(Fr_{lo}) + 1058 Bo^{0.7} (1-x) F_{fl} \right] h_{lo}$$ $$Co = \left( \frac{\rho_v}{\rho_l} \right)^{0.5} \left( \frac{1-x}{x} \right)^{0.8}$$ $$Bo = \frac{q_w''}{G h_{fg}}$$ $$Fr_{lo} = \frac{G^2}{\rho_l^2 g D}$$ Vertical Tubes: $f_2(Fr_{lo}) = 1$ Horizontal tubes with $Fr_{lo} \geq 0.04$: $f_2(Fr_{lo}) = (25 Fr_{lo})^{0.3}$ $F_{fl}$ = Fluid surface parameter tabulated in Kandlikar (1990, 1991) |
| **Kim and Mudawar (2013)** [74] |

$$h = (h_{NB}^2 + h_{CB}^2)^{0.5}$$

$$h_{NB} = \left[2345\left(Bo\,\frac{\Pi_{heated}}{\Pi_{flow}}\right)^{0.70}\left(\frac{P}{P_{crit}}\right)^{0.38}(1-x)^{-0.51}\right]\left(0.023Re_l^{0.8}Pr_l^{0.4}\frac{k_l}{D}\right)$$

$$h_{CB} = \left[5.2\left(Bo\,\frac{\Pi_{heated}}{\Pi_{flow}}\right)We_{lo}^{-0.54} + 3.5\left(\frac{1}{X_{tt}}\right)^{0.94}\left(\frac{\rho_v}{\rho_l}\right)^{0.25}\right]\left(0.023Re_l^{0.8}Pr_l^{0.4}\frac{k_l}{D}\right)$$

$$We_{lo} = \frac{G^2 D}{\rho_l \sigma}$$

| **Liu et al. (2021)** [72] |
|---|

$$h = Fh_{CB} + Sh_{NB}$$

$$h_{CB} = 0.023\frac{k_l}{D}\left(\frac{G(1-x)D}{\mu_l}\right)^{0.8}Pr_l^{0.4}$$

$$F = 1 + 0.205Co^{-0.94}\left(\frac{\mu_l}{\mu_v}\right)^{0.6}\frac{1}{1+We_v^{-0.3}}$$

$$We_v = \frac{G^2 x^2 D}{\sigma \rho_v}$$

$$h_{NB} = 41.4\frac{k_l}{D_b}\left(\frac{qD_b}{k_l T_{sat}}\right)^{0.835(1-\frac{P}{P_{cr}})^{1.33}}\left(-\log\frac{P}{P_{cr}}\right)^{-1.52}\left(1-\frac{\rho_v}{\rho_l}\right)^{0.53}$$

$$S = \frac{1}{1+\left(\frac{G(1-x)DF^{1.25}}{\mu_l}\times 10^{-4}\right)^{0.3}\left(\frac{q''}{Gh_{fg}}\times 10^{-4}\right)^{-0.3}}$$

It is important to note that nucleate boiling correlations are derived from curve fits rather than capturing the physics of the flow. Caution should be exercised when applying correlations outside of the original dataset from which they were created. Additionally, it is advisable to use

the units with which the correlation was formulated. Chen's correlation was developed using English units, while Kandlikar, Kim and Mudawar, and Liu et al. use SI units. Furthermore, the gravitational constant, $g$, in Chen (1966) only needs to be included when using English units.

Of the correlations above, the Chen correlation is the most widely used for vertical saturated flow boiling and is often the baseline against which new correlations are compared. It works particularly well with water-steam flows at low pressures, but diverges from experimental data when applied to refrigerants [3]. The Kandlikar correlation captures both horizontal and vertical flows and is based on saturated flow boiling data for water, refrigerants, and cryogenic fluids. The correlation from Kim and Mudawar is a widely used modern correlation for miniature and micro channels developed using 10,805 data points gathered from 31 sources with a mean absolute error in heat transfer coefficient prediction of 20.3%. The Kim and Mudawar correlation is popular because it was developed for a wide range of working fluids, hydraulic diameters, mass velocities, liquid Reynolds numbers, qualities, and reduced pressure. The correlation developed by Liu et al. was derived for low-pressure refrigerants in smooth horizontal tubes, and it shows good agreement with experimentally calculated heat transfer coefficients from the authors' data and previously published data.

## 3.5 Homogeneous and Heterogeneous Bubble Nucleation

The classical theory of bubble nucleation discussed thus far focuses on the growth of pre-existing vapor embryos trapped inside cavities on the boiling surface. This process, known as heterogeneous bubble nucleation, involves vapor embryos that are in contact with both solid and liquid phases [47]. This style of bubble nucleation accurately describes the phenomena observed in typical boiling systems and has been adopted in the development of most boiling correlations.

However, there are limitations of this theory for edge cases such as boiling on perfectly smooth surfaces that remain an open topic.

Bubble nucleation can occur completely within the superheated liquid layer, a process referred to as homogeneous nucleation. Homogeneous nucleation occurs due to internal fluctuations in local molecular density and energy in the liquid, potentially leading to the vaporization of liquid close to the saturation limit [47]. According to the current pre-existing vapor theory, if a heated surface is atomically smooth, homogeneous nucleation should account for the boiling behavior in the system. This understanding of bubble nucleation has been challenged. Experiments by Theofanous et al. revealed that boiling on a nanoscopically smooth heater was observed at only a few kelvins of superheat, while the pre-existing nuclei theory predicts a required superheat of approximately 300 K [75].

This premature boiling on smooth surfaces prompted Dihn and Theofanous to explore existing research in the nucleate boiling realm that could describe the limitations of the pre-existing vapor theory [76]. One of the many experiments described came from Weng et al. who hypothesized that a vapor film forms immediately upon heater activation after observing that, as atomically smoother heaters became smaller, higher nucleation temperatures were required [77]. Another concept described by Dihn and Theofanous comes from much earlier work by Frenkel, who found that nucleation often begins at hydrophobic islands on the boiling surface [78]. Frenkel posited that liquid adhesion to a surface could be locally reduced due to a monomolecular layer of surfactant or other impurities, resulting in hydrophobic islands. This concept was further discussed in a series of papers by Ishida et al. and Tyrrell and Attard who proposed that the hydrophobic surface acted as a nucleation site for air in effectively supersaturated water [79], [80]. Despite these

insights challenging the pre-existing vapor theory, most literature uses the classical vapor embryo framework to describe nucleate boiling phenomena in their experiments.

## 4. Role of Disturbance Waves in Nucleate Boiling

## 4.1 Visualization of Disturbance Waves and Nucleate Boiling

One of the most significant findings related to nucleate boiling recently has been the role of disturbance waves. Just as they impact the dryout and rewetting process, disturbance waves are responsible for oscillations in nucleate boiling observed in annular flow. Barbosa et al. were among the first to investigate the influence of disturbance waves on boiling in annular flows, discovering that these waves increased bubble nucleation in their wake [52]. Using high-speed imaging (Fig. 11), the authors found that the arrival of disturbance waves triggers nucleate boiling, resulting in a greater number of active nucleation sites in the liquid, particularly in the immediate wake of larger waves. Barbosa's experimental setup involved a series of concentric heated pipes and glass tubes with an upward steam flow. In Fig. 11, as the wave progresses in the streamwise direction from Fig. 11 (a) to (d), the difference in the number of active nucleation sites, identified by arrows, between the wave front and tail is significant. The wave region itself contains many reflections and obscurations, making bubble identification in that area much more difficult. The theory that waves may trigger bubble nucleation was originally postulated by Marsh and Mudawar [64]. While studying falling films, they observed wave-based boiling behavior and measured an increase in wall superheat underneath and in the wake of disturbance waves. This superheat provides favorable conditions for bubble nucleation and growth, in contrast to thin film regions, which tend to deprive the wall of the superheat necessary to sustain nucleation. This mechanism of bubble nucleation in annular flow has also been corroborated by other authors giving strong confidence in the reality of this phenomenon [57].
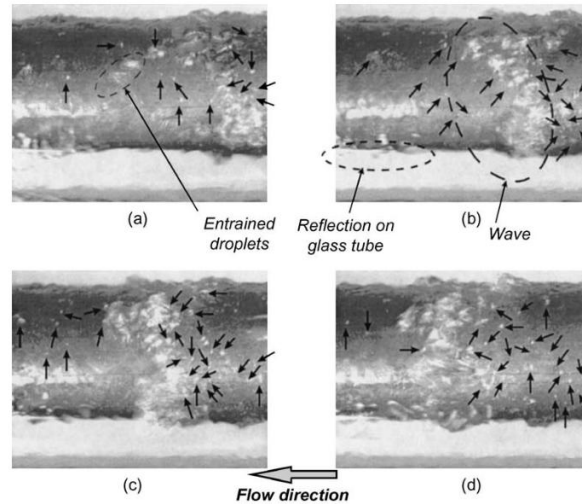
**Fig. 11:** Identification of active nucleation sites in wavey annular flow [52]

Barbosa et al. provided interpretations of previously suggested theories regarding the increased frequency of bubble nucleation in the disturbance wave region. The first theory suggests there is a reduction in the heat transfer coefficient in the wave region, leading to increased wall temperatures and therefore conditions more conducive to nucleate boiling. This theory is founded on the fact that the wave region is considerably thicker than other portions of the liquid film, making it reasonable to assume changes in heat transfer properties occur. A thicker liquid film could increase the conductive resistance of the system and therefore raise the wall superheat. Crucially though, disturbance waves are very well mixed by turbulent eddies [64]. A general understanding of convective heat transfer leads to the conclusion that mixing the fluid results in an increased liquid heat transfer coefficient, decreasing the wall superheat. This interplay between increased conductive resistance and increased convective heat transfer introduces uncertainty regarding whether a temperature change is the primary driver of increased nucleate boiling. A second theory says that a reduction in pressure experienced in the wave region is to blame for the increase in nucleate boiling. This pressure drop would lower the local saturation temperature and allow for more nucleation sites to activate. The third theory suggests there is bubble entrainment

in the waves which allows for more nucleation. It is possible that microbubbles are propelled into the superheated region near the wall by the disturbance waves. These microbubbles could then attach to local vapor embryos and nucleation sites, allowing them to grow and detach creating a short burst of nucleate boiling. Before explaining each of these theories in more depth, the authors would like to acknowledge our favor of the first theory so that any unconscious bias in the explanation of the theories is transparent to the reader.

**4.2 Temperature Theory**

4.2.1 Simulations

Out of the three theories put forward by Barbosa et al., the temperature theory has garnered the most attention. Two computational fluid dynamics (CFD) studies have analyzed the theory while closely mimicking Barbosa's experimental conditions [81], [82], [83]. Yang et al. developed a liquid-only model featuring a stationary liquid and moving wall to mimic liquid flow [83]. The vapor interactions were approximated as a constant shear stress across the surface of the liquid, and only the liquid phase was explicitly modeled, meaning no boiling or microbubbles were present. Fig. 12 (b) illustrates the model domain and boundary conditions while Fig. 12 (a) displays the velocity vectors in the base film and the disturbance wave. The results show a significant velocity gradient between the wall and the vapor core, producing a chaotic swirling velocity profile in the wave region. Notably, the bulk velocity of the waves in the simulation is reasonably similar to what is seen in experimental investigations [45].
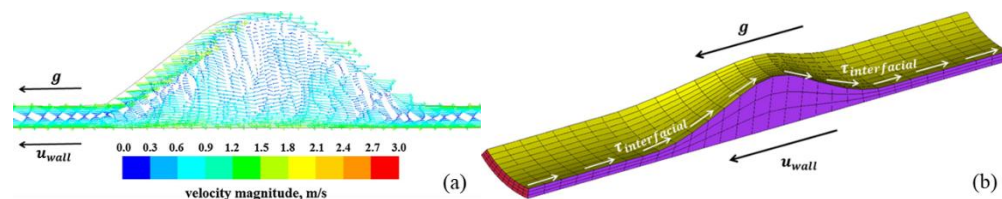


**Fig. 12: (a)** Cut plane of velocity vector simulation, **(b)** Schematic of simulation setup [83]

The increased mixing affects the wall temperature profile under the wave. Fig. 13 presents the difference between the wall and saturation temperatures, normalized by saturation temperature. A high-temperature region develops at the front of the wave where the flow transitions between the laminar base film and the turbulent wave as seen in Fig. 13 (a). As the wave travels across the wall, high-temperature streaks form between the wave front and the wave tail. The thermal streaking effect is driven by velocity fluctuations in the disturbance wave and can result in temperature increases of up to 6% from the saturation temperature, sustained for about 40 ms. As a note, the authors explicitly state that the results are qualitative, so the exact values should be interpreted cautiously. That said, they claim that the temperature increase and duration of exposure would result in boiling based on past literature. Looking at the time-averaged temperature field in Fig. 13 (b), the wave region has a lower time-averaged temperature compared to the laminar region, indicating the wave contributes to a higher average heat transfer coefficient. This is consistent with expectations when comparing laminar and turbulent flows.
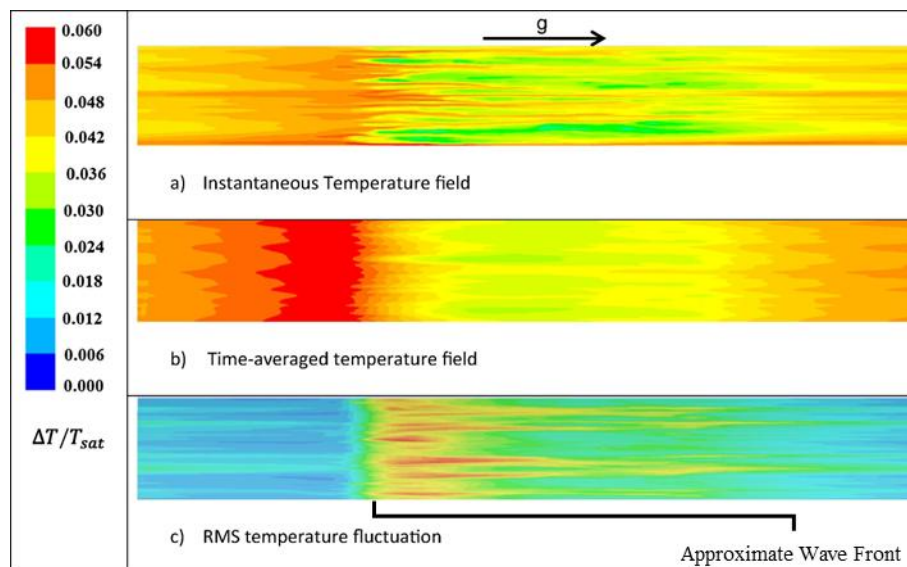


**Fig. 13:** Normalized wall temperature difference field of (a) instantaneous temperature, (b) time-average temperature, (c) root-mean-squared temperature fluctuation [83]

In a second simulation, Sato and Niceno also evaluated Barbosa's setup using CFD, but allowed disturbance waves to naturally develop along liquid flow [82]. While both experiments used a Large Eddy Simulation with a Smagorinsky model for sub-grid turbulence, Sato and Niceno allowed for heat and mass transfer between the vapor and liquid phases using a numerical method based on the mass conservation sharp-interface phase change model. They also used non-homogeneous shear stress along the heated length to generate waves rather than assuming the static shape of a single wave as seen in Yang et al. Similar to the previous investigation, Sato and Niceno also concluded that boiling resulted from high local wall temperatures directly associated with the passage of a wave. However, in contrast to the previous simulation, there is a higher average temperature under the wave with no temperature streaking. The simulation results are depicted in Fig. 14, clearly showing the wave region results in elevated temperatures. It is difficult to determine the exact location of the high-temperature region in relation to wave position, such as whether the front of the wave has the highest temperatures. While variations in temperature across the width of the wall did exist, they were not as distinct as thermal streaking described by Yang et al. The authors attributed the higher average temperature under the wave to the type of model used despite expectations that turbulence in the wave would yield lower temperatures. Disagreement in these two CFD simulations, both attempting to describe the same experimental conditions, is a reminder that CFD may be used as a clue to system behavior but should not be considered as a one-to-one comparison to experimental work. Nevertheless, both simulations agree that the wall temperature increases with the passage of disturbance waves, lending confidence to the idea that temperature variations trigger nucleate boiling in thin liquid films.
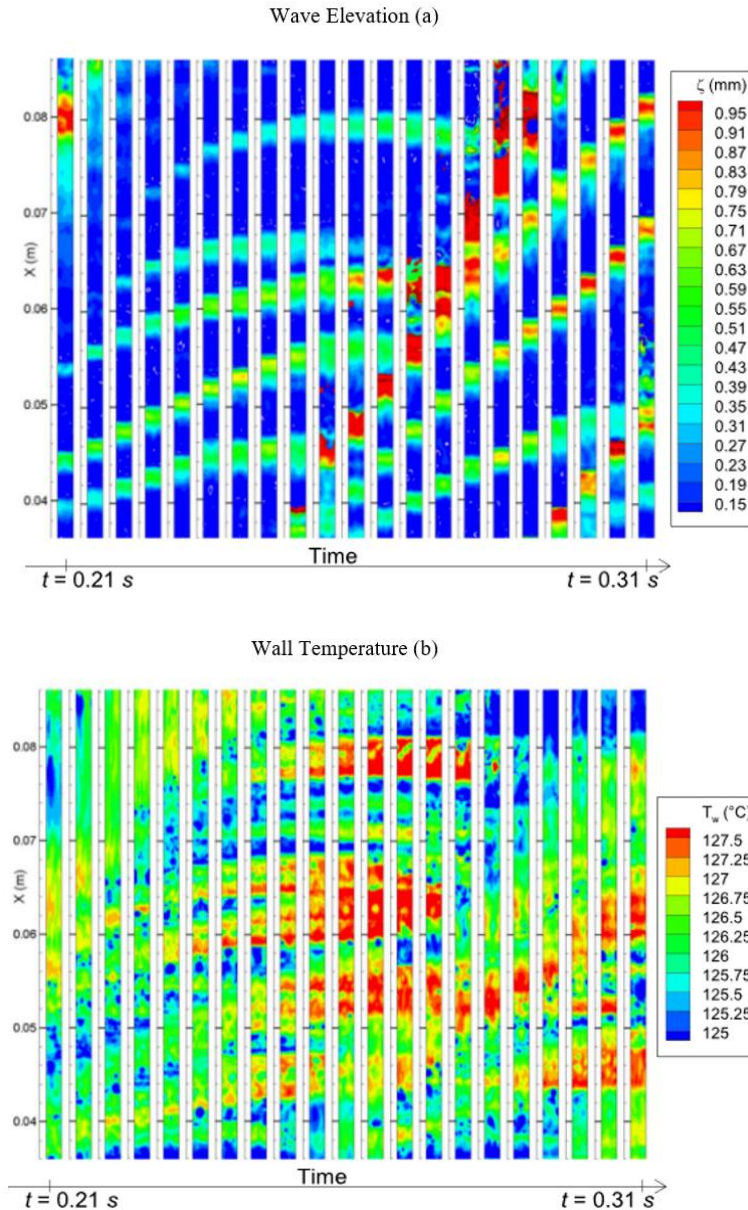
**Fig. 14:** Time-sequenced images over the length of the simulated area of, **(a)** wave thickness, and **(b)** temperature of the wall at every 5 ms [82]

4.2.2 Experimental Investigations

Recent annular flow experiments have highlighted the relationship between wall temperature and the passage of a disturbance wave [57], [84]. Su et al. worked with a saturated steam mixture at conditions where nucleate boiling does not occur, as the system was firmly in the regime dominated by forced convective evaporation [31]. Also of note, the experiments were

performed at qualities ranging between x=0.01—0.08 which is low for annular flow. Later publications confirmed that annular flow was always achieved at this low quality; however, translating these results to other annular flow experiments due to the considerable thickness of the liquid film [57]. Regardless, the authors found that wall temperature peaks at the wave front, and the heat transfer coefficient reaches its maximum immediately following the passage of a wave, resulting in a local minimum in the wall temperature, as seen in Fig. 15. Although the tests did not occur in the saturated nucleate boiling regime, these observations lend support to the hypothesis that temperature variations lead to nucleate boiling. In discussing the causes of these oscillations in temperature and heat transfer coefficient, the authors determined that the influence of turbulent eddies was insufficient to create the amplitude of the observed changes. Rather, it was postulated that the sharp changes in liquid film thickness cause bulk velocity variations. As the wave approaches, the liquid film thickness drastically increases, resulting in a large decrease in liquid velocity and heat transfer coefficient. Conversely, when the wave departs, the opposite will occur, and the heat transfer coefficient will rise. This hypothesis matches what is seen in the data collected but does not align neatly with experiments using thinner films. Other publications have suggested that thicker liquid films at low qualities should be treated differently than thinner, high quality, films due to the difference in velocity behaviors seen between the two [45]. In the forced convection regime, as very thin films begin to dry out, they become smoother which changes the friction factor between the liquid and vapor phase, but this behavior is not observed in thicker films like the ones shown in Fig. 15. This leaves room open for future experimental investigations into the effect of disturbance waves and heat transfer coefficient in very thin films, but, again, supports the theory that disturbance waves lead to local changes in the wall temperature.
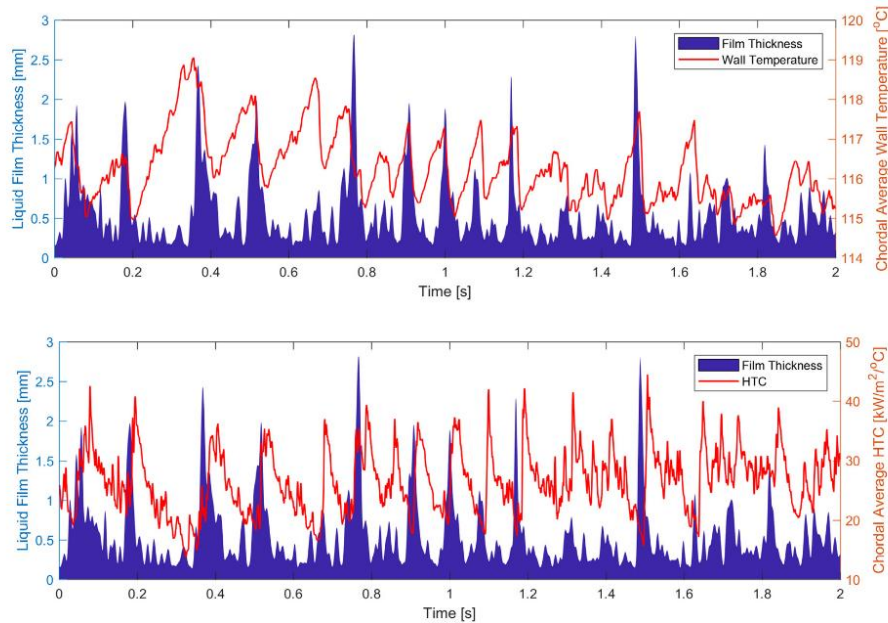
**Fig. 15:** Oscillations in temperature and heat transfer coefficient in relation to liquid film thickness [84]

## 4.3 Pressure Theory (Saturation Temperature Effects)

The pressure theory relies on the relationship between local pressure and saturation temperature. Further discussion of this theory first requires a deeper understanding of the relationship between saturation temperature and nucleate boiling which is applicable to all nucleate boiling flows and described by Charnay et al. [61]. In the region where nucleate boiling is dominant, vapor qualities tend to be low, and the heat transfer coefficient is independent of mass velocity but dependent on heat flux and saturation pressure. Once sufficiently high vapor qualities are reached, the flow becomes forced convection dominant, making the heat transfer coefficient less dependent on heat flux and more dependent on mass flux. At low vapor qualities, increasing the saturation temperature (by increasing the system pressure) results in a decrease in surface tension and an increase in the vapor-liquid density ratio $\rho_v/\rho_l$. These property changes intensify nucleate boiling, as discussed in *Chapter 3 Section 3.3*. Specifically, higher saturation temperatures increase in the number of active nucleation sites and a decrease in bubble radius at

the point of detachment which in turn decreases the average bubble sizes and the waiting period in the ebullition cycle.

The effects of saturation temperature are also dependent on the proximity of the saturation temperature to the critical temperature. For instance, with R245fa ($T_{crit}$ = 154.05 $^{o}$C) at high saturation temperatures (greater than 120 $^{o}$C), the contribution of nucleate boiling to heat transfer is significant even at high vapor qualities where convective boiling is typically dominant. This occurs because increased saturation temperature raises vapor density, yielding a decrease in vapor velocity. Additionally, the thermal conductivity of the liquid film decreases with increasing saturation temperature, reducing heat transfer due to conduction out of the wall and through the liquid film. With these two effects, both conduction and convection heat transfer are diminished in the flow, emphasizing nucleate boiling and delaying the switch to the forced convective boiling regime.

Beyond the liquid film properties, system pressure affects several other aspects of the flow. A notable relationship exists between pressure and the ratio of bubble-induced droplet entrainment mass loss rate from the liquid film to the total mass loss rate from the liquid film due to all modes of entrainment and vaporization. This mass loss ratio first increases with pressure, reaching a maximum value of 13% (13% of all mass lost from the liquid film is due to boiling-induced entrainment) at an operating pressure of 0.75 MPa [85]. The fraction then decreases to an absolute minimum of 4% at 4 MPa, followed by another increase up to approximately 7% of the mass loss at a pressure of 7 MPa [85]. One plausible explanation of this relationship is that liquid droplet ejection from bubble bursting is dependent on the pressure of the system. High-pressure flows have more active nucleation sites, higher vapor density, and a larger departure frequency [85]. These effects, however, are only observed at high system pressures and are not overly sensitive to

smaller local changes in pressure. As Barbosa acknowledges in his description of the pressure-induced boiling theory, disturbance waves only result in a change in pressure around 500 Pa [52], resulting from local volume reductions in the vapor core as the flow contracts over the length of a disturbance wave. For Barbosa's conditions, this deviation would only result in a minuscule change in bubble-induced droplet entrainment and is not large enough to significantly influence the number of active nucleation sites. While system pressure does play an influential role in nucleate boiling, the change in local pressure caused by a disturbance wave seems unlikely to create the significant increase in nucleate boiling observed by Barbosa through either change in saturation temperature or direct increases in boiling detected through changes in the bubble-induced droplet entrainment.

## 4.4 Bubble Entrainment Theory (Bubble dynamics)

To evaluate the bubble entrainment theory, the dynamic behavior of bubbles in thin film annular flow must be understood. An extensive study by Hann et al. explored bubble entrapment in a gas-shear liquid film [86]. While nucleate boiling is the most obvious mechanism for bubble formation, other flow factors can also yield bubbles. For example, small bubbles can become entrapped in the liquid film when droplets from the vapor core impact the liquid-vapor interface. These droplets move at, or close to, the speed of the vapor core and, if they have a transverse velocity, impact the liquid film at a shallow angle, creating a furrow in their wake. Many theories exist that explain how the droplet impact results in entrapped gas, but a clear answer has not been well agreed upon.

In addition to droplet impact, the disturbance waves can entrap vapor in the film. Observations of the portion of the flow just ahead of a disturbance wave reveal that many bubbles are generated through packets of liquid detaching from the crest of the disturbance wave and

colliding with the liquid film. The bubbles created from this mechanism are typically larger than those created by droplet impact. Smaller ripple waves or capillary waves can also entrap gas. As these waves overturn due to shear from the vapor core, pockets of gas are trapped under the liquid and form into groups of bubbles, some of which survive to be overtaken by disturbance waves. Small bubble groups are typically generated in the laminar region between disturbance waves and are quickly swept up into the large waves resulting in a clear increase in the number of bubbles seen in a disturbance wave as compared to the base film. Bubbles can, of course, slide out of the disturbance wave, but the thin film is generally not conducive to sustained bubble life, particularly for large bubbles.

While various mechanisms contribute to the addition of vapor bubbles into the flow beyond nucleate boiling, several mechanisms lead to bubble collapse. This collapse is typically the result of an external shock such as the collapse of nearby bubbles, droplet impact into the film, or the strong turbulent motion seen under the disturbance waves. Additionally, if a large bubble moves into a region of the film where the diameter is larger than the film thickness, the bubble will quickly collapse. When these larger bubbles burst, they may form multiple smaller bubbles or entirely disappear. The probability density function of the size distribution of bubbles in an air-water flow (attributable solely to bubble entrainment since the wall is unheated) is shown in Fig. 16. The influence of the thin film can be seen as bubbles larger than the base film are unlikely; they can only survive within disturbance waves. Smaller bubbles are seen more frequently because they have a higher likelihood of surviving, and more mechanisms exist which create small bubbles including the collapse of larger bubbles. For reference, the mean film thickness is around 0.33 mm, but no exact value is given by the authors.
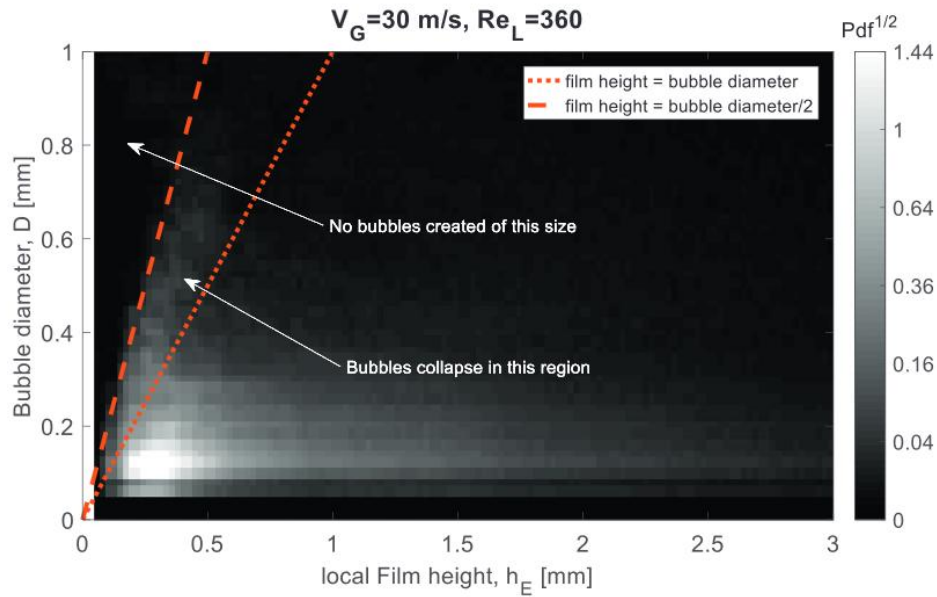
**Fig. 16:** Probability density function of bubble diameter as compared to local liquid film height in an air water flow [86]

When examining the bubble entrainment theory, it is important to note that this phenomenon was explicitly not observed in Barbosa's experiments. Nor, to the authors' knowledge, is there significant evidence of microbubbles attaching to the heated wall in other literature. As illustrated in Fig. 17 (a) and (b), the velocity of bubbles is clearly subject to the surrounding liquid. Disturbance waves have a higher velocity than the base film which is mirrored by the velocity of the bubbles. Given the nature of a probability density function, Fig. 17 (a) does not suggest that no bubbles have zero velocity, rather, few were observed. A small portion of the bubbles in both the base film and the disturbance waves have zero velocity which could be interpreted as bubbles attaching to the wall. Importantly though, there is not any significant increase in the number of zero velocity bubbles under a disturbance wave as compared to the laminar region which would be expected by the bubble entrainment theory. This experiment was conducted for an air-water flow without nucleate boiling, so there is the possibility that the

presence of vapor embryos in the cavities of the wall could lead to increased bubble attachment to the wall, but current evidence does not suggest that many if any bubbles are attaching.
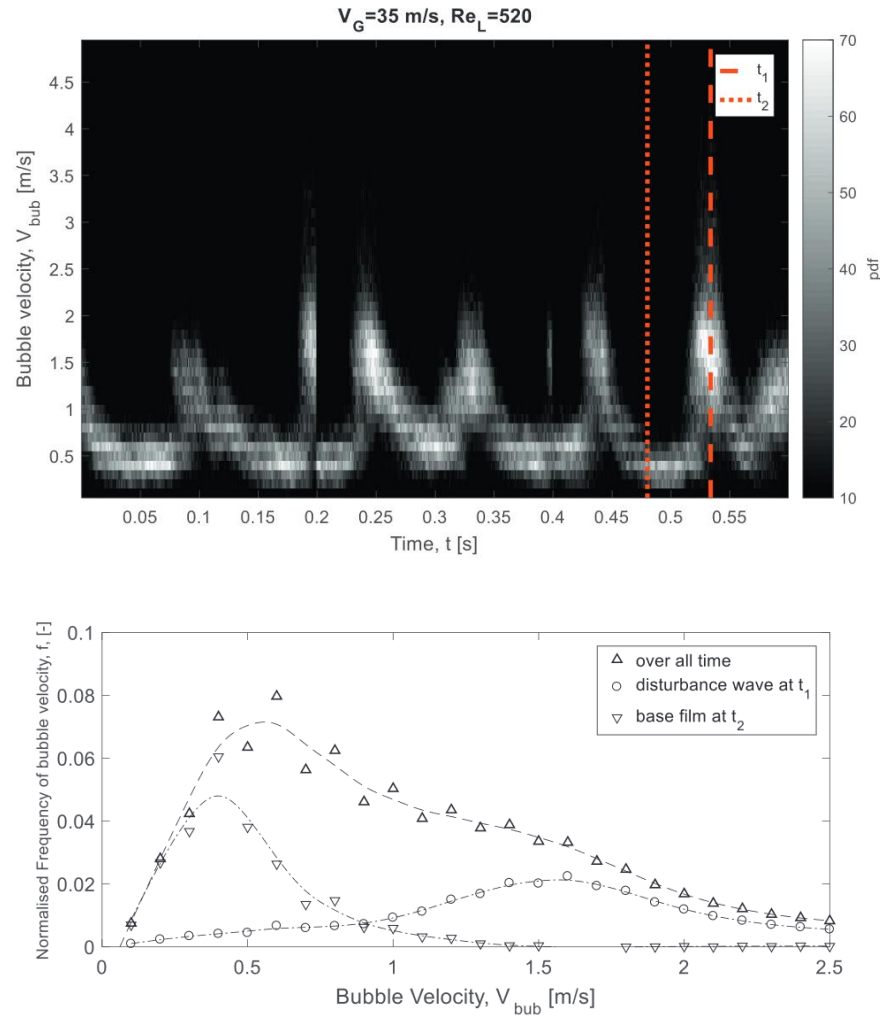


**Fig. 17: (a)** Probability density function of bubble velocities over time at ($t_1$) in the base film and ($t_2$) a disturbance wave in an air water flow, **(b)** Comparison of the frequency of velocity distribution under the base film ($t_1$) and the disturbance wave ($t_2$) [86]

## 5. Modeling of Nucleate Boiling Using Heat Flux Partitioning

Heat flux partitioning is a modeling approach that characterizes the contribution of individual sources to the total heat removed during nucleate boiling. Most generalized boiling heat transfer coefficient correlations lack the nuance of heat flux partition, capturing only the total heat transfer coefficient with meaningful reductions in accuracy when moving out of their empirical

database. However, experiments performed within the heat flux partitioning framework capture the dynamic nature of all heat transfer modes while progressing through flow regimes. With an understanding of all modes of heat transfer, it becomes possible to use these models in new, understudied fields such as thin film annular flow boiling.

There are many sources of heat flux associated with nucleate boiling. In a simple pool boiling system, these include the natural convective heat flux arising from temperature gradients in the liquid, quenching heat flux by transient conduction during the waiting period of the boiling cycle, and evaporative heat flux associated with latent heat during the liquid-to-vapor phase change [87]. The relative significance of each of these heat transfer mechanisms depends on the heat applied to the system. As the heat flux increases, the contributions of evaporation and quenching intensify while the impact of convection dwindles. Flow boiling introduces more heat transfer mechanisms. First, latent heat transport is typically broken into three components: evaporation of the liquid microlayer (as described in *Chapter 3 Section 2.1*), evaporation of the superheated liquid surrounding the bubble, and additional microlayer evaporation that occurs when the nucleated bubble slides along the heated surface by the liquid flow [49]. Compared to the 50-60% found in pool boiling, evaporation of the microlayer removes only about 33% of the total heat near critical heat flux conditions in subcooled flow boiling [88]. The nature of convective heat transfer also differs in flow boiling, as it is driven by forced convection rather than natural convection. While the distinction between these two forms of convection is well-established, the dynamics of heat transfer due to bubble movement introduce greater complexity.

Bubbles slide only when their maximum diameter is smaller than the space between nucleation sites; otherwise, they may merge with the neighboring bubble or inhibit nucleation in neighboring cavities [49], [54]. Merging may also occur if multiple bubbles slide at different

speeds, leading to a collision [20]. This merger alters the surface area available for liquid evaporation and alters the local temperature gradient leading to transient conduction [20]. The sliding bubble forces new cool liquid into the microlayer under the bubble, which rapidly evaporates given its minimal thickness. Sliding is particularly important to heat transfer at high pressures while bubble merger is more vigorous at low pressures [49]. A lack of experimental investigation into each of these heat transfer mechanisms makes it difficult to determine the breakdown of contributions, but it seems generally agreed that forced convection and evaporation dominate the heat transfer while transient conduction is a minor factor [20], [49].

Numerical heat flux partitioning models have been developed for subcooled flow boiling and pool boiling and compared to experimental data using correlations to determine unreported variables, but very few experiments have been developed from the ground up with a focus on heat flux partitioning [20], [21], [49]. This is likely due to the challenges associated with unobtrusively measuring each of the flow characteristics required for the application of the equations previously created. If the practice of heat flux partitioning is to grow, more work is needed to simplify each of the heat transfer equations so that they may be realistically applied to experimental data, allowing for direct measurement of variables to assess their individual impacts.

## 6. Conclusion

Nucleate boiling is a complex and not fully understood phenomenon that is increasingly obfuscated when extended into thin film annular flow boiling. Boiling occurs within the limiting thermal layer, where the liquid film is heated above the saturation temperature [54]. This thermal layer is primarily influenced by the balance between convective heat transfer and wall superheat, which is itself dependent on the thickness of the liquid thin film and the vapor quality in annular flows [45], [61], [62], [67]. Additional factors such as surface tension, saturation temperature,

pressure, liquid and vapor density, mass flux, incoming heat flux, and wall surface roughness all significantly change the presence and intensity of nucleate boiling [50], [61], [64], [67], [69], [70]. Together, these flow properties create an intricate balance between sustained nucleate boiling and the suppression of nucleate boiling through the shrinking of the thermal layer by forced convective evaporation at the liquid-vapor interface [53], [84].

Given the complexity of the flow regime, significant gaps remain in the understanding of nucleate boiling in thin film annular flow. Multiple authors have observed intense bubble nucleation in the wake of disturbance waves, but the fundamental mechanisms driving this increase have not been conclusively tested and proven [52], [57], [64]. The most extensively studied hypothesis is that waves change the local heat transfer coefficient, allowing for small areas of high superheat to be sustained for long enough to allow vapor embryos to progress through the boiling cycle [81], [82], [83], [84]. Another proposed mechanism suggests that pressure changes under the disturbance wave lead to increased nucleate boiling, but this theory has been mostly disregarded in current literature due to the insignificant pressure change observed over the passage of a large wave [61], [85]. A third theory asserts that powerful mixing inside disturbance waves could force entrapped bubbles into the superheated liquid close to the wall resulting in bubble growth [86]. Although the movement of bubbles within waves has been studied, the literature has not detected a significant number of bubbles attaching to the heated wall, and this phenomenon has yet to be observed in the context of nucleate boiling in annular flows.

In addition to previous experimental work, there have been efforts to model the contributions of nucleate boiling to the total heat transfer coefficient. These include correlation-based approaches [22], [23], [54], [72], and the heat flux partitioning methods [20], [21], [49], [87]. Many current studies focus on developing correlations specific to the studied flow regime.

However, adopting heat flux partitioning could lead to a better understanding of all heat transfer components, paving the way for a more universally applicable model. An accurate prediction method describing the conditions at which nucleate boiling occurs would represent a huge leap forward in the collective understanding and modeling of two-phase annular flow. This understanding, however, will not come without the formation of a detailed and varied experimental database developed with particular attention paid to direct measurement of all individual flow phenomena.

# CHAPTER 4: EXPERIMENTAL OBSERVATION OF NUCLEATE BOILING

## 1. General Boiling Conditions

Nucleate boiling in thin film annular flows is a complex phenomenon. *Chapter 3* provides a detailed analysis of many flow characteristics and their impact on nucleate boiling. In summary, convective evaporation at the liquid-vapor interface prevents superheating within the liquid film, thereby suppressing nucleate boiling. However, in thicker liquid films, the increased thermal resistance between the heated wall and the liquid-vapor interface allows for local superheating, permitting nucleate boiling. Local superheating may also be achieved by simply increasing the wall heat flux. Additionally, the passage of disturbance waves significantly alters the intensity of nucleate boiling. As observed by Barbosa et al., fully suppressed nucleation cavities may become briefly activated by the passage of a disturbance wave [52]. Although the exact mechanism remains uncertain, it is likely that the disturbance wave increases the liquid film superheat thereby enhancing bubble nucleation. Fig. 18 illustrates the importance of heat flux and disturbance waves. The set of images clearly shows how bubble density and diameter increase under a disturbance wave as the input heat increases from 0 W up to 1200 W.
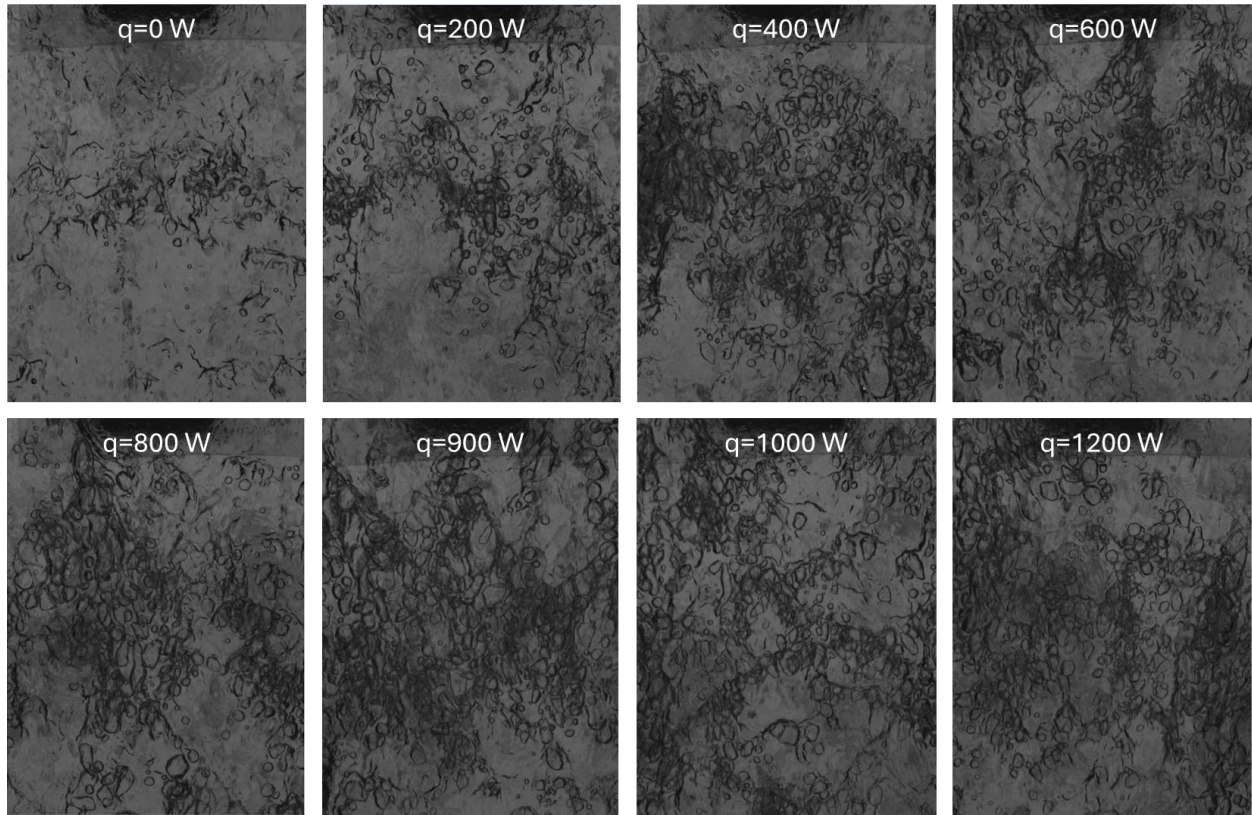
**Fig. 18:** Images of a disturbance wave as heat flux is increased from 0 to 1200 W at an inlet quality of 0.342 and mass flux of 176 kg/m$^2$-s

True nucleate boiling was only observed under conditions that produced the thickest or slowest moving liquid film at the highest achievable heat flux. This occurred at an inlet vapor quality $x_{in}$=0.342, a mass flux of 176 kg/m$^2$-s, and a heat flux of 63.5 kW/m$^2$ (1200 W). Under these conditions, only three active nucleation sites were observed within an approximately 5 cm long viewing area, suggesting that the current experimental setup can reach the threshold of nucleate boiling. Achieving more extensive nucleate boiling in future experiments would require a larger liquid pump, a larger power supply, and/or surface modifications to produce a wider range of nucleation cavity sizes. Equipment limitations are discussed in the *Appendix A*. The boiling surface suggestion stems from the fact that the coated surface is exceptionally smooth, which is not conducive to nucleate boiling. Increasing surface roughness would provide more possible

nucleation cavities and could facilitate boiling without modifications to the pumps or power supplies.

Importantly, nucleate boiling is not the sole source of vapor within the liquid film. The high vapor core velocity causes droplets to deposit into the liquid film at a shallow impact angle, creating a furrow in their wake. Hann et al. have identified this mechanism as a means of entrapping vapor in the liquid film [86]. High-speed videos frequently capture droplets impacting the liquid film, followed by bubble growth in their wake in the succeeding frames. These bubbles are detached from the wall and are not the result of nucleate boiling. While nucleate boiling was only observed at a singular condition, bubble growth was present across all test conditions with an applied heat flux. A similar vapor entrapment mechanism, theorized in the literature to occur through wave rollover, was not explicitly observed in these experiments.

In the experimental setup, the liquid film is saturated without an applied heat flux, meaning a few bubbles persist in the liquid film without external heating. These bubbles, which must originate from droplet deposition, constitute most of the void within the liquid film. Supporting this, bubble size and density decrease as droplets transition to a finely dispersed mist at higher core Weber numbers, consistent with the findings of Cioncolini and Thome [89]. This transition is evident in Fig. 19 as there is a reduction in average bubble diameter with increasing mass flux as inlet vapor quality and heat flux are held constant.
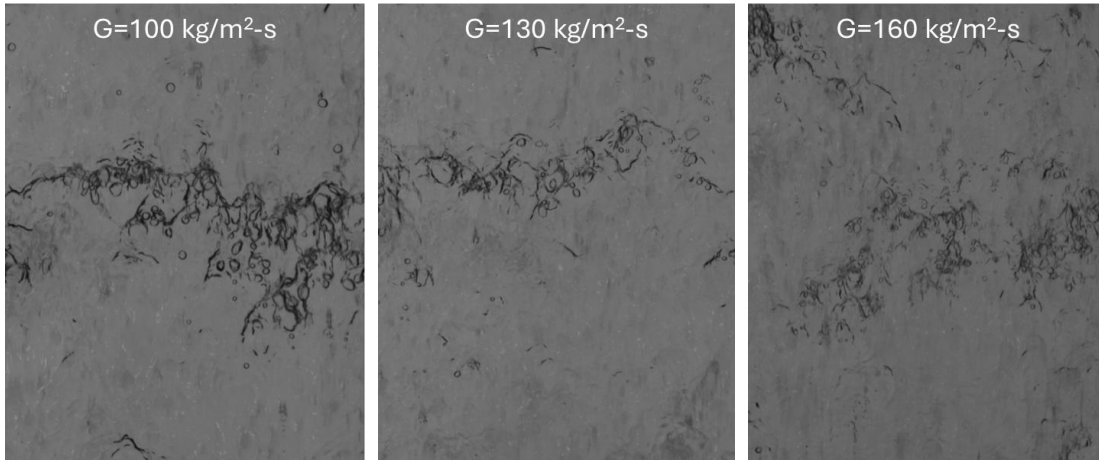
**Fig. 19:** Test section images at varying mass flux while inlet quality and heat flux are held constant at 0.63 and 31.7 kW/m$^2$ respectively.

While these observations pertain to regions upstream of the cylindrical obstruction, the recirculation region in its immediate wake creates unique conditions for bubble growth. The contact line between the recirculation patterns and the free-stream area (the intersection between regions 2 and 5 as seen in Fig. 30) exhibits significant bubble growth. These bubbles remain mostly stationary, experiencing conditions more like pool boiling, which leads to rapid growth. The obstruction generates substantial turbulence and alters the droplet deposition rate in the wake region, likely contributing to excessive vapor formation. However, across all sections of the test region, bubbles appear to follow existing flow paths without significantly altering the overall flow dynamics.

## 2. Disturbance Wave Effects

The video accompanying this work titled, "Wave Nucleate Boiling", highlights the critical role of disturbance waves in nucleate boiling. In the video, nucleation cavities (circled in red), oscillate between active and suppressed depending on the local film thickness. As a wave passes, the nucleation cavities activate, producing a significant volume of vapor. Conversely, in the thin base film between waves, the cavities are largely suppressed. Another notable feature of the video

is the volume of bubbles contained within disturbance waves. In the thin base film, bubbles quickly burst as their diameter approaches the film thickness. However, disturbance waves are relatively thick, allowing large-diameter bubbles to persist. Fig. 20 presents the approximate ratio of void area to the total frame area for a video at a mass flux of 176 kg/m$^2$-s, inlet vapor quality of 0.342, and a heat flux of 63,492 kW/m$^2$ captured at 4000 fps. The passage of disturbance waves corresponds to an increase in void area. At very high heat flux, bubbles occupy a significant portion of the volume beneath a wave. These bubbles typically measure a few millimeters in diameter but rarely coalesce, preventing departure from nucleate boiling type critical heat flux under the waves.
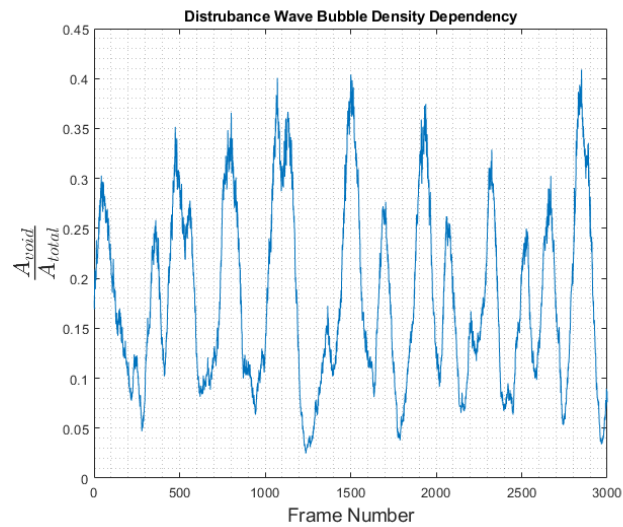


**Fig. 20:** The ratio of void area to total frame area for a thick film at high heat flux

# CHAPTER 5: OBSTRUCTED ANNULAR FLOW

## 1. Introduction

This chapter is a copy of the article submitted to the International Journal of Heat and Fluid Flow under the title "Film Dryout Behavior in Obstructed Annular Two-Phase Flow" with minor formatting modifications. A description of authors respective contributions are as follows:

- Joseph Farrell: Conceptualization, Software, Formal analysis, Investigation, Data curation, Writing – original draft, Writing – review & editing

- Jason Chan: Formal analysis, Methodology, Software, Investigation, Data curation, Writing – review & editing

- Roman Morse: Conceptualization, Writing – review & editing

- Evan T. Hurlburt: Conceptualization, Project administration, Funding acquisition

- Arganthaël Berson: Conceptualization, Writing – review & editing, Supervision

- Allison Mahvi: Conceptualization, Writing – review & editing, Supervision

To specify, all data was gathered, analyzed, and reported by the primary author of this thesis. Similar work may be found in the Jason Chan's thesis, but remains separate and distinct from the content discussed here. The flow conditions used in the parametric study described in this chapter are summarized in Table 4.

**Table 4:** Experimental flow parameters used in full parametric study of the 2.5-mm and 1.25-mm diameter obstructions. The heat fluxes were varied for each test from 0 kW/m$^2$ to the value shown in the table. All data were collected at a 25 °C refrigerant saturation temperature.

|  |  | Mass Flux (kg/m$^2$-s) | | |
|---|---|---|---|---|
|  |  | 130 | 150 | 170 |
| Inlet Quality (-) | 0.63 | 27.8 kW/m$^2$ | 22.5 kW/m$^2$ | 29.1 kW/m$^2$ |
|  | 0.70 | 23.8 kW/m$^2$ | 21.2 kW/m$^2$ | 25.1 kW/m$^2$ |
|  | 0.77 | 17.2 kW/m$^2$ | 18.5 kW/m$^2$ | 19.8 kW/m$^2$ |
|  | 0.83 | 17.2 kW/m$^2$ | 15.9 kW/m$^2$ | 15.9 kW/m$^2$ |
|  | 0.90 | 13.2 kW/m$^2$ | 10.6 kW/m$^2$ | 13.2 kW/m$^2$ |

## 2. Results and Discussion

The results of the parametric study (Table 4) are presented in three sections for a large (*D* = 2.5 mm) and small (*D* = 1.25 mm) obstruction. The fundamentals of the liquid flow behavior downstream of the obstruction including the size, shape, and location of dryout region are discussed in *Chapter 5 Section 2.1*. Film thickness measurement data are used in conjunction with a qualitative evaluation of high-speed video data to resolve the root cause of premature dryout in *Chapter 5 Section 2.2*. Finally, the temperature response on the heated wall with subsequent calculations of HTC are discussed in *Chapter 5 Section 2.3*.

### 2.1 Obstruction Wake Behavior

The disruption of the thin film liquid flow by the obstruction consistently generates a parabolic-shaped wake with multiple distinct regions of the flow. This section identifies and describes the wet wake flow field as well as the incipience and growth of the dry region.

2.1.1 Wake Shape and Flow Regions

The liquid flow field can be split into the five regions identified in Fig. 21. As the regions can be difficult to immediately distinguish in images of the test section, Fig. 21(a) emphasizes each flow region schematically. To provide reference to the actual flow, Fig. 21(b) shows an image of the test section during operation. Additionally, example high speed video of the wake can be

seen in Appendix C. Region 1 is located upstream of the obstruction and remains undisturbed by its presence, exhibiting the same behaviors as unobstructed flow. Region 2, immediately downstream of the obstruction, is a recirculation area like that observed in single phase flow around a cylinder. Region 3 is the calmest region, characterized by minimal wave or recirculation activity. The base film in region 3 is being vaporized but not replenished by disturbance waves and eventually dries out (region 4). The dryout area is parabolic with relatively stable side walls and a jagged, oscillating rewetting front at the trough of the parabola. Region 5 is the downstream area that has largely escaped the effects of the obstruction. The obstruction flow area restriction causes the liquid to accelerate, but otherwise, the film in region 5 is comparable to that observed upstream of the obstruction. Contrary to regions 2 and 3, there is significant wave behavior in region 5.
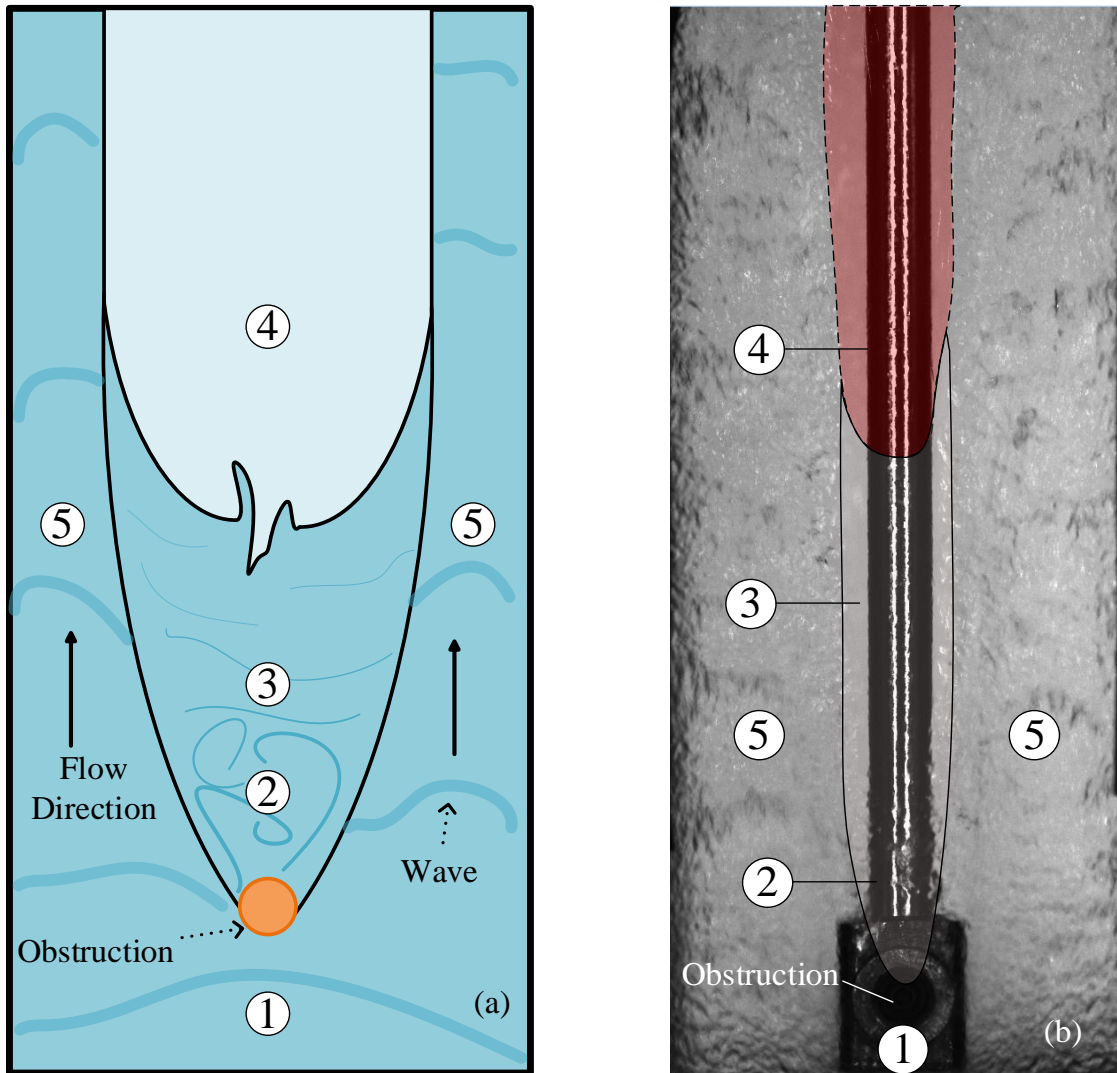
**Fig. 21:** (a) Illustration of flow around a cylindrical obstruction with prominent flow regions numbered, (b) Image of the test section with the large obstruction at $x_{in}$=0.80, $G = 150$ kg/m$^2$-s, $q''_{eff} = 13$ kW/m$^2$. The dry wake region is highlighted in red.

As the film moves downstream and the recirculation patterns decay, a calm wake region forms behind the obstruction (region 3), visually free of droplet impingement or large disturbance waves. As will be seen in *Chapter 5 Section 2.2,* the liquid film is thinner in this region than the adjacent flow outside the wake (region 5). Interestingly, the wake structure seen in Fig. 21 (a) and (b) closely resembles the single-phase flow diagram shown in Fig. 2, indicating that there is similarity in the general flow structure with the well-understood single-phase. Based on previous

literature concerning single-phase flow, it would be expected that turbulent mixing and viscous interaction between the low-pressure wake and high-pressure free stream would drive the flow toward velocity and thickness uniformity after contact with an obstruction. However, in the present investigation, viscous interactions between the wake and free stream are not strong enough to force assimilation in the flow within the visible range. In fact, when the film is heated, the velocity gradient becomes more pronounced as the liquid film loses mass and progresses downstream. Any turbulent oscillations are not large enough to force the liquid film back into the wake region, meaning there are no evident forces to drive uniformity in the flow after contact with the obstruction. High-speed videos showing the wake behind the obstruction as well as the recirculation region of both obstructions are available in Appendix C.

### 2.1.2 Dry Wake

As the film continues to move away from the obstruction, a dry region forms with sufficient heat flux (region 4). The dryout is sustained without rewetting from either waves or droplet impingement. The dryout region is U-shaped, analogous to the theoretical low-velocity wake profile of a cylindrical obstruction in single-phase flow, as illustrated in Fig. 2, and the parabolic dry arch from gravity-driven flows around an obstruction [37], [42]. While no direct velocity measurements of the film in the wake region were performed due to the complex liquid film behavior and lack of distinct trackable features, qualitative evaluation of wave velocity around the wake region using the high-speed video suggests a velocity profile resembling Fig. 2.

The location and width of the dry region depend on experimental conditions. Dryout always initiates at the farthest point downstream of the obstruction observable in the test section, beginning as a thin parabola confined near the centerline of the wake. The height and width of the dry region can be increased by decreasing mass flux, increasing obstruction diameter, increasing

heat flux, or increasing inlet quality. These trends are shown in Fig. 22 and Fig. 23. The wake width and heat flux at all test conditions and measurement points can be seen in Appendix B. Comparing the dry wake region of the larger obstruction to the dry wake region of the small obstruction reveals several key differences:

- Dryout area increases with obstruction diameter
- Dryout is observed only at higher tested inlet qualities with the smaller obstruction
- When present, the wake width of the smaller obstruction is narrower than that of the larger obstruction given the same conditions.

These observations align well with the differences in wake size when varying obstruction diameter in a gravity-driven flow [39], [43]. It should be noted that the measurements of wake width come from a manual analysis of only a small portion of the total images taken of the flow. The dry wake will have some variance which may not be captured in the averaged image used. Thus, the qualitative aspects of dry wake width area are accurate, but the quantitative measurements are subject to a certain degree of bias and error.
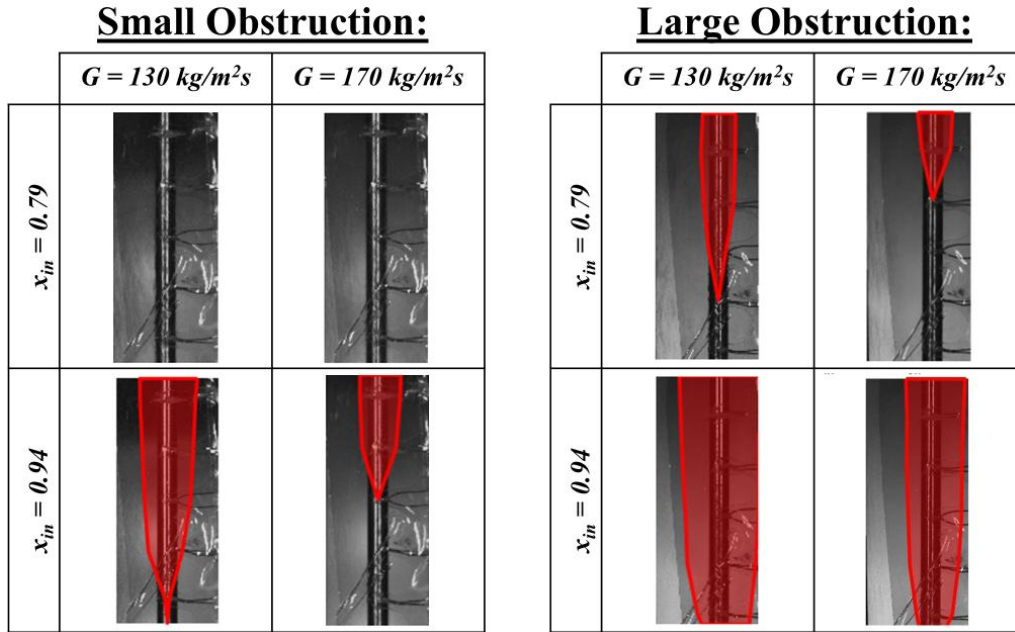
**Fig. 22:** Images downstream of the obstruction with red denoting the dryout region. The effective heat fluxes for the cases shown are between 12.5 and 13 kW/m$^2$.
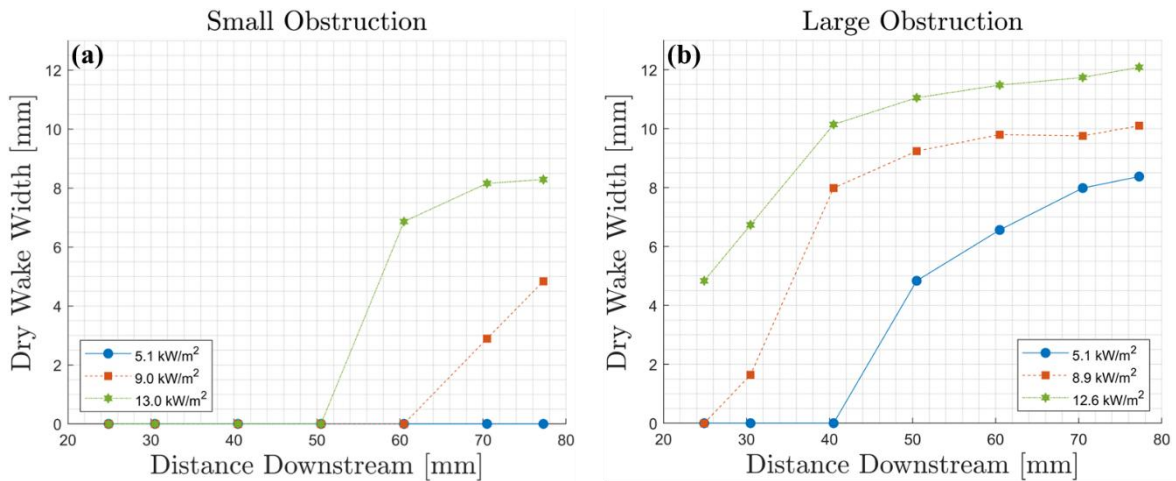


**Fig. 23:** Comparison of width of dry wake regions at different streamwise positions far downstream of the (a) small and (b) large obstructions, for an inlet quality of 0.94, and inlet mass flux of 170 kg/m$^2$s. The wake width for all conditions tested is shown in Appendix B.

## 2.2 Liquid Film Behavior

While dryout is the same shape between the large and small obstructions, dryout occurs at lower heat fluxes for the large obstruction than the small obstruction, and at much lower heat fluxes than unobstructed flows. Two factors combine to create the premature dryout in obstructed flow:

a significant reduction in average film thickness downstream of the obstruction, and the absence of disturbance waves in the wake region.

2.2.1 Liquid Film Thickness

In gravity-driven thin film flow around an obstruction, there is a sizable decrease in film thickness downstream of the obstacle [40], [42], [43]. This trend is also seen in annular flows as illustrated in Fig. 24(a), where the film thickness in the wake of the obstruction (region 3) is noticeably reduced compared to the upstream flow which can be used as a parallel for unobstructed flow. Time-averaged measurements over two seconds (4000 frames) indicate that the liquid film in the wake of the small obstruction is between 10-40% thinner than the upstream flow. For the large obstruction, the reduction is more pronounced, with the average film thickness decreasing by 60-80% depending on the mass flux. Previous literature has established that liquid films thin before dryout, a process accelerated in the wake of an obstruction, as evidenced by the sharp increase in dry area with decreasing film thickness shown in Fig. 24(b) [2], [45]. Notably, Fig. 24(a) demonstrates the minimal effect exerted by both heat flux and inlet quality, particularly at low qualities and for the large obstruction. The flat-line behavior of the film thickness ratio suggests the upstream and downstream films thin at the same rate.

The effect of mass flux on dryout can also be seen in Fig. 24(b). As the mass flux increases, the dry area decreases for the same conditions. This observation agrees with Ami et al. and suggests that the obstructed flow characteristics are dependent on the liquid film Reynolds number [31]. Previous work has shown that the increased mixing of highly turbulent flows promotes film thickness uniformity or increases film thickness through enhanced droplet deposition, overpowering any thinning caused by the obstruction [30], [32], [35]. Additionally, the length of the turbulent recirculation region in the immediate wake of the obstruction is proportional to the

Reynolds number [29]. Ultimately, an increase in turbulence decay distance downstream of an obstruction results in the suppression of dryout over a longer distance [30].

In this experiment, premature dryout was observed as opposed to the CHF enhancement seen by Ami et. al and Zahlan [30], [31]. As can be seen in Fig. 24(b), incoming Reynolds number appreciably influences dryout characteristics. Consequently, flows with high Reynolds numbers, as defined in equations (12) and (13), in previous experiments should be expected to dry substantially differently than the current investigation (inlet $Re_{tp}$<9100 in this study as compared to inlet $Re_{lo}$>40960 in Zahlan) [30].

$$Re_{lo} = \frac{G * D_i}{\mu_l} \tag{12}$$

$$Re_{tp} = \frac{\rho_l * D_h * (j_v + j_l)}{\mu_l} \tag{13}$$

$$j_v = \frac{G * x}{\rho_v} \tag{14}$$

$$j_l = \frac{G * (1 - x)}{\rho_l} \tag{15}$$
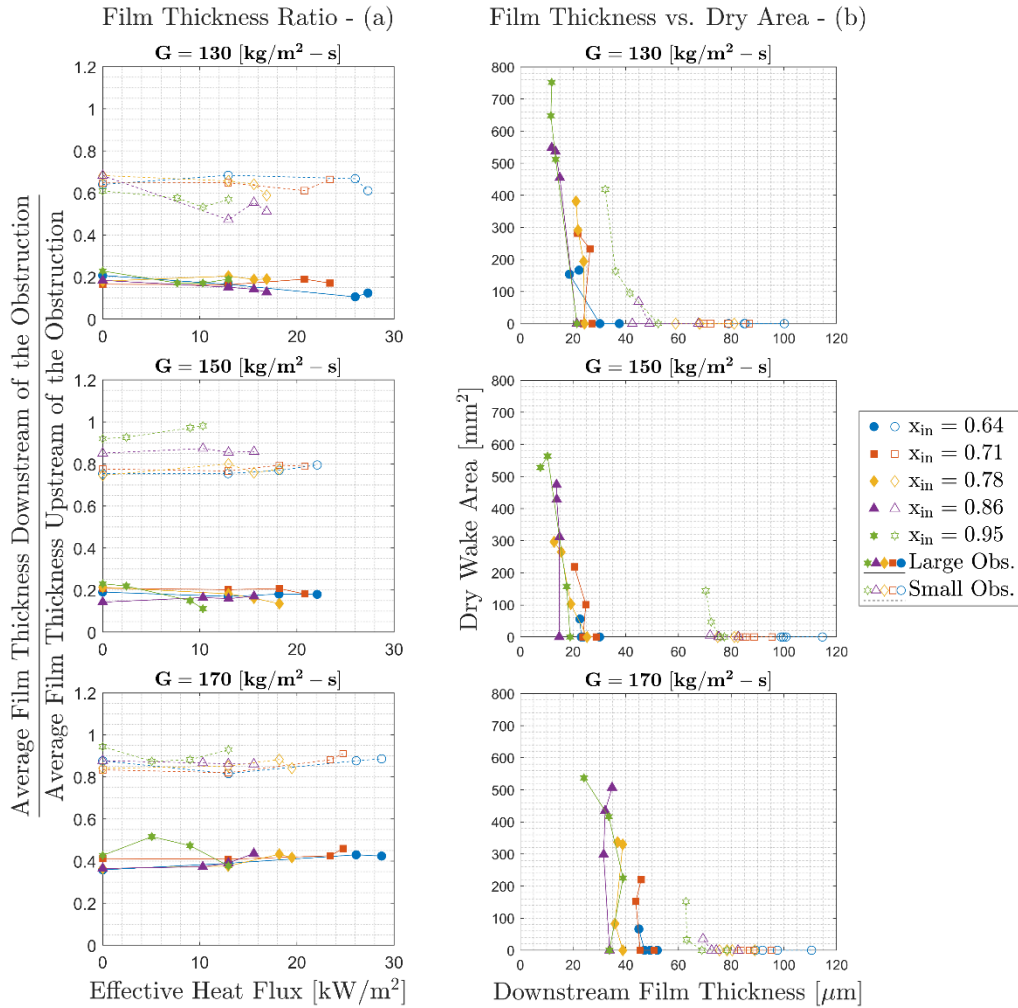
**Fig. 24:** (a) Ratio of downstream film thickness to upstream film thickness and (b) dry area dependency on downstream film thickness

2.2.2 Disturbance Wave Activity

Although the average film thickness can help explain the transition to dryout, the frequency and size of disturbance waves also has a strong influence [2], [4]. Any reduction in wave behavior will drastically lower the heat flux required for the onset of dryout. The separation of waves by the obstruction seen in high-speed videos can be quantitatively confirmed by comparing the film thickness standard deviation upstream and downstream of the obstruction which is a good indicator of wave activity [45]. Fig. 25 shows the standard deviation in film thickness as a function of the liquid film Reynolds Number defined as,

$$Re_{lf} = \frac{\rho_l \bar{u}_l D_{obs}}{\mu_l} \tag{16}$$

where $\bar{u}_l$ is the average upstream liquid velocity defined as

$$\bar{u}_l = \frac{G(1-x)(1-e)A_c}{\rho_l \Pi_{flow} \bar{\delta}_{up}} \tag{17}$$

The entrained liquid fraction, $e$, was found according to the method of Cioncolini and Thome [89]. To establish a consistent comparison point between obstruction sizes, the standard deviation of film thickness downstream of the obstruction shown in Fig. 25 was normalized by the time-averaged upstream film thickness which is consistent between obstructions.

Fig. 25 presents the standard deviation in film thickness upstream and downstream of the obstruction. The data gives multiple insights into the fluid mechanics of the liquid film around the obstruction. First, varying the obstruction diameter does not significantly influence the liquid film upstream. Second, at a given upstream film Reynolds number, the downstream normalized values for both obstruction sizes are significantly smaller than their upstream counterparts. Moreover, the diameter of the obstruction influences the extent of this reduction. The small obstruction sees a 20-30% reduction in normalized standard deviation whereas the large obstruction creates a more substantial 40-60% reduction. Third, increasing mass flux yields a larger normalized standard deviation downstream of the obstruction with no significant influence on upstream values when comparing points at the same film Reynolds number.
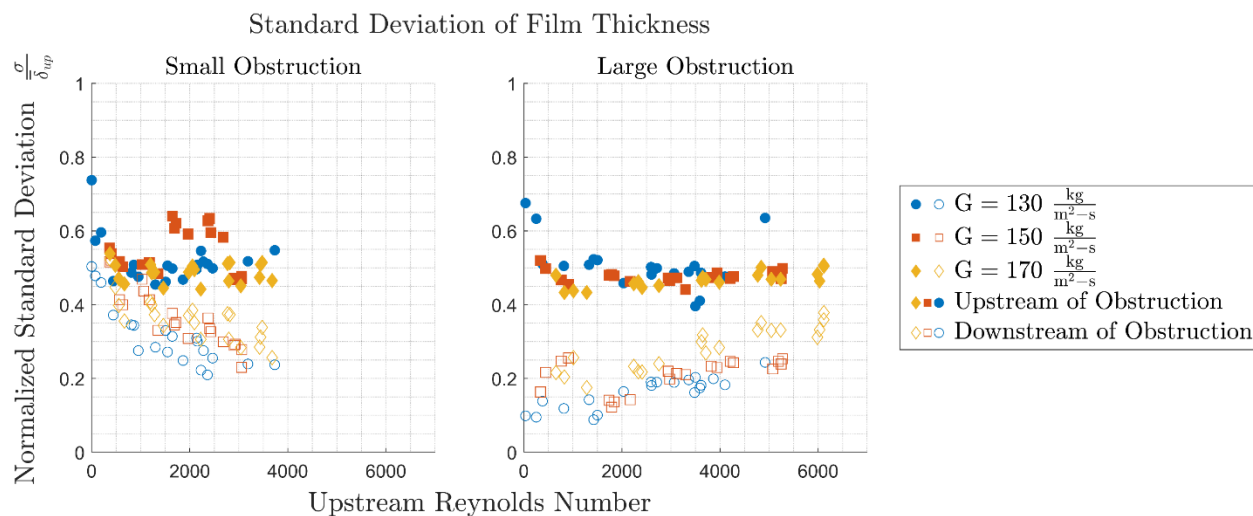
**Fig. 25:** Normalized standard deviation of film thickness downstream of the obstruction normalized by mean film thickness upstream of the obstruction.

The large obstruction demonstrates a positive correlation between the normalized standard deviation downstream and liquid film Reynolds number. Interestingly, this trend does not continue with the small obstruction which shows no positive correlation with the film Reynolds number. Instead, downstream of the small obstruction appears to mirror the standard deviation behavior seen upstream of the obstruction. While the presence of an obstruction consistently reduces wave activity as seen through a reduction in standard deviation, the extent of the reduction appears to be related to obstruction size.

## 2.3 Wall Temperature Behavior

The behavior in the wake region has a significant impact on the thermal characteristics of the flow. The liquid film's response to heat flux can be quantitatively observed through the external thermocouples placed downstream from the obstruction (Fig. 63). The external wall temperature measurements in this parametric study reveal that the wall temperature response to a dryout event does not match what has been observed previously for unobstructed flow. In unobstructed flow, the liquid film thins before eventually rupturing, creating a fast-growing dry area in the streamwise direction. The dry region is usually large, with an unpredictable shape, and can be rewet by

disturbance waves unless the incoming heat flux exceeds the CHF [2]. In the obstructed flow studied here, the wall temperature behaves as if a series of increasingly severe sustained dryout events occur as the heat flux increases.

### 2.3.1 Wall Temperature Time Trace

Fig. 26 shows a time trace of the wall temperature evolution with increasing heat flux. The plot illustrates the temperature response for the large obstruction at mass flux $G=150$ kg/m$^2$-s and inlet vapor quality of 0.86. At the beginning of the experiment, all wall temperature measurements increase synchronously with increasing heat flux until t=85 seconds, at which point the most downstream position starts to increase rapidly compared to the rest. The onset of heat transfer degradation occurred during this time as the effective wall heat flux reached 7.75 kW/m$^2$. When the wall heat flux is increased to 15.5 kW/m$^2$, the wall temperature at the farthest downstream measurement location (TC$_{ext,5}$) is approximately 22 $^o$C higher than the most upstream temperature measurement (TC$_{ext,1}$). Over the course of heating, the dry wake area (region 4) grows upstream towards the obstruction which is reflected in the temperature data. When the wet-dry interface passes each measurement point, the heat transfer coefficient at that point drastically decreases, resulting in a spike in temperature.
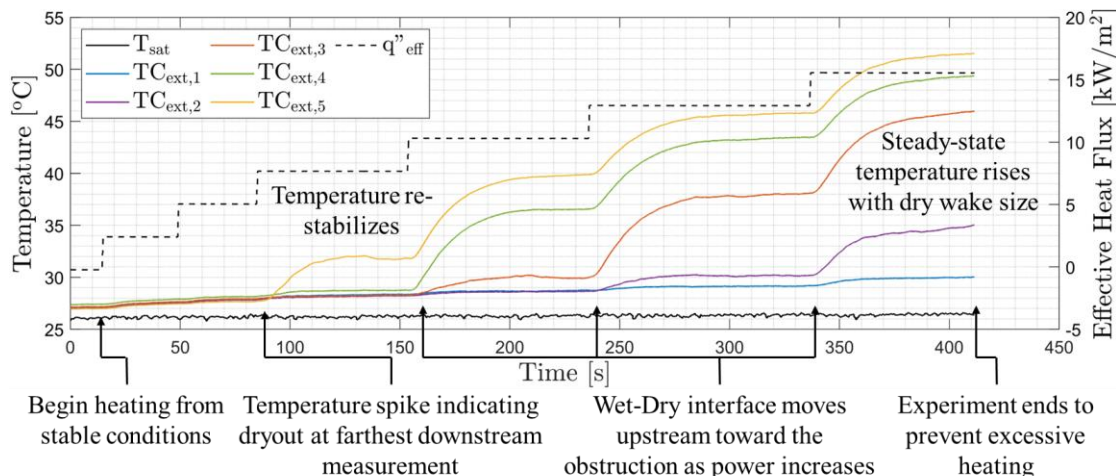
**Fig. 26:** Time trace of the effective heat flux and external wall temperatures at $x_{in}=0.86$ and $G=150$ kg/m$^2$-s for the large obstruction.

A key feature of the wall temperature downstream of the flow obstruction is its tendency to increase and reach a steady-state temperature for a given wall heat flux. This behavior contrasts with unobstructed flow, where dryout is typically accompanied by sudden thermal runaway. For example, at conditions similar to Fig. 26 without a flow obstruction, the external wall temperature stays within 5 $^o$C of the saturation temperature for effective wall heat fluxes ranging from 0 - 22 kW/m$^2$. However, past 22 kW/m$^2$, the wall temperature increases sharply and would reach a steady-state temperature far exceeding anything observed in this study [2]. As described previously, obstructed flow leads to a progressively increasing U-shape dry region without rewet which creates the plateauing temperature effect. In contrast, unobstructed flow dryout is spontaneous over a large area of the heated window, with the temperature rise occurring when disturbance waves are no longer able to rewet the surface yielding sustained large area dryout [2]. This transition from a high HTC to a lower HTC that leads to an increase in wall temperature is typically termed the critical boiling transition by the Nuclear Regulatory Commission [5]. An obstructed flow may technically achieve CHF or critical boiling with a sustained dry area by this definition, but not necessarily exhibit a total degradation in HTC.

2.3.2 Heat Transfer Coefficient

Fig. 27 shows how quality, heat flux, obstruction diameter, and downstream location affect the heat transfer coefficient, HTC, which is calculated as,

$$HTC = \frac{q''_{eff}}{(T - T_{sat})} \tag{18}$$

where $T$ is calculated from the external wall temperature measurement, considering losses to the surroundings and resistance through the window. As heat flux increases, conditions with a lower inlet quality and measurement points closer to the obstruction experience little to no HTC degradation. In fact, there is generally an increase in HTC as heat flux is increased which can be attributed to the thinning of the liquid film, reducing heat transfer resistance through the liquid [4]. On the other hand, high inlet quality experiments dryout with little applied heat, resulting in a sharp decrease in the HTC. In all cases, HTC degradation is more extreme and occurs at a lower heat flux at locations farther downstream of the obstruction. At these locations, the local quality is higher, resulting in a thinner film more susceptible to large area dryout in the wake.
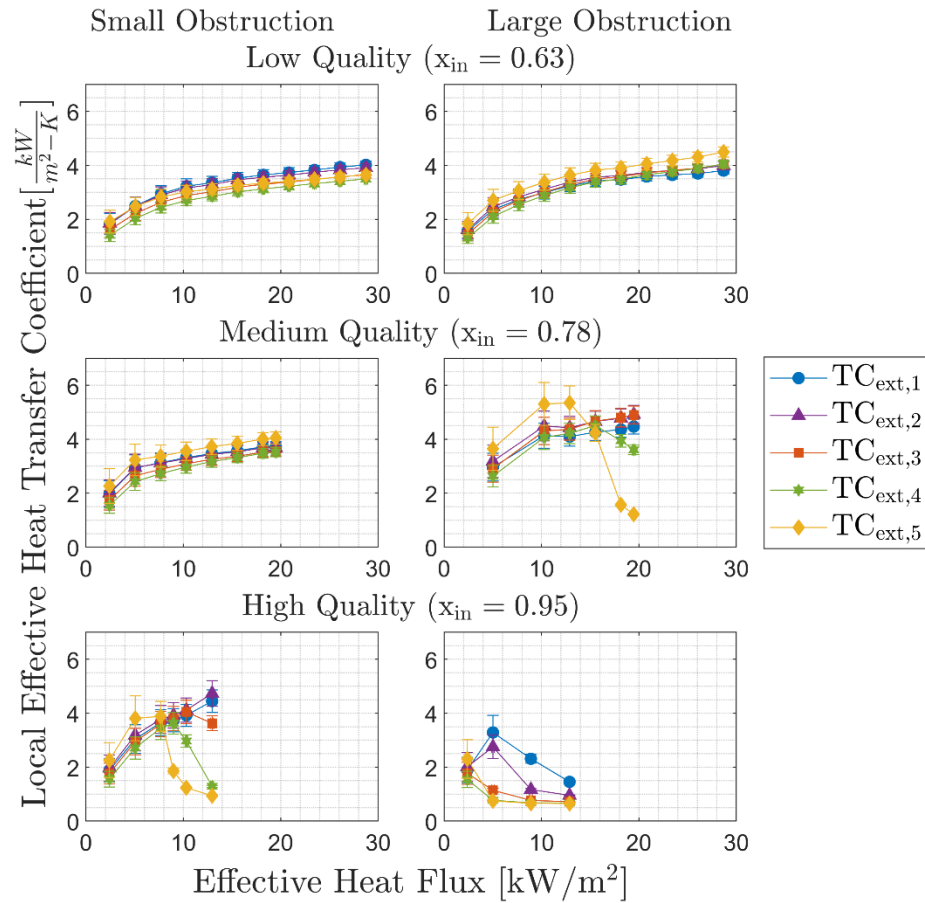
**Fig. 27:** Heat transfer coefficient degradation at each external temperature measurement point at low, medium, and high qualities ($x_{in}$=0.63, $x_{in}$=0.78, $x_{in}$=0.95) for the large and small obstruction at G=170 kg/m$^2$-s.

A direct comparison of the exterior wall temperature at all conditions tested for the small obstruction, large obstruction, and unobstructed flows can be seen in Fig. 28. Of particular importance in Fig. 28 is the slope of each temperature difference line. When there is no dryout, as is the case in most unobstructed and small obstructed points, the temperature difference increases linearly with heat flux with a small slope. When dryout occurs, there is a spike in $\Delta T_{ext}$, and the relationship between temperature and heat flux deviates from the consistent, linear values seen in wet conditions. In unobstructed flows, the slopes of the temperature lines closely resemble those for the small obstruction before dryout occurs. This similarity is not seen between the large

obstruction and unobstructed flows, showing a progression in temperature behavior toward unobstructed flow as obstruction diameter is reduced.
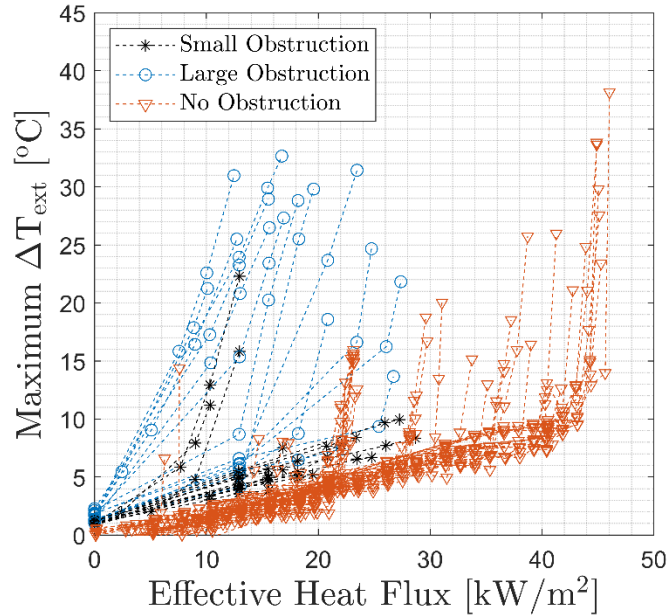


**Fig. 28:** Comparison of wall temperature increase versus heat flux with and without flow obstructions where $\Delta T_{ext}=T_{ext}-T_{sat}$.

2.3.3 Conduction Length

The progressive degradation of the HTC in obstructed flow can be explained by considering conduction through the heated surface from the relatively hot dry area to the cooler wetted wall on the periphery of the flow. The magnitude of conductive heat transfer will depend on the resistance defined in equation (19).

$$R''_{cond} = \frac{L_{cond}}{k_w} \tag{19}$$

The conduction length, $L_{cond}$, can be defined as the distance from the temperature measurement point to the wet film (region 5) and the thermal conductivity, $k_w$, is that of the heated wall. In obstructed flows, the dryout region is typically confined to the wake of the obstruction rather than spread across the entire width of the test section. This limits the conduction length and results in a smaller temperature rise than might result from the relatively larger dryout observed in

unobstructed flows. The conductive resistance effect can be observed when comparing the HTC to the dry wake width as in Fig. 29. As the wake width increases, there is a trend towards a lower HTC. However, if the wake is relatively small, heat can be conducted with minimal resistance from the dry patch to the wetted area resulting in little to no HTC deterioration.
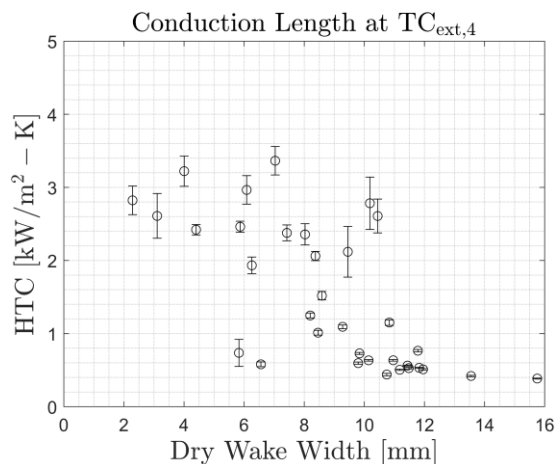


**Fig. 29:** The effect of conduction resistance at $TC_{ext,4}$ on HTC for the large obstruction.

## 3. Conclusion

This work provides insights into vertical upward two-phase annular flow around an obstruction and compares the results to unobstructed flows. The gathered data reveal a distinctive temperature pattern. Instead of a single large temperature spike resulting from rapid dryout in unobstructed flows, the obstructed flows show a series of progressively more severe temperature increases. These increases correspond to the size of the expanding dryout region. This temperature behavior is observed far downstream of the obstruction where high-speed videos show a sustained local U-shaped dry patch. The dry patch grows further upstream as the heat flux is increased. A parametric study conducted over various mass flow rates, inlet vapor qualities, and wall heat fluxes for a small and large obstruction characterizes the observed behavior. The results are divided into three parts: obstruction wake region imaging, measurement of the thin liquid film in the wake, and external wall temperature measurements.

The main conclusions from this work are as follows:

1. **Obstruction Wake Imaging:** Images of the dry wake region reveal that both obstruction diameters produce a similarly shaped parabolic dry patch, which forms far downstream of the obstruction. This dry patch remains confined within the wake, exhibiting minimal oscillation and no visible rewetting. Under identical conditions, the large obstruction generates a longer and wider dry region than the small obstruction. The size of the dry region is closely linked to the liquid film behavior, expanding as vapor quality increases and mass flux decreases.

2. **Liquid Film Behavior:** The most striking characteristic of the liquid film is that incoming disturbance waves are deflected toward the high-velocity region on the periphery of the flow without any restoring force to promote reassimilation into the obstruction wake. Additionally, the time-averaged wake film thickness is moderately thinner than the upstream film for the small obstruction and significantly thinner for the large obstruction. The premature dryout in the obstruction wake observed in this study is attributed to the absence of replenishing disturbance waves combined with reduced liquid mass available to vaporize.

3. **Wall Temperature Measurements:** Time traces of the wall temperature reveal the obstruction-induced effects on the downstream HTC. Increasing heat flux creates a series of plateauing temperature spikes proportional to the size of the dry region. The temperature rise in this sustained dry region may technically meet some definitions of CHF without a large degradation in HTC. The temperature response suggests a transverse conduction resistance related to the distance between the location measured in the dryout area and a wetted part of the wall. Examining the effect of obstruction size, the large obstacle

experiences HTC degradation at a lower heat flux compared to the small obstruction, consistent with the visual evidence of early dryout onset.

The data presented in this work clearly demonstrate that obstructed flows behave significantly differently than unobstructed flows, both in terms of liquid film dryout and the maximum temperatures experienced during those dryout events. Furthermore, the size of the obstruction plays a critical role in how the liquid film responds. By highlighting the interplay between obstruction-induced dryout behavior and thermal response, this work offers valuable insights for advancing predictive models of heat transfer in complex annular flow systems.

# CHAPTER 6: OBSTRUCTED ANNULAR FLOW WAKE DRYOUT WITH LIQUID FILMS CONDUCIVE TO NUCLEATE BOILING

## 1. Wake Shape and Flow Regions

The upgrades to the refrigerant flow loop, as outlined in *Appendix A*, enabled testing at lower inlet vapor qualities than previously possible. This reduction in vapor quality increases the liquid film thickness, which not only facilitates nucleate boiling, but also fundamentally alters the dryout behavior. The differences between the two flow regimes are shown in Fig. 30. Fig. 30 (a) represents the previously established dryout behavior for very thin liquid films, while Fig. 30 (b) depicts the newly observed flow regions for thicker liquid films. As the thinner liquid film flows have been described in depth in *Chapter 5*, this chapter will focus on the novel dryout mechanisms associated with thicker liquid films. All obstructed flow data in this chapter uses a 2.5 mm diameter cylinder as the obstacle.
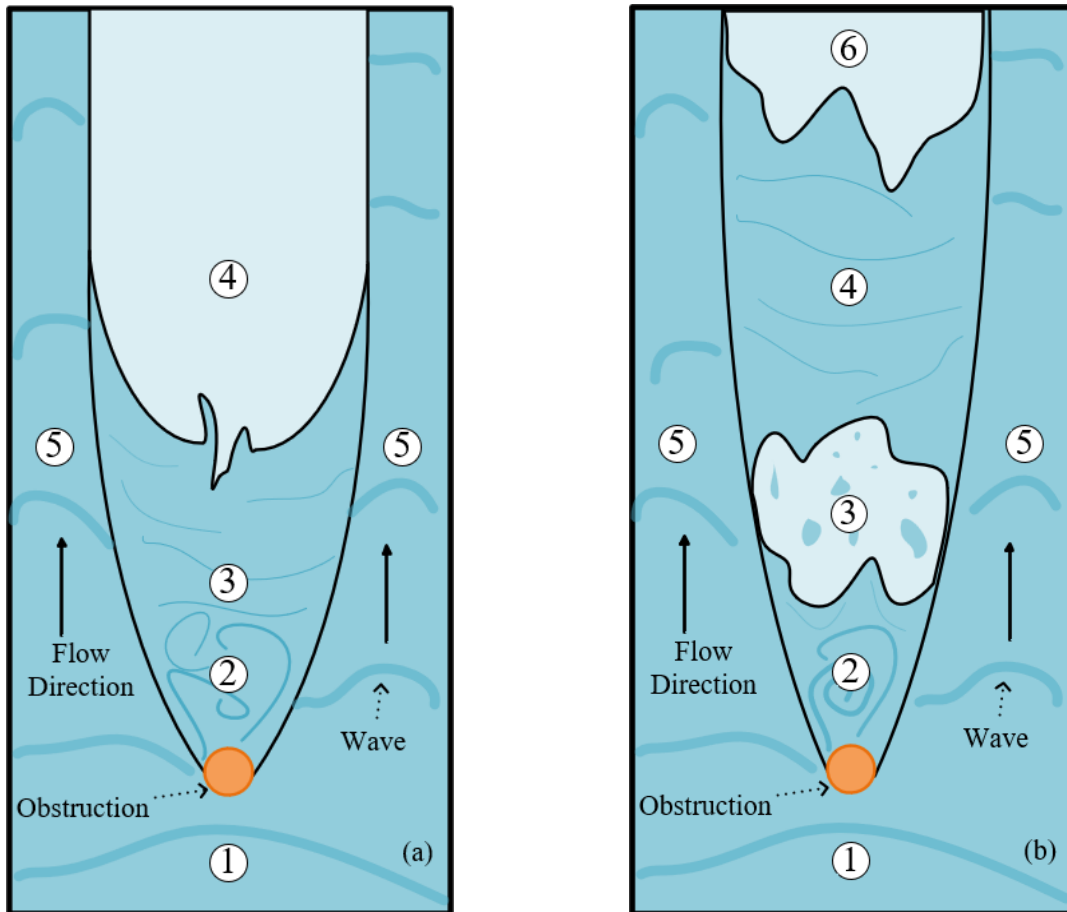
**Fig. 30:** Obstructed flow region diagram for (a) very thin liquid films ($x_{in} \gtrsim 0.6$) and (b) thicker liquid films ($x_{in} \lesssim 0.6$)

Region 1, located upstream of the obstruction, remains largely unchanged between the flow regimes. While differences in vapor quality and mass flow rate inherently affect the flow, the obstruction itself does not significantly influence this region.

Immediately downstream of the obstruction, region 2 exhibits recirculation for both flow patterns. For thicker liquid films, the recirculation is intense and remains concentrated near the obstruction. In contrast, for thinner films, the liquid film primarily travels downstream with minimal disruption.

The most striking distinction appears in region 3. With thinner liquid films, we theorize that the inertia of the liquid film and shear from the vapor core drives the liquid film downstream,

forming a calm region 3. With thicker liquid films, however, recirculating liquid appears to stall due to insufficient vapor shear. This yields a severely liquid deficient region that forms into a new dryout region (region 3) close to the obstruction with little heat. Unlike dryout in the far downstream regions of the flow, this upstream dryout area is characterized by stationary liquid droplets on the wall, likely originating from droplet deposition influenced by the obstruction.

Thicker films also change the characteristics of region 4, where rewetting is observed downstream of region 3. This rewetting in the wake of the obstruction is not observed with thinner film flows. We theorize that the increased turbulence in the thicker films, particularly in the larger disturbance waves, enhances lateral movement that can rewet the wake. Additionally, the higher relative importance of surface tension forces over inertial forces, combined with increased droplet deposition, may contribute to the formation of this rewetted region.

Finally, regions 5 and 6 are similar in the thin and thick film cases. As the relatively thin and calm region 4 is exposed to the heated wall, it gradually vaporizes, leading to the formation of a far downstream dryout region (region 6). Region 5 represents the periphery free stream region which is not significantly impacted by the presence of the obstruction. For both thick and thin films, the disturbance waves are split upon contact with the obstruction and are largely contained to region 5.

The recombination of the liquid film downstream of a dryout patch is a striking phenomenon. There is likely some exchange of liquid mass between the wake region and the periphery of the flow for both the dual and single dryout flows. Since dual dryout occurs in thick, low-mass-flux flows, the recombination could result from increased turbulence in the thicker disturbance waves. Furthermore, low vapor shear at low mass flux allows any turbulence in the liquid film greater freedom to move laterally. Additionally, we can consider how the relative

importance of destabilizing vapor core inertial forces compared to cohesive surface tension forces (representing the Weber number) varies under different flow conditions. Calculating the Weber number using to the method of Cioncolini and Thome [89], we find that low mass flux and vapor quality flows have a small Weber number, corresponding to larger droplets and a more cohesive liquid film. The deposition of these large droplets in the wake of the obstruction provides an influx of liquid mass into a severely deficient region. Turbulent lateral movement from the periphery of the flow may combine with these deposited droplets to bridge around the dry area without being destabilized by the vapor core.

## 2. Temperature Response

The wake temperature response provides a quantitative representation of the wake shape and dryout regions discussed in *Chapter 6 Section 1*. Fig. 31 presents the time trace of temperature measurements at a mass flux of 140 kg/m$^2$-s and inlet vapor quality of 0.55, visually confirmed to yield two separate dryout regions. At the initial increase in heat flux, the temperature reading in the recirculation region (TC$_{ext,1}$) and slightly downstream of the impending dryout region near the obstruction (TC$_{ext,3}$) remains lower than the other measurement points. As heat flux increases, all temperature measurements rise without a significant change in behavior until reaching 36.6 kW/m$^2$, at which point TC$_{ext,2}$ peaks just above the other temperature measurements. Beyond this point, TC$_{ext,2}$ responds with a greater temperature rise to an increase in heat flux compared to the other temperature measurements until the heat flux reaches 44.5 kW/m$^2$. At this heat flux, there is a sharp temperature rise at TC$_{ext,6}$, and a moderate temperature rise at TC$_{ext,5}$, both to a value exceeding the other measurement points. As heat flux continues to increase, TC$_{ext,2}$, TC$_{ext,5}$, and TC$_{ext,6}$ further separate from the other measurements with TC$_{ext,6}$ experiencing the most severe temperature rise.
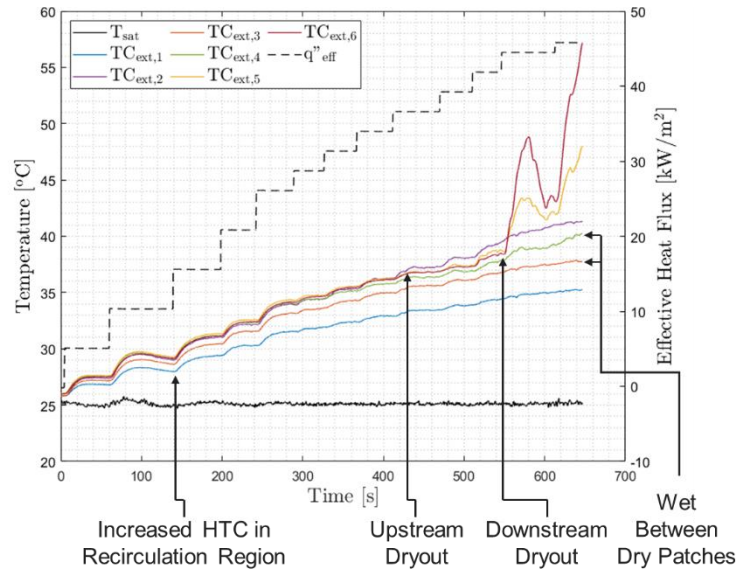
**Fig. 31**: Temperature time trace for flow conditions yielding dual dryout (all temperature data available in *Appendix E)*

The muted temperature response at $TC_{ext,1}$ compared to the other thermocouples can be attributed to the turbulent recirculation patterns immediately downstream of the obstruction, which likely enhance the heat transfer coefficient. Additionally, high-speed videos show increased bubble generation at the interface between the recirculation region and the free stream flow. The visible growth of vapor bubbles in this region likely complements flow turbulence to increase heat transfer coefficient. The temperature response of $TC_{ext,3}$ is less intuitive. At high heat flux, $TC_{ext,3}$ is positioned near the dry area surrounding $TC_{ext,2}$, potentially benefitting from a local quenching effect. However, this alone does not fully explain the observed behavior as an increased heat transfer coefficient is evident before dryout occurs. High-speed imaging does indicate a substantial increase in droplet impingement at $TC_{ext,3}$ compared to other flow regions. However, $TC_{ext,3}$ is located at the very edge of region 4 of the flow, where the liquid film is the thinnest in the wake. A thinner film corresponds to a higher heat transfer coefficient which could account for the observed temperature response.

The temperature profile of $TC_{ext,2}$ shows that dryout first occurs at this upstream wake location at 36.6 kW/m$^2$. However, the associated temperature rise is minimal, likely due to the multitude of liquid droplets in the dryout that created localized regions of enhanced heat transfer. Further, the small size of the dry area allows heat to conduct into adjacent wetted areas, mitigating temperature increase. In contrast, more severe dryout occurs at the far downstream location $TC_{ext,6}$ at 44.5 kW/m$^2$. As videos confirm, the size of the dry area oscillates greatly at this location, causing the spike and subsequent drop in temperature. Between $TC_{ext,2}$ and $TC_{ext,5}$, the thermocouples measure a cooler temperature which must mean the two dry areas are separated by a rewetted wall.

This temperature profile generates a question: How should CHF be defined for these flows? If CHF is defined as the heat flux at which sustained dryout first occurs, it corresponds to 36.6 kW/m$^2$. However, if CHF is defined by a significant temperature rise associated with increased heat flux, it would be 44.5 kW/m$^2$. Both definitions have merit, but choosing one over the other could impose artificial limits on the maximum operating conditions of a system.

## 3. Behavior Inflection

### 3.1 Transitional Temperature Response

The next step after identifying two distinct dryout phenomena was to determine if a set of flow conditions would create the dryout pattern shown in Fig. 30 (a) or (b). *Chapter 6* extensively investigated flows with inlet vapor quality of 0.63 or a mass flux of 130 kg/m$^2$-s. To understand the transition between dry regions, we probed the operating conditions around this point with the following three tests:

1. <u>Variable Mass Flux:</u> The inlet quality was held constant at $x_{in}=0.63$, while the mass flux varied from 95 – 170 kg/m$^2$-s (Fig. 6).

2. <u>Variable Inlet Quality:</u> The mass flux was fixed at 130 kg/m$^2$-s, and the inlet quality varied from 0.45 – 0.95 (Fig. 7).

3. <u>Variable Inlet Quality:</u> The mass flux was fixed at 140 kg/m$^2$-s, and the inlet quality varied from 0.45 – 0.7 (appendix).

The temperature data for all experiments are provided in the appendix. In Fig. 32 and Fig. 33, the temperature at the measured location most impacted by the upstream dryout (TC$_2$) is compared to the temperature at the measured location most impacted by the downstream dryout (TC$_6$). A positive temperature difference indicates the upstream location is warmer than the far downstream location.

Fig. 32 reveals two distinct temperature behaviors as mass flux increases. Fig. 32 (a) shows that, at low mass flux (G < 120 kg/m$^2$-s), temperature remains independent of mass flux at heat fluxes below 15 kW/m$^2$. Beyond this threshold, a sharp temperature spike occurs, indicating dryout at the upstream location. Following this spike, the temperature difference shifts sharply negative, suggesting intense dryout at the downstream location. This temperature response aligns with the two separate dryout regions observed in the temperature time trace shown in Fig. 31 and described in *Chapter 6 Section 2*. At high mass flux (G > 120 kg/m$^2$-s, Fig. 32 (b)), the temperature difference is no longer independent of mass flux at low heat flux. Instead, the response is characteristic of a thinning film. We theorize that the liquid film at TC 2 is stalled by the recirculation patterns at low mass flux, but the unidirectional movement of the liquid film at high mass flux creates a continuous film, emphasizing the effect of thinning. In the high mass flux cases, the film thins significantly as it flows downstream, yielding a higher heat transfer coefficient at the downstream location compared to the upstream location and the positive slope seen in Fig. 32 (b). Importantly, there is no visual evidence that the positive temperature slope seen in Fig. 32 (b) is the result of dryout

upstream. At high heat flux, a severe temperature rise occurs far downstream, indicating large area dryout. The transition between the two mass flux regimes falls between $G = 120$ kg/m$^2$-s and $G = 130$ kg/m$^2$-s, where the temperature profiles exhibit similar behaviors. This range marks a clear inflection point between low mass flux and high mass flux characteristics.
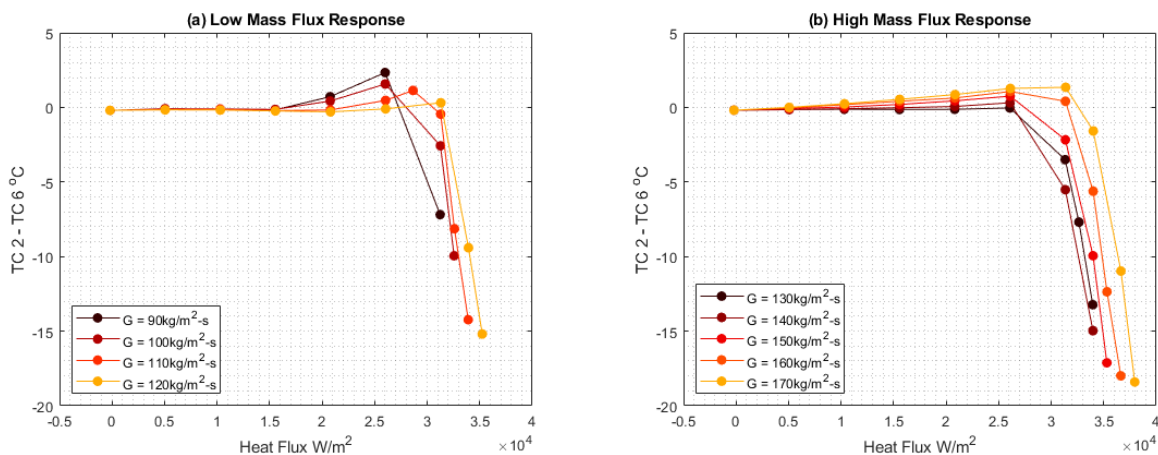


**Fig. 32:** Temperature difference between the upstream (TC$_2$) and downstream (TC$_6$) dryout locations at a constant inlet vapor quality of $x_{in}$=0.63 and (a) low mass flux or (b) high mass flux

Holding mass flux constant rather than inlet quality, the low inlet quality experiments ($x_{in}$ < 0.6, Fig. 33 (a)) exhibit a temperature rise at the upstream location before the downstream location. Under these flow conditions, the upstream area dries at a lower heat flux than the downstream area. Referring to Fig. 32 (b), at 130 kg/m$^2$-s, the temperature difference does not appear to be a function of heat flux other than in instances of dryout. This trend extends to the constant inlet vapor quality experiments, producing the flat line behavior seen in Fig. 33 (b) prior to downstream dryout. At high quality conditions ($x_{in}$ > 0.6), the dominant factor influencing the temperature difference between the upstream and downstream locations is downstream dryout. The data indicates an inflection point between $x_{in}$=0.60 and $x_{in}$=0.66. When the experiment was repeated at 140 kg/m$^2$-s, the behavior remained consistent, though the inflection point shifted to a slightly lower quality of $x_{in}$=0.50 – 0.55.
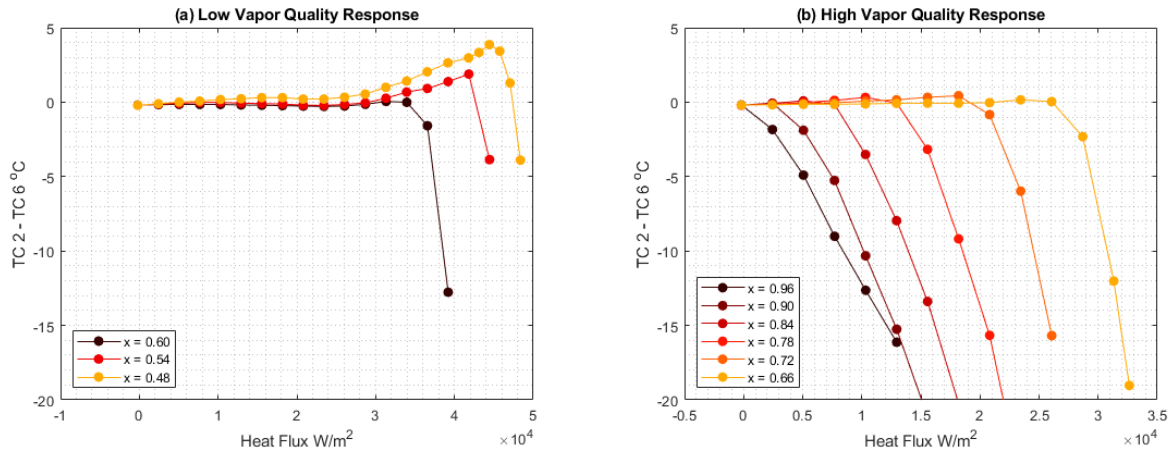
**Fig. 33:** Temperature difference between the upstream (TC 2) and downstream (TC 6) dryout locations at a constant mass flux of G=130 kg/m²-s and (a) low inlet vapor quality or (b) high inlet vapor quality

### 3.2 Predicting the Transition

One conclusion from these experiments is that upstream dryout occurs before downstream dryout at flow conditions more favorable for nucleate boiling. That is, at conditions where the liquid film is thick and slow moving (low vapor quality and low mass flux). While nucleate boiling itself does not significantly influence liquid film movement in these experiments, the flow conditions that promote nucleate boiling also give rise to this new dryout phenomenon.

High-speed video analysis confirms that the recirculation region formed under conditions of thick films or low mass fluxes exhibits significant circular movement and counterflow momentum. Conversely, at high mass flux or with thin films, counterflow within the recirculation region disappears. In these cases, the liquid film is immediately carried downstream by its momentum and the vapor interfacial shear, facilitating the formation of region 3 as depicted in Fig. 30 (a). The supplied video, "Whirlpool", illustrates the recirculation pattern for a thick film at G=140 kg/m²-s, $x_{in}$=0.45, and q=0 W/m². In this short clip, the vortex created by the obstruction has sufficient circular momentum to momentarily break the liquid film even in the absence of heat flux. This whirlpool effect, lasting approximately 0.017 seconds, is analogous to the swirling

motion of water draining from a pool. In short, the recirculation pattern associated with thick films or slow flows yields substantial counterflow momentum, leading to a severely deficient liquid film immediately downstream of the obstruction.

The recirculation pattern may change as a function of the liquid Reynolds number, like single phase flow past a cylinder. Typical recirculation patterns in single phase flow are shown in Fig. 34, where the wake of a cylinder transitions from strong localized countercurrent vortices to a more turbulent bulk flow as the Reynolds number increases. We see a similar effect in our test section, where a stationary vortex is seen immediately downstream of the cylinder in the liquid film at low vapor qualities and mass fluxes.
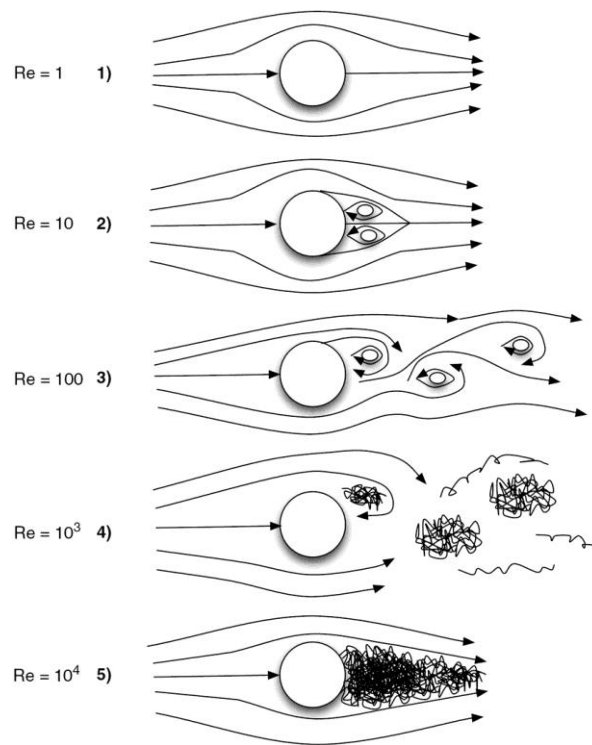


**Fig. 34:** Approximation of single phase flow around a cylinder as a function of Reynolds number [90]

Although likely important, the liquid Reynolds number does not fully dictate the flow pattern in thin liquid films. Interfacial shear also appears to play an important role in the downstream movement of vortex structures in the liquid film. The vapor core of the flow is highly

turbulent at all conditions tested ($Re_v>16000$) and thus does not generate large coherent vortices when flowing around a cylinder. As a result, the turbulent vapor core always pulls the liquid film downstream and can prevent upstream wake dryout. As the vapor shear decreases (at low quality and mass flux), the suppression of liquid film recirculation weakens, allowing for free vortex formation and potentially leading to upstream dryout.

The effect of interfacial shear on the vortices generated in annular flow has, to the author's knowledge, not been explored in the literature. However, many publications have simulated the effect of the air-water interface on vortex shedding from an interface piercing vertical circular cylinder. It has been observed that near the interface, organized vortex shedding is absent while simultaneously occurring deeper in the flow [91]. Additionally, the liquid velocity in the wake of the cylinder is lower at the air-water interface than what is seen deeper in the flow [92]. This velocity phenomenon can be seen in Fig. 35 below. While this simulation does not capture vortices being dragged downstream by the interfacial shear, it does demonstrate that liquid in the wake of a cylinder near the interface tends to follow velocity of the gas phase.
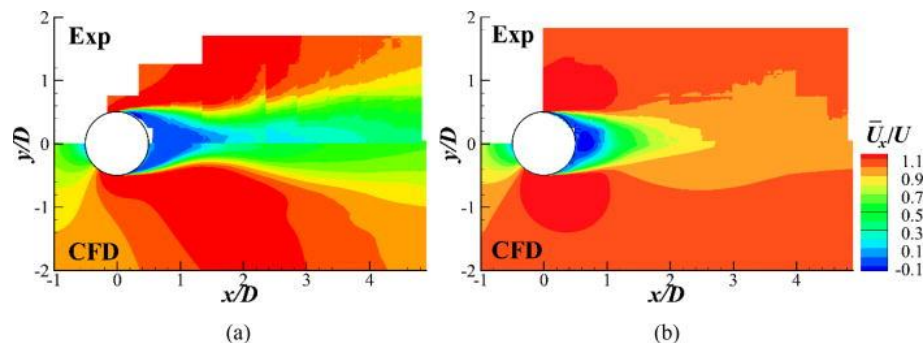


**Fig. 35:** Time-averaged streamwise velocity at (a) $z/D=-0.75$, and (b) $z/D=-3.5$, where $z$ is the vertical surface with 0 at the air-water interface, and $D$ is the cylinder diameter [92]

These observations highlight the critical role of the liquid film and vapor core inertia in predicting hydrodynamic behavior. The inertia of the liquid film can be characterized using the liquid film Reynolds number. However, without direct film thickness measurements, the precise

calculation of this parameter remains an open area for future investigation. Instead, an estimated liquid Reynolds number can be determined using,

$$Re_l = \frac{(1 - x_{local})(1 - e)GD_{obs}}{\mu_l} \tag{20}$$

where the entrainment ratio, e, is predicted using the Cioncolini and Thome correlation [89]. To quantify the relative significance of interfacial shear, we introduce the shear-weight ratio (SWR):

$$SWR = \frac{\tau_{int}}{\rho_l \delta_{avg} g} \tag{21}$$

Equation (21) is the ratio of the interfacial shear stress to the weight of the liquid film per unit area. The method of calculating the shear stress, $\tau_{int}$, follows that outlined by Morse et al. [4], while the average film thickness, $\delta_{avg}$, is estimated as a geometric function of the void fraction as predicted using the method from Cioncolini and Thome [62].

The SWR represents the ratio of acceleration of the liquid film due to the shear force to the acceleration due to gravity. Equation (21) is simply a rearranged *F=m\*a* equation where the mass is $\rho_l \delta_{avg} dA$, the force is $\tau_{int} dA$, and the acceleration is SWR. If both the force and mass sides of the equation are multiplied by $g^{-1}$, the result is Equation (21). There are, of course, other forces acting on the liquid film namely a pressure force and a wall shear force. Analysis shows pressure forces are over an order of magnitude less significant than the weight of the liquid film and can safely be neglected. The assumption that the wall shear stress does not significantly vary between test conditions must then also be made. This assumption could be valid if the velocity of the liquid film does not vary significantly between tests, but no velocity data was gathered. If the statements about pressure and wall shear are assumed to be true, then the SWR alone should vary between test conditions.

By multiplying the liquid Reynolds number with the SWR, we can define a new dimensionless number, termed the Obstructed Annular number (*OA*):

$$OA = SWR^{1.5} * Re_l^{0.5} \tag{22}$$

The exponentials in equation (22) are arbitrarily chosen to emphasize the relative importance of interfacial shear versus liquid inertia. In annular flow, liquid motion is primarily governed by shear from the vapor core rather than its inertia. As a result, the shear term is weighted more heavily than the Reynolds number in this formulation.

The *OA* number can be applied to predict the transition in dryout behavior. Fig. 36 presents the maximum temperature ratio at each mass flux-inlet quality pair obtained from the data described in *Chapter 6 Section 3.1* and shown in *Appendix F*, plotted as a function of the dimensionless ratio from equation (22). The results reveal a clear and consistent minimum in the temperature ratio corresponding to the manually identified transition between dual area and single area dryout. As discussed in *Chapter 6 Section 3.1*, dual area dryout occurs with slow and thick films, which corresponds to low interfacial shear and Reynolds number. This signifies that the values to the left of the minimum point exhibit characteristics that yield dual dryout while values to the right exhibit single dryout. Based on this limited data set, a critical *OA* value of approximately 65 is proposed as the transition between the two dryout regimes. The temperature ratio data as a function of the *OA* number for all tests can be seen in the *Appendix F*. This modeling exercise is not necessarily meant to predict the exact transition point with high confidence, but rather to illustrate the predictability of the dryout phenomenon observed and provide a basis for possible future work.
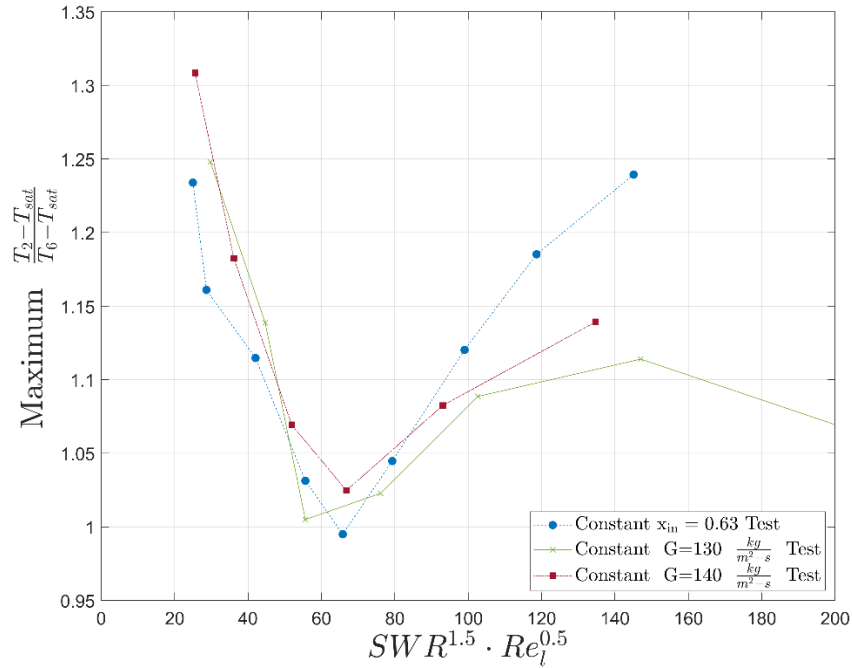
**Fig. 36:** Transition between dryout regimes as defined using a new combination of dimensionless numbers

The effect of the Reynolds number and SWR on the dimensionless temperature ratio are separately in Fig. 37 (a) and (b). As shown in Fig. 37 (a), the local minimum of the temperature ratio varies significantly as a function of liquid Reynolds number. In contrast, Fig. 37 (b) indicates that the local minimum changes only slightly with the SWR. It is important to note that the data used for these graphs fall within a relatively narrow range. Expanding the dataset may reveal a stronger dependence of the temperature ratio on the SWR or suggest that the SWR alone is sufficient in predicting the transition point. Furthermore, without considering the Reynolds number, the obstruction diameter would not be accounted for in the flow prediction.
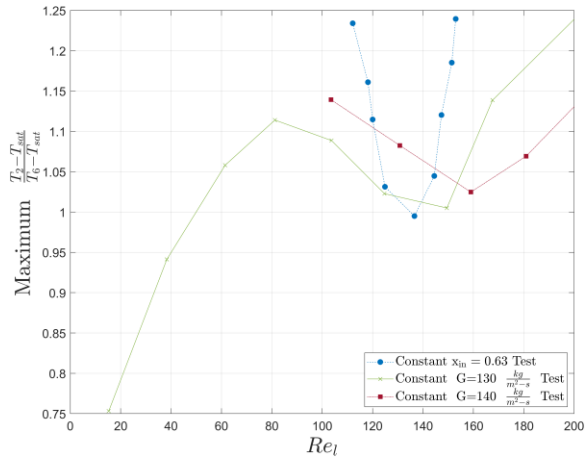
(a)
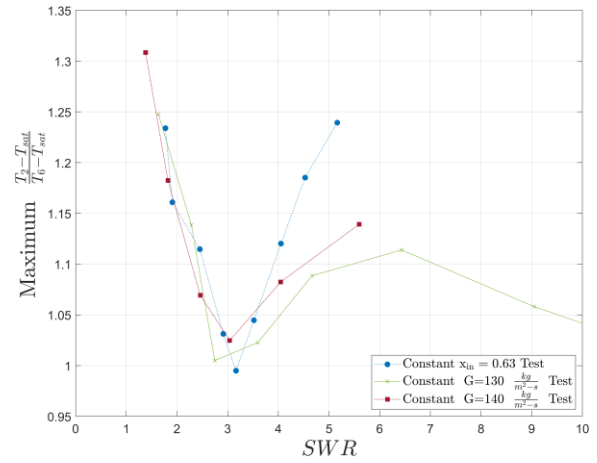
(b)

**Fig. 37:** Transition between dryout regimes as defined using a (a) the Reynolds number alone or (b) using the SWR alone

# CHAPTER 7: CONCLUSION

## 1. Thin Film Nucleate Boiling

Nucleate boiling in thin film annular flow is a highly complex phenomenon influenced by a set of competing factors such as film thickness, vapor quality, surface tension, wall superheat, and mass flux. While boiling occurs within a thin thermal layer where the liquid temperature exceeds the saturation temperature, forced convective evaporation may eliminate superheating and suppress boiling. Although disturbance waves are known to trigger nucleation, the mechanisms behind this effect remain unconfirmed, with hypotheses ranging from localized heat transfer enhancement to bubble entrainment and mixing effects. Some research has shown there is a correlation between the passage of a disturbance wave and a lower heat transfer coefficient. Modeling efforts have included both empirical correlations and heat flux partitioning methods, the latter offering greater potential for capturing the contributions of individual heat transfer mechanisms. This knowledge of nucleate boiling was used to inform design changes in the test facility to expand testable conditions into the annular flow boiling regime where enhanced nucleate boiling under disturbance wave was again observed.

## 2. Obstructed Annular Flow

When a small cylindrical obstruction is placed in annular flow to disrupt the liquid film, a parabolic-shaped dryout region forms with sufficient heat. This dry region first forms in the obstruction wake and is initially quite thin, confined to the centerline of the wake. As the heat flux grows, the dry region grows as well, still contained within the wake. The degradation in heat transfer coefficient measure in the dry wake has been found to be proportional to the dry wake size. This wake dryout occurs for two reasons. First, the liquid film in the wake is thinner than the free stream flow, decreasing the liquid mass available to vaporize. Second, disturbance waves are

directed out of the wake region by the obstruction and do not recombine into the wake. This thin, waveless flow is slowly dragged downstream by the vapor core, vaporizing as it travels until eventual dryout.

If the liquid film is sufficiently thick and slow moving upon contact with the obstruction, it may dry close to the obstruction as well as far downstream. These two dry regions are separated by a wet flow likely fed by mass exchange with the free stream flow. The upstream dry region is small compared to the downstream dry region and filled with droplets, leading to a relatively small decrease in heat transfer coefficient upon dryout. We theorize that this upstream dryout region forms because the liquid film stalls in the immediate recirculation region downstream of the obstruction. Without sufficient vapor shear or incoming momentum, the liquid film in the recirculation cannot progress downstream, and thus an upstream dry region forms. The transition between the dual and single dryout systems can be modeled with some success through a combination of the incoming liquid Reynolds number and the ratio of the acceleration due to the vapor interfacial shear and the gravitational acceleration of the liquid film.

## 3. Future Work

The transition from nucleate boiling dominant to forced convective evaporation dominated annular flow represents a poorly defined regime where multiple competing mechanisms influence the total heat transfer coefficient. This ambiguity underscores the need for detailed experimental investigations to measure the local heat transfer coefficient under well-controlled conditions. The heat flux partitioning approach offers a promising framework for addressing this gap, as it enables the isolation and quantification of individual heat transfer mechanisms contributing to the overall process. Another unresolved question in thin film nucleate boiling involves the root cause of disturbance wave induced nucleation cavity activation. It has been well demonstrated that

disturbance waves may trigger nucleation, but the underlying mechanisms remain unknown. Quantifying the effect of disturbance waves is critical for creating accurate heat transfer coefficient models and precise flow regime predictions.

Obstructed annular flow is not a popularly studied two-phase flow research topic leaving many gaps in our knowledge of two-dimensional thin liquid film flows. Specifically, the exchange of mass between the free stream regions on the periphery of the flow and the wake region is not well understood. It is clear from the rewetting of the wake between the upstream and downstream dryout regions shown in *Chapter 6* that there is some exchange of mass, but the downstream distance at which this occurs, and the extent of the exchange needs be measured to better understand wake dryout. If an accurate map of the mass flow rate field around a cylindrical obstruction was created, it could be coupled with film thickness-based models to predict dryout type critical heat flux using well supported physics. However, there are many challenges associated with unobtrusively measuring mass flow rate in any part of the flow. We propose that particle image velocimetry could be paired with the total internal reflectance liquid film thickness measurement technique to decompose the mass flow rate measurement into its component parts.

# REFERENCES

[1]   G. F. Hewitt and N. S. Hall-Taylor, *Annular Two-Phase Flow*, 1st ed. Oxford, UK: Pergamon Press Ltd, 1970.

[2]   R. W. Morse, T. A. Moreira, J. Chan, K. M. Dressler, G. Ribatski, E. T. Hurlburt, L. L. McCarroll, G. F. Nellis, A. Berson, "Critical heat flux and the dryout of liquid film in vertical two-phase annular flow," *Int. J. Heat Mass Transf.*, vol. 177, p. 121487, Oct. 2021, doi: 10.1016/j.ijheatmasstransfer.2021.121487.

[3]   S. M. Ghiaasiaan, *Two-Phase Flow, and Condensation In Convectional and Miniature Systems*, 2nd ed. Cambridge, UK: Cambridge University Press, 2017.

[4]   R. W. Morse *et al.*, "A new paradigm for the role of disturbance waves on film dryout and wall heat transfer in annular two-phase flow," *Int. J. Heat Mass Transf.*, vol. 219, p. 124812, Feb. 2024, doi: 10.1016/j.ijheatmasstransfer.2023.124812.

[5]   J. S. Kaizer *et al.*, "Credibility Assessment Framework for Critical Boiling Transition Models: A generic safety case to determine the credibility of critical heat flux and critical power models." U.S. Nuclear Regulatory Commission, Mar. 2019.

[6]   S.-M. Kim and I. Mudawar, "Universal approach to predicting saturated flow boiling heat transfer in mini/micro-channels – Part I. Dryout incipience quality," *Int. J. Heat Mass Transf.*, vol. 64, pp. 1226–1238, Sep. 2013, doi: 10.1016/j.ijheatmasstransfer.2013.04.016.

[7]   S. Gu, L. Tao, C. Jin, Y. Ju, and X. Zhao, "Study of flow pattern transition criterion and heat transfer characteristics in vertical rectangular narrow channel for steam heating," *Int. J. Heat Mass Transf.*, vol. 220, p. 124877, Mar. 2024, doi: 10.1016/j.ijheatmasstransfer.2023.124877.

[8]   S. H. Kim, I. C. Chu, M. H. Choi, and D. J. Euh, "Mechanism study of departure of nucleate boiling on forced convective channel flow boiling," *Int. J. Heat Mass Transf.*, vol. 126, pp. 1049–1058, Nov. 2018, doi: 10.1016/j.ijheatmasstransfer.2018.05.105.

[9]   J.-M. Le Corre, "Phenomenological model of disturbance waves in annular two-phase flow," *Int. J. Multiph. Flow*, vol. 151, p. 104057, Jun. 2022, doi: 10.1016/j.ijmultiphaseflow.2022.104057.

[10]  S. H. Baek, H.-S. Shim, J. G. Kim, and D. H. Hur, "Effects of heat flux on fuel crud deposition and sub-cooled nucleate boiling in simulated PWR primary water at 13 MPa," *Ann. Nucl. Energy*, vol. 133, pp. 178–185, Nov. 2019, doi: 10.1016/j.anucene.2019.05.022.

[11]  B. Wu, M. Firouzi, T. Mitchell, T. E. Rufford, C. Leonardi, and B. Towler, "A critical review of flow maps for gas-liquid flows in vertical pipes and annuli," *Chem. Eng. J.*, vol. 326, pp. 350–377, Oct. 2017, doi: 10.1016/j.cej.2017.05.135.

[12]  J. Kim, "Review of nucleate pool boiling bubble heat transfer mechanisms," *Int. J. Multiph. Flow*, vol. 35, no. 12, pp. 1067–1076, 2009, doi: 10.1016/j.ijmultiphaseflow.2009.07.008.

[13]  V. K. Dhir, "Nucleate and transition boiling heat transfer under pool and external flow conditions," *Int. J. Heat Fluid Flow*, vol. 12, no. 4, pp. 290–314, Dec. 1991, doi: 10.1016/0142-727X(91)90018-Q.

[14] G. Yang, W. Zhang, M. Binama, J. Sun, and W. Cai, "Review on bubble dynamic of subcooled flow boiling-part a: Research methodologies," *Int. J. Therm. Sci.*, vol. 184, p. 108019, Feb. 2023, doi: 10.1016/j.ijthermalsci.2022.108019.

[15] G. Yang, W. Zhang, M. Binama, Q. Li, and W. Cai, "Review on bubble dynamic of subcooled flow boiling-part b: Behavior and models," *Int. J. Therm. Sci.*, vol. 184, p. 108026, Feb. 2023, doi: 10.1016/j.ijthermalsci.2022.108026.

[16] C. Berna, A. Escrivá, J. L. Muñoz-Cobo, and L. E. Herranz, "Review of droplet entrainment in annular flow: Interfacial waves and onset of entrainment," *Prog. Nucl. Energy*, vol. 74, pp. 14–43, Jul. 2014, doi: 10.1016/j.pnucene.2014.01.018.

[17] C. Berna, A. Escrivá, J. L. Muñoz-Cobo, and L. E. Herranz, "Review of droplet entrainment in annular flow: Characterization of the entrained droplets," *Prog. Nucl. Energy*, vol. 79, pp. 64–86, Mar. 2015, doi: 10.1016/j.pnucene.2014.11.011.

[18] S. K. Singh and D. Sharma, "Review of pool and flow boiling heat transfer enhancement through surface modification," *Int. J. Heat Mass Transf.*, vol. 181, p. 122020, Dec. 2021, doi: 10.1016/j.ijheatmasstransfer.2021.122020.

[19] S. Husain and S. A. Khan, "A review on heat transfer enhancement techniques during natural convection in vertical annular geometry," *Clean. Eng. Technol.*, vol. 5, p. 100333, Dec. 2021, doi: 10.1016/j.clet.2021.100333.

[20] N. Basu, G. Warrier, and V. K. Dhir, "Wall Heat Flux Partitioning During Subcooled Flow Boiling: Part 1—Model Development," *J. Heat Transf.-Trans. Asme - J HEAT Transf.*, vol. 127, Feb. 2005, doi: 10.1115/1.1842784.

[21] N. Basu, G. R. Warrier, and V. K. Dhir, "Wall Heat Flux Partitioning During Subcooled Flow Boiling: Part II—Model Validation," *J. Heat Transf.*, vol. 127, no. 2, pp. 141–148, Mar. 2005, doi: 10.1115/1.1842785.

[22] J. Chen, "A Correlation for Boiling Heat Transfer to Saturated Fluids in Convective Flow," *Ind. Eng. Chem. Process Des. Dev.*, vol. 5, no. 3, pp. 322–329, 1966, doi: 10.1021/i260019a023.

[23] S. G. Kandlikar, "A General Correlation for Saturated Two-Phase Flow Boiling Heat Transfer Inside Horizontal and Vertical Tubes," *J. Heat Transf.*, vol. 112, no. 1, pp. 219–228, Feb. 1990, doi: 10.1115/1.2910348.

[24] D. C. Groeneveld *et al.*, "The 2006 CHF look-up table," *Nucl. Eng. Des.*, vol. 237, no. 15, pp. 1909–1922, Sep. 2007, doi: 10.1016/j.nucengdes.2007.02.014.

[25] M. Mohammed Shah, "Improved general correlation for critical heat flux during upflow in uniformly heated vertical tubes," *Int. J. Heat Fluid Flow*, vol. 8, no. 4, pp. 326–335, Dec. 1987, doi: 10.1016/0142-727X(87)90069-5.

[26] M. Caira, G. Caruso, and A. Naviglio, "A correlation to predict chf in subcooled flow boiling," *Int. Commun. Heat Mass Transf.*, vol. 22, no. 1, pp. 35–45, Jan. 1995, doi: 10.1016/0735-1933(94)00050-U.

[27] K. Washburn and G. Lauchle, "Effects of Inflow Conditions on Discrete Frequency Noise Generated by Small Axial Fan Flows," Pennsylvania State University Applied Research

Laboratory, State College, Pennsylvania, Technical Report 85–001, Sep. 1985. [Online]. Available: https://apps.dtic.mil/sti/pdfs/ADA160579.pdf

[28] F. L. Ponta, "Vortex decay in the Kármán eddy street," *Phys. Fluids*, vol. 22, no. 9, p. 093601, Sep. 2010, doi: 10.1063/1.3481383.

[29] S. K. Bose and S. Dey, "Far-wake flows downstream of cylinders: A novel generalized similarity method," *Eur. J. Mech. - BFluids*, vol. 67, pp. 65–69, Jan. 2018, doi: 10.1016/j.euromechflu.2017.08.008.

[30] H. Zahlan, "Flow Obstacle Effect on Film Boiling Heat Transfer with Uniform and Non-Uniform Axial Heat Flux," University of Ottawa, Ottawa, Canada, 2008. [Online]. Available: https://ruor.uottawa.ca/items/e6662755-537d-45d2-bfd2-84dd39c471a9

[31] T. Ami, H. Umekawa, and M. Ozawa, "Influence of a Flow Obstacle on Boiling Two-Phase Flow," presented at the ASME 2011 Power Conference collocated with JSME ICOPE 2011, American Society of Mechanical Engineers Digital Collection, Feb. 2012, pp. 727–734. doi: 10.1115/POWER2011-55391.

[32] T. Okawa, N. Shimada, A. Kotani, and I. Kataoka, "An Experimental Study on the Mass Transfer Rate of Droplets in Annular Two-Phase Flow," *JSME Int. J. Ser. B*, vol. 49, no. 2, pp. 271–278, 2006, doi: 10.1299/jsmeb.49.271.

[33] S. Mori and T. Fukano, "Influence of a flow obstacle on the occurrence of burnout in boiling two-phase upward flow within a vertical annular channel," *Nucl. Eng. Des.*, vol. 225, no. 1, pp. 49–63, Oct. 2003, doi: 10.1016/S0029-5493(03)00136-5.

[34] T. Fukano, S. Mori, and T. Nakagawa, "Fluctuation characteristics of heating surface temperature near an obstacle in transient boiling two-phase flow in a vertical annular channel," *Nucl. Eng. Des.*, vol. 219, no. 1, pp. 47–60, Jan. 2003, doi: 10.1016/S0029-5493(02)00214-5.

[35] Y. Yamamoto, A. Hoshide, T. Mitsutake, and S. Morooka, "Analytical study on effects of BWR fuel spacer on droplet deposition," *Nucl. Eng. Des.*, vol. 175, no. 1, pp. 119–129, Nov. 1997, doi: 10.1016/S0029-5493(97)00168-4.

[36] I. L. Pioro, D. C. Groeneveld, S. S. Doerffer, Y. Guo, S. C. Cheng, and A. Vasić, "Effects of flow obstacles on the critical heat flux in a vertical tube cooled with upward flow of R-134a," *Int. J. Heat Mass Transf.*, vol. 45, no. 22, pp. 4417–4433, Oct. 2002, doi: 10.1016/S0017-9310(02)00150-3.

[37] T. Podgorski, J.-M. Flesselles, and L. Limat, "Dry arches within flowing films," *Phys. Fluids*, vol. 11, no. 4, pp. 845–852, Apr. 1999, doi: 10.1063/1.869956.

[38] E. Rio and L. Limat, "Wetting hysteresis of a dry patch left inside a flowing film," *Phys. Fluids*, vol. 18, no. 3, p. 032102, Mar. 2006, doi: 10.1063/1.2173183.

[39] M. Sellier, "Modelling the wetting of a solid occlusion by a liquid film," *Int. J. Multiph. Flow*, vol. 71, pp. 66–73, May 2015, doi: 10.1016/j.ijmultiphaseflow.2014.12.007.

[40] S. Veremieiev, H. M. Thompson, Y. C. Lee, and P. H. Gaskell, "Inertial two- and three-dimensional thin film flow over topography," *Chem. Eng. Process. Process Intensif.*, vol. 50, no. 5, pp. 537–542, May 2011, doi: 10.1016/j.cep.2010.08.008.

[41] S. Veremieiev, H. M. Thompson, and P. H. Gaskell, "Free-surface film flow over topography: Full three-dimensional finite element solutions," *Comput. Fluids*, vol. 122, pp. 66–82, Nov. 2015, doi: 10.1016/j.compfluid.2015.08.016.

[42] M. Sellier, Y. C. Lee, H. M. Thompson, and P. H. Gaskell, "Thin film flow on surfaces containing arbitrary occlusions," *Comput. Fluids*, vol. 38, no. 1, pp. 171–182, Jan. 2009, doi: 10.1016/j.compfluid.2008.01.008.

[43] S. J. Baxter, H. Power, K. A. Cliffe, and S. Hibberd, "Three-dimensional thin film flow over and around an obstacle on an inclined plane," *Phys. Fluids*, vol. 21, no. 3, p. 032102, Mar. 2009, doi: 10.1063/1.3082218.

[44] B. Fehring, "Transient Wall Temperature and Film Thickness of Vertical Annular Two-Phase Pulsatile Flow," M.S., University of Wisconsin-Madison, Madison, WI, 2018. [Online]. Available: https://search.library.wisc.edu/catalog/9912807862902121

[45] T. A. Moreira, R. W. Morse, K. M. Dressler, G. Ribatski, and A. Berson, "Liquid-film thickness and disturbance-wave characterization in a vertical, upward, two-phase annular flow of saturated R245fa inside a rectangular channel," *Int. J. Multiph. Flow*, vol. 132, p. 103412, Nov. 2020, doi: 10.1016/j.ijmultiphaseflow.2020.103412.

[46] J. Chan *et al.*, "Liquid film flow rate from measurements of disturbance wave characteristics for applications in thin film flow," *Exp. Fluids*, vol. 65, no. 6, p. 93, Jun. 2024, doi: 10.1007/s00348-024-03832-x.

[47] V. Carey, *Liquid-Vapor Phase-Change Phenomena*, 2nd ed. New York, NY: Taylor & Francis Group, LLC, 2008.

[48] C. Gerardi, J. Buongiorno, L. Hu, and T. McKrell, "Study of bubble growth in water pool boiling through synchronized, infrared thermometry and high-speed video," *Int. J. Heat Mass Transf.*, vol. 53, no. 19, pp. 4185–4192, Sep. 2010, doi: 10.1016/j.ijheatmasstransfer.2010.05.041.

[49] N. H. Hoang, C.-H. Song, I.-C. Chu, and D.-J. Euh, "A bubble dynamics-based model for wall heat flux partitioning during nucleate flow boiling," *Int. J. Heat Mass Transf.*, vol. 112, pp. 454–464, Sep. 2017, doi: 10.1016/j.ijheatmasstransfer.2017.04.128.

[50] S. Jayanti and G. F. Hewitt, "Hydrodynamics and heat transfer in wavy annular gas-liquid flow: a computational fluid dynamics study," *Int. J. Heat Mass Transf.*, vol. 40, no. 10, pp. 2445–2460, Jul. 1997, doi: 10.1016/S0017-9310(96)00288-8.

[51] H. Zhang, Y. Umehara, H. Yoshida, and S. Mori, "On the velocity and frequency of disturbance waves in vertical annular flow with different surface tension and gas–liquid density ratio," *Int. J. Heat Mass Transf.*, vol. 211, p. 124253, Sep. 2023, doi: 10.1016/j.ijheatmasstransfer.2023.124253.

[52] J. R. Barbosa, G. F. Hewitt, and S. M. Richardson, "High-speed visualisation of nucleate boiling in vertical annular flow," *Int. J. Heat Mass Transf.*, vol. 46, no. 26, pp. 5153–5160, Dec. 2003, doi: 10.1016/S0017-9310(03)00255-2.

[53] G.-Y. Su, F. Paolo D'Aleo, B. Phillips, E. Al-Safran, J. Buongiorno, and H.-M. Prasser, "Suppression of nucleate boiling in upward two-phase annular flow: A direct measurement

using modern diagnostics," *Int. J. Heat Mass Transf.*, vol. 159, p. 120143, Oct. 2020, doi: 10.1016/j.ijheatmasstransfer.2020.120143.

[54] Y. Y. Hsu, "On the Size Range of Active Nucleation Cavities on a Heating Surface," Journal of Heat Transfer, vol. 84, no. 3, pp. 0022-1481, Jan. 1962, doi: 10.1115/1.3684339.

[55] M. Cerza and V. Sernas, "Nucleate Boiling in Thermally Developing and Fully Developed Laminar Falling Water Films," *J. Heat Transf.*, vol. 110, no. 1, pp. 221–228, Feb. 1988, doi: 10.1115/1.3250455.

[56] N. Basu, G. R. Warrier, and V. K. Dhir, "Onset of Nucleate Boiling and Active Nucleation Site Density During Subcooled Flow Boiling," *J. Heat Transf.*, vol. 124, no. 4, pp. 717–728, Jul. 2002, doi: 10.1115/1.1471522.

[57] G.-Y. Su, "Thermohydraulics and Suppression of Nucleate Boiling in Upward Two-Phase Annular Flow: Probing Multiscale Physics by Innovative Diagnostics," Ph.D dissertation, Department of Nuclear Science and Engineering, Massachusetts Institute of Technology, Cambridge, 2018. [Online]. Available: https://dspace.mit.edu/handle/1721.1/7582

[58] R. Mesler and G. Mailen, "Nucleate boiling in thin liquid films," *AIChE J.*, vol. 23, no. 6, pp. 954–957, 1977, doi: 10.1002/aic.690230629.

[59] J. R. Barbosa, G. F. Hewitt, and S. M. Richardson, "Forced convective boiling of steam–water in a vertical annulus at high qualities," *Exp. Therm. Fluid Sci.*, vol. 26, no. 1, pp. 65–75, Apr. 2002, doi: 10.1016/S0894-1777(02)00108-5.

[60] T. Sato and H. Matsumura, "On the conditions of incipient subcooled boiling and forced convection, Bull. Japan. Soc. Mech. Engineers, vol. 7, pp. 392-398, 1964.".

[61] R. Charnay, R. Revellin, and J. Bonjour, "Flow boiling heat transfer in minichannels at high saturation temperatures: Part I – Experimental investigation and analysis of the heat transfer mechanisms," *Int. J. Heat Mass Transf.*, vol. 87, pp. 636–652, Aug. 2015, doi: 10.1016/j.ijheatmasstransfer.2015.03.081.

[62] A. Cioncolini and J. R. Thome, "Void fraction prediction in annular two-phase flow," *Int. J. Multiph. Flow*, vol. 43, pp. 72–84, Jul. 2012, doi: 10.1016/j.ijmultiphaseflow.2012.03.003.

[63] J. R. S. Thom, "Prediction of pressure drop during forced circulation boiling of water," *Int. J. Heat Mass Transf.*, vol. 7, no. 7, pp. 709–724, Jul. 1964, doi: 10.1016/0017-9310(64)90002-X.

[64] W. J. Marsh and I. Mudawar, "Predicting the onset of nucleate boiling in wavy free-falling turbulent liquid films," *Int. J. Heat Mass Transf.*, vol. 32, no. 2, pp. 361–378, Feb. 1989, doi: 10.1016/0017-9310(89)90183-X.

[65] W. Li, K. Zhou, J. Li, Z. Feng, and H. Zhu, "Effects of heat flux, mass flux and two-phase inlet quality on flow boiling in a vertical superhydrophilic microchannel," *Int. J. Heat Mass Transf.*, vol. 119, pp. 601–613, Apr. 2018, doi: 10.1016/j.ijheatmasstransfer.2017.11.145.

[66] N. V. Upot, A. Mahvi, K. Fazle Rabbi, J. Li, A. M. Jacobi, and N. Miljkovic, "Scalable and Resilient Etched Metallic Micro- and Nanostructured Surfaces for Enhanced Flow Boiling," *ACS Appl. Nano Mater.*, vol. 4, no. 7, pp. 6648–6658, Jul. 2021, doi: 10.1021/acsanm.1c00524.

[67] P. Ju and T. Hibiki, "Flow characteristics of gas-liquid adiabatic and boiling annular two-phase flows," *Int. J. Heat Mass Transf.*, vol. 210, p. 124161, Aug. 2023, doi: 10.1016/j.ijheatmasstransfer.2023.124161.

[68] T. N. Tran, M. W. Wambsganss, and D. M. France, "Boiling heat transfer with three fluids in small circular and rectangular channels," Argonne National Lab. (ANL), Argonne, IL (United States), ANL-95/9, Jan. 1995. doi: 10.2172/93485.

[69] B. Zajec, L. Cizelj, and B. Končar, "Effect of mass flow rate on bubble size distribution in boiling flow in temperature-controlled annular test section," *Exp. Therm. Fluid Sci.*, vol. 140, p. 110758, Jan. 2023, doi: 10.1016/j.expthermflusci.2022.110758.

[70] D. Wang, L. Zhao, X. Nie, Y. Lu, and S. Deng, "Experimental study on flow boiling characteristics of R-245fa in circular tube under non-uniform heat flux," *Int. J. Heat Mass Transf.*, vol. 143, p. 118570, Nov. 2019, doi: 10.1016/j.ijheatmasstransfer.2019.118570.

[71] E. Bediako, P. Dancova, A. F. A. Elbarghthi, and T. Vít, "Flow boiling heat transfer of R134a: Effect of heat flux and Dry-out characteristics," in *10th Int. Conf. on Fluid Flow, Heat and Mass Transfer,* Jun. 2023. doi: 10.11159/ffhmt23.161.

[72] Y. Liu, D. Jige, and N. Inoue, "Correlation for Flow Boiling Heat Transfer of Low-pressure Refrigerants Inside A Horizontal Smooth Tube," presented at the 18th Int. Refrigeration and Air Conditioning Conf., Purdue University, West Lafayette, May 2021. [Online]. Available: https://docs.lib.purdue.edu/iracc/2141/

[73] D. Jung, H. Lee, D. Bae, and S. Oho, "Nucleate boiling heat transfer coefficients of flammable refrigerants," *Int. J. Refrig.*, vol. 27, no. 4, pp. 409–414, Jun. 2004, doi: 10.1016/j.ijrefrig.2003.11.007.

[74] S.-M. Kim and I. Mudawar, "Universal approach to predicting saturated flow boiling heat transfer in mini/micro-channels – Part II. Two-phase heat transfer coefficient," *Int. J. Heat Mass Transf.*, vol. 64, pp. 1239–1256, Sep. 2013, doi: 10.1016/j.ijheatmasstransfer.2013.04.014.

[75] T. G. Theofanous, J. P. Tu, A. T. Dinh, and T. N. Dinh, "The boiling crisis phenomenon: Part I: nucleation and nucleate boiling heat transfer," *Exp. Therm. Fluid Sci.*, vol. 26, no. 6, pp. 775–792, Aug. 2002, doi: 10.1016/S0894-1777(02)00192-9.

[76] N. Dinh and T. Theofanous, "Nucleation phenomena in boiling," *Multiph. Sci. Technol.*, vol. 15, pp. 349–363, Jan. 2003, doi: 10.1615/MultScienTechn.v15.i1-4.290.

[77]  J. G. Weng, C.P. Grigoropoulos, and C.L. Tien, "Heater size effect on heterogeneous nucleate boiling," in: *IMECE*, (Symp. on Fluid Physics and Heat Transfer for Macro- and Micro- scale Gas-Liquid and Phase-Change Flows), Paper 2-8-2-12, 2001.

[78] J. Frenkel, *Kinetic Theory Of Liquids*. Oxford University Press, 1946. Accessed: Apr. 25, 2024. [Online]. Available: http://archive.org/details/in.ernet.dli.2015.53485

[79] N. Ishida, T. Inoue, M. Miyahara, and K. Higashitani, "Nano Bubbles on a Hydrophobic Surface in Water Observed by Tapping-Mode Atomic Force Microscopy," *Langmuir*, vol. 16, no. 16, pp. 6377–6380, Aug. 2000, doi: 10.1021/la000219r.

[80] J. W. G. Tyrrell and P. Attard, "Images of Nanobubbles on Hydrophobic Surfaces and Their Interactions," *Phys. Rev. Lett.*, vol. 87, no. 17, p. 176104, Oct. 2001, doi: 10.1103/PhysRevLett.87.176104.

[81] J. Yang, C. Narayanan, and D. Lakehal, "Large Eddy & Interface Simulation (LEIS) of disturbance waves and heat transfer in annular flows," *Nucl. Eng. Des.*, vol. 321, pp. 190–198, Sep. 2017, doi: 10.1016/j.nucengdes.2016.10.054.

[82] Y. Sato and B. Niceno, "Large eddy simulation of upward co-current annular boiling flow using an interface tracking method," *Nucl. Eng. Des.*, vol. 321, pp. 69–81, Sep. 2017, doi: 10.1016/j.nucengdes.2017.03.003.

[83] J. Yang, F. Sebilleau, and G. F. Hewitt, "The role of disturbance waves in nucleate boiling in annular flow," *Int. J. Heat Mass Transf.*, vol. 116, pp. 609–616, Jan. 2018, doi: 10.1016/j.ijheatmasstransfer.2017.08.044.

[84] G.-Y. Su, F. P. D'Aleo, B. Phillips, R. M. Streich, E. Al-Safran, J. Buongiorno, and H. M. Prasser, "On the oscillatory nature of heat transfer in steady annular flow," *Int. Commun. Heat Mass Transf.*, vol. 108, p. 104328, Nov. 2019, doi: 10.1016/j.icheatmasstransfer.2019.104328.

[85] Y. Zhou, B. Ji, C. Zhao, H. Bo, Y. Zhang, and H. Li, "Role of bubble dynamics in heat and mass transfer in annular flows," *Int. J. Therm. Sci.*, vol. 191, p. 108348, Sep. 2023, doi: 10.1016/j.ijthermalsci.2023.108348.

[86] D. B. Hann, A. V. Cherdantsev, and B. J. Azzopardi, "Study of bubbles entrapped into a gas-sheared liquid film," *Int. J. Multiph. Flow*, vol. 108, pp. 181–201, Nov. 2018, doi: 10.1016/j.ijmultiphaseflow.2018.07.001.

[87] S. H. Kim, G. C. Lee, J. Y. Kang, K. Moriyama, H. S. Park, and M. H. Kim, "Heat flux partitioning analysis of pool boiling on micro structured surface using infrared visualization," *Int. J. Heat Mass Transf.*, vol. 102, pp. 756–765, Nov. 2016, doi: 10.1016/j.ijheatmasstransfer.2016.06.040.

[88] G. Aguiar, "Infrared Thermometry Analysis of Surface Effects in Subcooled and Saturated Boiling of Water," Ph.D dissertation, Department of Nuclear Science and Engineering, Massachusetts Institute of Technology, Cambridge, MA, 2024. [Online]. Available: https://dspace.mit.edu/handle/1721.1/154320

[89] A. Cioncolini and J. R. Thome, "Entrained liquid fraction prediction in adiabatic and evaporating annular two-phase flow," *Nucl. Eng. Des.*, vol. 243, pp. 200–213, Feb. 2012, doi: 10.1016/j.nucengdes.2011.11.014.

[90] S. Galtier, "Turbulence in space plasmas and beyond," *J. Phys. Math. Theor.*, vol. 51, no. 29, p. 293001, Jun. 2018, doi: 10.1088/1751-8121/aac4c7.

[91] J. Suh, J. Yang, and F. Stern, "The effect of air–water interface on the vortex shedding from a vertical circular cylinder," *J. Fluids Struct.*, vol. 27, no. 1, pp. 1–22, Jan. 2011, doi: 10.1016/j.jfluidstructs.2010.09.001.

[92] S. (陈松涛) Chen, W. (赵伟文) Zhao, and D. (万德成) Wan, "Turbulent structures and characteristics of flows past a vertical surface-piercing finite circular cylinder," *Phys. Fluids*, vol. 34, no. 1, p. 015115, Jan. 2022, doi: 10.1063/5.0078526.

[93] M. Grasso, V. Petrov, and A. Manera, "Accuracy and error analysis of optical liquid film thickness measurement with total internal reflection method (TIRM)," *Exp. Fluids*, vol. 65, no. 6, p. 83, May 2024, doi: 10.1007/s00348-024-03820-1.

[94] T. A. Shedd and T. A. Newell, "Automated optical liquid film thickness measurement method," *Rev. Sci. Instrum.*, vol. 69, no. 12, pp. 4205–4213, Dec. 1998, doi: 10.1063/1.1149232.

# APPENDIX A: FACILITY UPGRADES

### 1. Expanding Mass Flux and Vapor Quality Range

In preliminary experiments aimed at achieving nucleate boiling in thin-film flows, we observed only limited nucleate boiling. The literature review outlined in *Chapter 2* identified liquid film thickness as one of the most influential flow parameters affecting the intensity of boiling. The current test loop, designed to achieve high vapor quality flows, inherently produces thin film flows. To enable the formation of thicker films, the test loop was modified to approximately double the liquid mass flow rate, extending the operational range to higher mass fluxes and lower vapor qualities. This was accomplished by adding a new high-flow liquid pump to the facility, shown in Fig. 38.
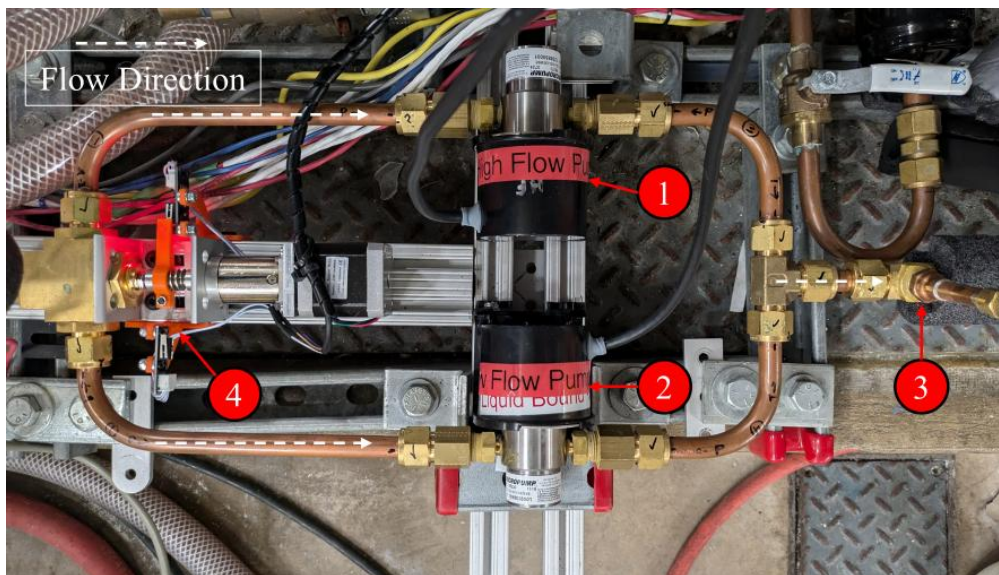


**Fig. 38:** New liquid pump flow layout

The new pump assembly contains the following key components, labeled in the figure:

1. A new high-flow GJN23 pump with DEMSE Eagle Drive
2. The preexisting low-flow GJN21 pump with DEMSE Eagle Drive
3. Schrader valve
4. 3-way valve with electronic actuator

The new high-flow pump is compatible with the same pipe dimensions and voltage source as the existing pump. New control hardware was set up for the second pump using the Click PLC software (the programmable logic controller used to control any PID equipment). The Click PLC hardware setup is similar to the low-flow pump, requiring only small adjustments. Additionally, a Schrader valve was integrated into the design to enable easy evacuation of refrigerant from the line during future repairs, and a 3-way valve was added to direct refrigerant through the active pump. The 3-way valve is actuated by a custom-built electronic actuator controlled through the Click PLC via the main LabView program. Software updates allow users to select either the high-flow or low-flow pump during loop operation. The program shuts down and cuts control to both pumps, actuates the stepper motor to the selected pump, and restores user control, ensuring smooth transitions. Both pumps were retained to preserve our capacity to operate at low liquid flow rates using the low-flow pump while expanding our maximum liquid flow rate using the high-flow pump. All newly created joints in this section of the loop were tested for leaks using a refrigerant leak detector, and the high-flow pump's PID performance was confirmed to be satisfactory.

Fig. 39 illustrates the operational capacity of the flow loop before and after the upgrade. The vapor and liquid flow rates are shown in the far left and bottom cells, respectively, and the vapor quality at each test condition is shown in the colored cells. Green cells indicate viable test conditions, red cells represent unviable test conditions, and yellow cells highlight conditions that are possibly operational but unstable. The maximum liquid mass flow rate increased from 25 g/s to 50 g/s, with the new pump (limiting maximum power to 75% to ensure longevity). The minimum vapor quality decreased from 0.444 to 0.324 allowing for thicker films and boiling at lower heat fluxes.

| Quality | | | | | | | | | | | | | | | | | | | |
|---|---|---|---|---|---|---|---|---|---|---|---|---|---|---|---|---|---|---|---|
| 72 | 0.935 | 0.906 | 0.878 | 0.852 | 0.828 | 0.804 | 0.783 | 0.762 | 0.742 | 0.724 | 0.706 | 0.689 | 0.673 | 0.658 | 0.643 | 0.629 | 0.615 | 0.603 | 0.590 |
| 70 | 0.933 | 0.903 | 0.875 | 0.848 | 0.824 | 0.800 | 0.778 | 0.757 | 0.737 | 0.718 | 0.700 | 0.683 | 0.667 | 0.651 | 0.636 | 0.622 | 0.609 | 0.596 | 0.583 |
| 68 | 0.932 | 0.901 | 0.872 | 0.845 | 0.819 | 0.795 | 0.773 | 0.751 | 0.731 | 0.712 | 0.694 | 0.677 | 0.660 | 0.645 | 0.630 | 0.615 | 0.602 | 0.589 | 0.576 |
| 66 | 0.930 | 0.898 | 0.868 | 0.841 | 0.815 | 0.790 | 0.767 | 0.746 | 0.725 | 0.706 | 0.688 | 0.670 | 0.653 | 0.638 | 0.623 | 0.608 | 0.595 | 0.581 | 0.569 |
| 64 | 0.928 | 0.895 | 0.865 | 0.837 | 0.810 | 0.785 | 0.762 | 0.740 | 0.719 | 0.699 | 0.681 | 0.663 | 0.646 | 0.631 | 0.615 | 0.601 | 0.587 | 0.574 | 0.561 |
| 62 | 0.925 | 0.892 | 0.861 | 0.832 | 0.805 | 0.780 | 0.756 | 0.734 | 0.713 | 0.693 | 0.674 | 0.656 | 0.639 | 0.623 | 0.608 | 0.593 | 0.579 | 0.566 | 0.554 |
| 60 | 0.923 | 0.889 | 0.857 | 0.828 | 0.800 | 0.774 | 0.750 | 0.727 | 0.706 | 0.686 | 0.667 | 0.649 | 0.632 | 0.615 | 0.600 | 0.585 | 0.571 | 0.558 | 0.545 |
| 58 | 0.921 | 0.885 | 0.853 | 0.823 | 0.795 | 0.768 | 0.744 | 0.720 | 0.699 | 0.678 | 0.659 | 0.641 | 0.624 | 0.607 | 0.592 | 0.577 | 0.563 | 0.550 | 0.537 |
| 56 | 0.918 | 0.882 | 0.848 | 0.818 | 0.789 | 0.762 | 0.737 | 0.713 | 0.691 | 0.671 | 0.651 | 0.633 | 0.615 | 0.599 | 0.583 | 0.569 | 0.554 | 0.541 | 0.528 |
| 54 | 0.915 | 0.878 | 0.844 | 0.812 | 0.783 | 0.755 | 0.730 | 0.706 | 0.684 | 0.663 | 0.643 | 0.624 | 0.607 | 0.590 | 0.574 | 0.560 | 0.545 | 0.532 | 0.519 |
| 52 | 0.912 | 0.874 | 0.839 | 0.806 | 0.776 | 0.748 | 0.722 | 0.698 | 0.675 | 0.654 | 0.634 | 0.615 | 0.598 | 0.581 | 0.565 | 0.550 | 0.536 | 0.523 | 0.510 |
| 50 | 0.909 | 0.870 | 0.833 | 0.800 | 0.769 | 0.741 | 0.714 | 0.690 | 0.667 | 0.645 | 0.625 | 0.606 | 0.588 | 0.571 | 0.556 | 0.541 | 0.526 | 0.513 | 0.500 |
| 48 | 0.906 | 0.865 | 0.828 | 0.793 | 0.762 | 0.733 | 0.706 | 0.681 | 0.658 | 0.636 | 0.615 | 0.596 | 0.578 | 0.561 | 0.545 | 0.530 | 0.516 | 0.503 | 0.490 |
| 46 | 0.902 | 0.860 | 0.821 | 0.786 | 0.754 | 0.724 | 0.697 | 0.672 | 0.648 | 0.626 | 0.605 | 0.586 | 0.568 | 0.551 | 0.535 | 0.520 | 0.505 | 0.492 | 0.479 |
| 44 | 0.898 | 0.854 | 0.815 | 0.779 | 0.746 | 0.715 | 0.688 | 0.662 | 0.638 | 0.615 | 0.595 | 0.575 | 0.557 | 0.540 | 0.524 | 0.509 | 0.494 | 0.481 | 0.468 |
| 42 | 0.894 | 0.848 | 0.808 | 0.771 | 0.737 | 0.706 | 0.677 | 0.651 | 0.627 | 0.604 | 0.583 | 0.564 | 0.545 | 0.528 | 0.512 | 0.497 | 0.483 | 0.469 | 0.457 |
| 40 | 0.889 | 0.842 | 0.800 | 0.762 | 0.727 | 0.696 | 0.667 | 0.640 | 0.615 | 0.593 | 0.571 | 0.552 | 0.533 | 0.516 | 0.500 | 0.485 | 0.471 | 0.457 | 0.444 |
| 38 | 0.884 | 0.835 | 0.792 | 0.752 | 0.717 | 0.685 | 0.655 | 0.628 | 0.603 | 0.580 | 0.559 | 0.539 | 0.521 | 0.503 | 0.487 | 0.472 | 0.458 | 0.444 | 0.432 |
| 36 | 0.878 | 0.828 | 0.783 | 0.742 | 0.706 | 0.673 | 0.643 | 0.615 | 0.590 | 0.567 | 0.545 | 0.526 | 0.507 | 0.490 | 0.474 | 0.459 | 0.444 | 0.431 | 0.419 |
| 34 | 0.872 | 0.819 | 0.773 | 0.731 | 0.694 | 0.660 | 0.630 | 0.602 | 0.576 | 0.553 | 0.531 | 0.511 | 0.493 | 0.476 | 0.459 | 0.444 | 0.430 | 0.417 | 0.405 |
| 32 | 0.865 | 0.810 | 0.762 | 0.719 | 0.681 | 0.646 | 0.615 | 0.587 | 0.561 | 0.538 | 0.516 | 0.496 | 0.478 | 0.460 | 0.444 | 0.430 | 0.416 | 0.403 | 0.390 |
| 30 | 0.857 | 0.800 | 0.750 | 0.706 | 0.667 | 0.632 | 0.600 | 0.571 | 0.545 | 0.522 | 0.500 | 0.480 | 0.462 | 0.444 | 0.429 | 0.414 | 0.400 | 0.387 | 0.375 |
| 28 | 0.848 | 0.789 | 0.737 | 0.691 | 0.651 | 0.615 | 0.583 | 0.554 | 0.528 | 0.505 | 0.483 | 0.463 | 0.444 | 0.427 | 0.412 | 0.397 | 0.384 | 0.371 | 0.359 |
| 26 | 0.839 | 0.776 | 0.722 | 0.675 | 0.634 | 0.598 | 0.565 | 0.536 | 0.510 | 0.486 | 0.464 | 0.444 | 0.426 | 0.409 | 0.394 | 0.380 | 0.366 | 0.354 | 0.342 |
| 24 | 0.828 | 0.762 | 0.706 | 0.658 | 0.615 | 0.578 | 0.545 | 0.516 | 0.490 | 0.466 | 0.444 | 0.425 | 0.407 | 0.390 | 0.375 | 0.361 | 0.348 | 0.336 | 0.324 |
| 22 | 0.815 | 0.746 | 0.688 | 0.638 | 0.595 | 0.557 | 0.524 | 0.494 | 0.468 | 0.444 | 0.423 | 0.404 | 0.386 | 0.370 | 0.355 | 0.341 | 0.328 | 0.317 | 0.306 |
| 20 | 0.800 | 0.727 | 0.667 | 0.615 | 0.571 | 0.533 | 0.500 | 0.471 | 0.444 | 0.421 | 0.400 | 0.381 | 0.364 | 0.348 | 0.333 | 0.320 | 0.308 | 0.296 | 0.286 |
| 18 | 0.783 | 0.706 | 0.643 | 0.590 | 0.545 | 0.507 | 0.474 | 0.444 | 0.419 | 0.396 | 0.375 | 0.356 | 0.340 | 0.324 | 0.310 | 0.298 | 0.286 | 0.275 | 0.265 |
| | 5 | 7.5 | 10 | 12.5 | 15 | 17.5 | 20 | 22.5 | 25 | 27.5 | 30 | 32.5 | 35 | 37.5 | 40 | 42.5 | 45 | 47.5 | 50 |

**Vapor Mass Flow Rate [g/s]** (vertical axis)

**Liquid Mass Flow Rate [g/s]**

| Low-Flow Pump | High-Flow Pump |
|---|---|

Hewitt-Roberts Flow Map Can't say regime

**Fig. 39:** Loop operational capacity map

At low liquid flow rates, the maximum vapor flow rate is constrained by the maximum pump power. As the liquid flow rate is increased, the maximum vapor flow rate becomes restricted by the loop's capacity to condense and cool the two-phase mixture exiting the test section. Currently, this bottleneck is in the main return valve from the condensing heat exchanger which limits flow to the adequately sized heat pumps. Resizing this valve is a potential area for future improvement but is adequate for current testing needs. The minimum flow rate is dictated by the flow regime. For liquid flow rates below 25 g/s, the minimum vapor flow rate aligns with the transition between annular and slug flow as predicted using the Hewitt-Roberts flow map. For liquid flow rates above 25 g/s, flow maps predict a lower minimum vapor flow rate than the loop can sustain. Experimental results suggest that the flow prematurely transitions to the slug regime at the minimum vapor flow rate values shown in Fig. 39, establishing a new lower limit.

## 2. Saturation Pressure Control Valve

In our initial high heat flux testing, we determined that the saturation temperature control was insufficient. Saturation temperature in the facility is controlled by modulating the flow rate through the main condenser following the test section. Previously, this flow rate was manually adjusted using a quarter-turn ball valve, which required frequent and sensitive tuning whenever mass flux or inlet vapor quality changed. This manual process was prone to inconsistencies between loop operators and failed to dynamically respond to increases in heat flux. Consequently, the steady-state saturation temperature would gradually rise as heat flux increased and cooling power remained static.

Additionally, cycling of the heat pump introduced significant variations in saturation temperatures. Fig. 40(a) illustrates this effect during a 20-minute test in which heating power was gradually increased from 0-400 W. Without the PID controller, saturation temperature fluctuated dramatically as the heat pump cycled mid-test. These variations negatively affect many of our measure variables. To solve this problem, we replaced the quarter-turn ball valve with an electronically actuated valve (Hanbay Inc. MCM-050AF-3-1913TT-SE-075-BAV6 multiturn ball valve, Fig. 40(b)), controlled with a PID system. This valve was selected to achieve precise control of the coolant flow rate and sized to approximately match the valve coefficient of the previously installed valve. When the test was repeated under identical conditions with the PID valve, the saturation temperature remained stable throughout, demonstrating the efficacy of the new control scheme.
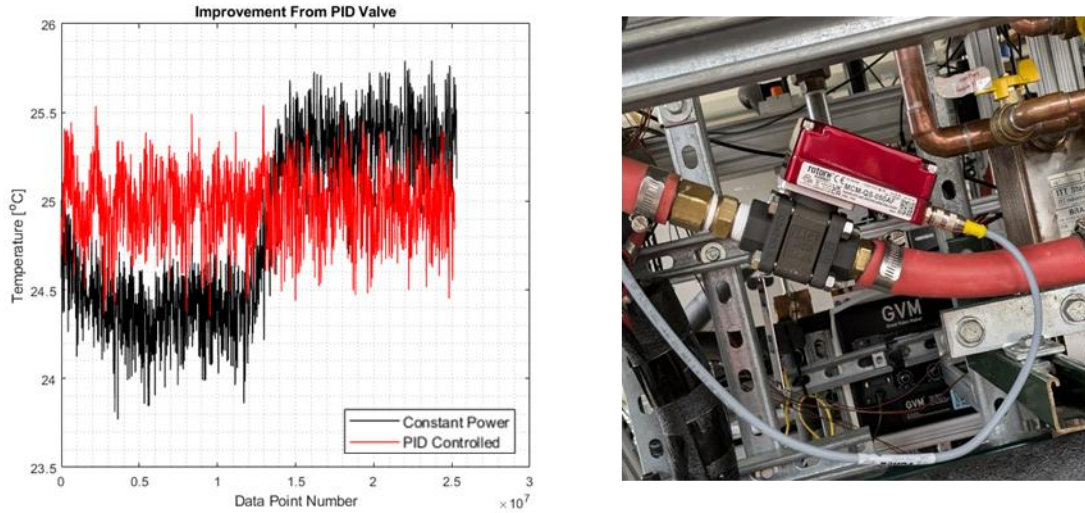
**Fig. 40:** (left) Refrigerant saturation temperature during an experimental run with and without the PID controlled valve and (right) photograph of the new PID-controlled saturation pressure valve

Tuning the valve PID was a complex process. Initial trial-and-error attempts to identify suitable gain values revealed that a single set of parameters could not accurately control the saturation temperature across all test conditions. To address this, the PID controller was manually tuned over a range of vapor inlet qualities and mass fluxes to generate a table of gain values. This data was then analyzed and plotted against vapor mass flow rate ($m_v$), inlet quality ($x$), and mass flux to identify trends.

From this analysis, the integral gain ($I$), derivative gain ($D$), and sample rate were found to be strong functions of vapor mass flow rate and are expressed as follows:

$$I = (2.746749 * 10^{-5}) * m_v^4 - 0.004692 * m_v^3 + 0.303941 * m_v^2 - 9.042997 * m_v + (1.156878 * 10^2)$$

$$D = (9.186478 * 10^{-6}) * m_v^4 - 0.001618 * m_v^3 + 0.105729 * m_v^2 - 3.088340 * m_v + 36.749884$$

$$Sample\ Rate = 0.001003 * m_v^4 - 0.174242 * m_v^3 + 0.105729 * m_v^2 - 3.088340 * m_v + 36.749884$$

The proportional gain ($P$) did not initially exhibit a clear relationship to the tested variables. However, upon further investigation, a linear relationship with inlet quality was identified and expressed as:

$$P = 5.453824 * x^3 - 10.627340 * x^2 + 7.145465 * x - 0.944482$$

These equations provide accurate control across the loop operational capacity shown in Fig. 39 but would likely require adjustment if substantial modifications are made to the flow loop.

### 3. FTO Partitioning for Variable Power Heating

A key objective for achieving nucleate boiling in the flow loop is to locally control the boiling location. We postulated that the current FTO coating on our test section windows could be manipulated to produce localized heat by electrically isolating sections of the coating to create higher resistance areas (example in Fig. 41). The heat flux generated by the coating depends on the coated area through which the electrical current flows. As the coated area is reduced toward the center of the sample in Fig. 41, the current density must increase, resulting in a higher local heat flux. This design would allow the isolated portion of the coating to be powered independently, enabling precise control over localized heating while preserving optical access.
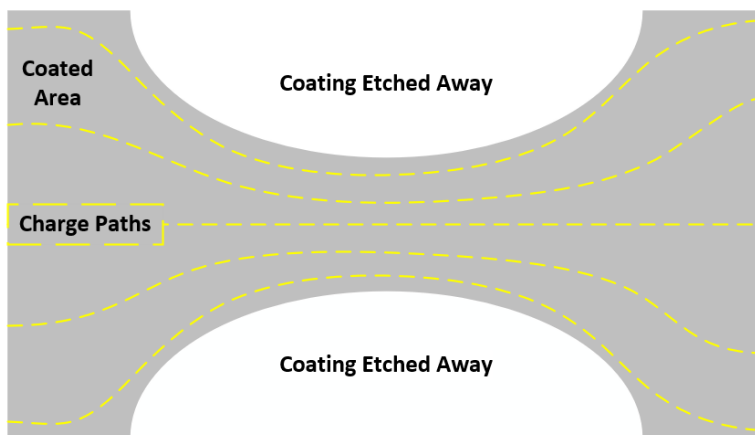


**Fig. 41:** Schematic of film modification to achieve local high heat flux

Etching the FTO coating required a specific chemical process. Through conversations with the window manufacturer, Delta Technologies, the chemical etching process shown below was developed using Kapton tape to mask the desired coated areas. The following steps require the listed chemicals, a large (>500 mL) beaker, a graduated cylinder, a spray bottle, a small metal

spatula, Kapton tape, scissors, a cotton swab, a squeegee, baking soda (or any basic powder to neutralize acids for disposal), and personal protective equipment (nitrile gloves, lab coat, safety glasses, and a fume hood for the etching step).

### Step 1: Window Preparation

1. Clean window with acetone
2. Rinse window with IPA
3. Mix soapy water in a spray bottle and spray onto the window and tape
4. Apply wet tape to the window
5. Arrange and cut tape as desired
6. Squeegee out excess water
7. Rearrange the tape to the final desired position
8. Let dry (24-48 hours)

### Step 2: Etching

1. Pour 208.23 mL of DI water into a large beaker
2. Measure 41.77 mL of 37% concentrated HCl and pour into the DI water (the resulting HCl aqueous solution should be at a 6.18% volume concentration)
3. Using a spatula, apply zinc powder evenly across the surface of the substrate. Remove any excess zinc powder from the surface by shaking the substrate lightly (zinc powder is essential to the etching process)
4. Submerge the substrate in the HCl solution. This will start a reaction between the hydrochloric acid, the zinc powder, and the FTO
5. Leave the substrate for 3 minutes for the reaction to complete
6. Rinse away any excess hydrochloric acid using deionized water and firmly wipe away any leftover residue using a cotton swab. You should be left with an FTO strip covered in tape
7. Peel away the tape and remove any remaining adhesive using isopropyl alcohol
8. Neutralize acidic solution using baking soda and clean as required

Thermal imaging of samples created using this etching process are shown in Fig. 42(a) and (b). A simple straight-line etch of just the bottom half of the window (Fig. 42(a)) was performed as a proof of concept. Although attaching electrical connections to these samples proved challenging, the thermal images demonstrated that the etched region remained unheated while the coated upper half successfully conducted electrical current. Following this initial success, the more complex pattern shown in Fig. 41 was attempted. The most challenging aspect of the process was

cleanly cutting and applying the Kapton tape. For future experiments, a laser cutter may be used to produce more precise tape masks. Differences in infrared transparency between the FTO-coated and bare glass make the thermal images difficult to interpret. It is evident that the etching process created a partitioned surface. This was confirmed using a manual thermocouple reader which measured the center region was around 10 °C hotter than the wider coated areas. The bright halo around the narrowest coated point is a result of heat spreading into the uncoated glass which has a different infrared transparency than the coated glass.



(a)                                                                                  (b)
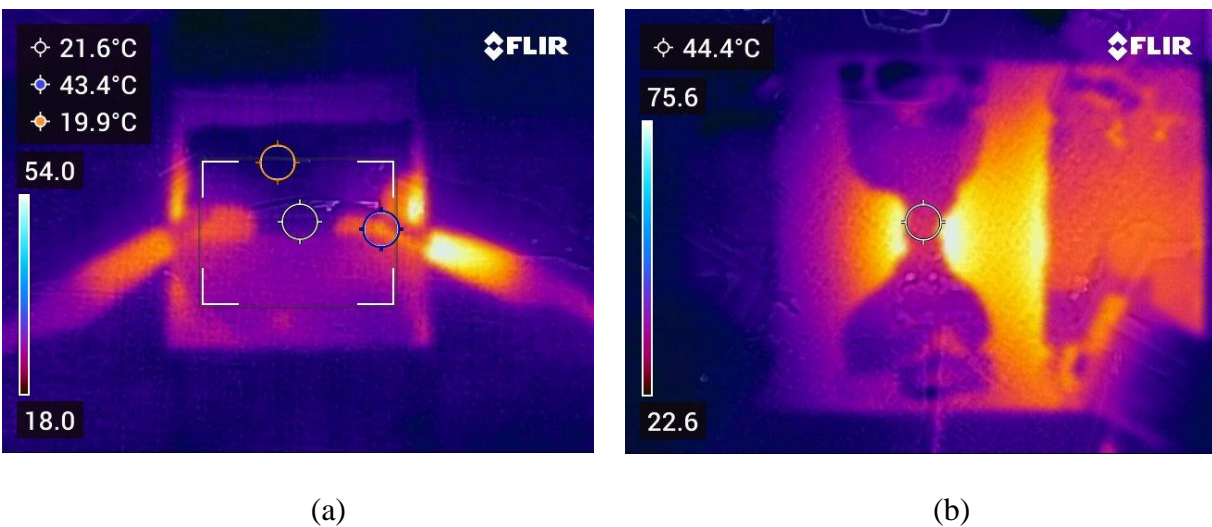
**Fig. 42:** IR images of electrically heated windows with (a) simple and (b) variable area chemically etched areas

### 4. Test Section Power Limitations

Nucleate boiling will only occur if the surface heat flux is high enough to produce sufficient superheat to initiate boiling. As a result, one of the goals of this work was to increase the heater power. The maximum sustainable power for the test section is currently limited in three ways:

1.      The maximum of the power supplies

2.      The wire gauge connecting the power supply to the contact pins

3.      The maximum current rating of the contact pins

This section will quantify these limits and discuss the current power capabilities.

The front and back of the test section are heated by two synced power supplies. The front window is powered by a XANTREX XDC 300-20 (300 V, 20 A) and the back window is powered by a XANTREX XDC 100-60 (100V, 60 A). This puts the maximum possible input power into each window at 2 kW using 100 V and 20 A. We currently use 18 AWG wires to connect the power supplies to the test section windows. 18 AWG wire have a maximum current rating of 20 A, matching the maximum possible current from the power supplies. The contact pins that connect the wires to the test section film have voltage rating of 150 VDC, and a 2 A limit through each pin set (each window passes the power through 4 sets of pins in parallel with each set containing 10 individual pins). The pin design thus limits the total voltage through each window to 150 volts and the total current to 80 amps. In our prior experiments, tests usually max out at 600 W. However, with the currently installed components, we can comfortably run up to 1350 W, limiting the maximum voltage to 90 V and the maximum current to 15 A.

The other possible concern brought up in discussions of pushing the current heating limits, particularly locally, is cracking the test section windows. In the current test section design, there is a small gap to allow the window to expand before contacting its housing. In a SolidWorks temperature-induced stress simulation, 1kW of power was put into a window with an additional 100 W of local heating through a rectangular heating patch stretching the width of the window and 50 mm tall. This heating did not cause anything close to mechanical failure with a factor of safety of 74. This gives confidence that increasing heat flux to the maximum possible values outlined previously won't cause the type of failure seen in previous multi-window iterations of the test section design.

## APPENDIX B: OBSTRUCTED FLOW DRYOUT AREA

The dryout area for the large obstruction at all test conditions can be seen in Fig. 43 – Fig. 45 for the low, medium, and high mass fluxes, respectively. The inlet quality and heat flux at the time of imaging can be seen in the individual image titles. The grid of images in each figure is organized with each row having the same inlet quality and with increasing heat flux moving from the left-most column to the right-most column. The dry area is manually identified and highlighted in red. These measurements were used to quantify the effect of different flow parameters on dry area as presented in Fig. 22 – Fig. 24(b). The dry area for all small obstruction tests can be seen in Fig. 46 – Fig. 48.

**Fig. 43:** Images downstream of the large obstruction at G=130 kg/m$^2$-s with dry wake area highlighted in red.

G=150 [kg/m$^2$-s]

| $x_{in}$=0.64 [-], $q_{eff}$=0.0 [kW/m$^2$] | $x_{in}$=0.64 [-], $q_{eff}$=13.1 [kW/m$^2$] | $x_{in}$=0.64 [-], $q_{eff}$=18.4 [kW/m$^2$] | $x_{in}$=0.64 [-], $q_{eff}$=22.3 [kW/m$^2$] |

| $x_{in}$=0.72 [-], $q_{eff}$=0.0 [kW/m$^2$] | $x_{in}$=0.72 [-], $q_{eff}$=13.1 [kW/m$^2$] | $x_{in}$=0.72 [-], $q_{eff}$=18.4 [kW/m$^2$] | $x_{in}$=0.72 [-], $q_{eff}$=21.0 [kW/m$^2$] |

| $x_{in}$=0.80 [-], $q_{eff}$=0.0 [kW/m$^2$] | $x_{in}$=0.80 [-], $q_{eff}$=13.1 [kW/m$^2$] | $x_{in}$=0.80 [-], $q_{eff}$=15.7 [kW/m$^2$] | $x_{in}$=0.80 [-], $q_{eff}$=18.4 [kW/m$^2$] |

| $x_{in}$=0.88 [-], $q_{eff}$=0.0 [kW/m$^2$] | $x_{in}$=0.88 [-], $q_{eff}$=10.5 [kW/m$^2$] | $x_{in}$=0.88 [-], $q_{eff}$=13.1 [kW/m$^2$] | $x_{in}$=0.88 [-], $q_{eff}$=15.6 [kW/m$^2$] |

| $x_{in}$=0.96 [-], $q_{eff}$=0.0 [kW/m$^2$] | $x_{in}$=0.96 [-], $q_{eff}$=2.5 [kW/m$^2$] | $x_{in}$=0.96 [-], $q_{eff}$=8.8 [kW/m$^2$] | $x_{in}$=0.96 [-], $q_{eff}$=10.0 [kW/m$^2$] |

**Fig. 44:** Images downstream of the large obstruction at G=150 kg/m$^2$-s with dry wake area highlighted in red.

G=170 [kg/m$^2$-s]

$x_{in}$=0.63 [-], $q_{eff}$=0.0 [kW/m$^2$]   $x_{in}$=0.63 [-], $q_{eff}$=13.0 [kW/m$^2$]   $x_{in}$=0.63 [-], $q_{eff}$=26.2 [kW/m$^2$]   $x_{in}$=0.63 [-], $q_{eff}$=28.8 [kW/m$^2$]

$x_{in}$=0.71 [-], $q_{eff}$=0.0 [kW/m$^2$]   $x_{in}$=0.71 [-], $q_{eff}$=13.0 [kW/m$^2$]   $x_{in}$=0.71 [-], $q_{eff}$=23.6 [kW/m$^2$]   $x_{in}$=0.71 [-], $q_{eff}$=24.9 [kW/m$^2$]

$x_{in}$=0.79 [-], $q_{eff}$=0.0 [kW/m$^2$]   $x_{in}$=0.79 [-], $q_{eff}$=13.1 [kW/m$^2$]   $x_{in}$=0.79 [-], $q_{eff}$=18.3 [kW/m$^2$]   $x_{in}$=0.79 [-], $q_{eff}$=19.6 [kW/m$^2$]

$x_{in}$=0.86 [-], $q_{eff}$=0.0 [kW/m$^2$]   $x_{in}$=0.86 [-], $q_{eff}$=10.4 [kW/m$^2$]   $x_{in}$=0.86 [-], $q_{eff}$=13.0 [kW/m$^2$]   $x_{in}$=0.86 [-], $q_{eff}$=15.6 [kW/m$^2$]

$x_{in}$=0.95 [-], $q_{eff}$=0.0 [kW/m$^2$]   $x_{in}$=0.95 [-], $q_{eff}$=5.1 [kW/m$^2$]   $x_{in}$=0.95 [-], $q_{eff}$=8.9 [kW/m$^2$]   $x_{in}$=0.95 [-], $q_{eff}$=12.6 [kW/m$^2$]

**Fig. 45:** Images downstream of the large obstruction at G=170 kg/m$^2$-s with dry wake area highlighted in red.

G=130 [kg/m$^2$-s]

$x_{in}$=0.62 [-], $q_{eff}$=0.0 [kW/m$^2$]  $x_{in}$=0.62 [-], $q_{eff}$=12.9 [kW/m$^2$]  $x_{in}$=0.62 [-], $q_{eff}$=26.0 [kW/m$^2$]  $x_{in}$=0.62 [-], $q_{eff}$=27.3 [kW/m$^2$]

$x_{in}$=0.70 [-], $q_{eff}$=0.0 [kW/m$^2$]  $x_{in}$=0.70 [-], $q_{eff}$=12.9 [kW/m$^2$]  $x_{in}$=0.70 [-], $q_{eff}$=20.8 [kW/m$^2$]  $x_{in}$=0.70 [-], $q_{eff}$=23.4 [kW/m$^2$]

$x_{in}$=0.78 [-], $q_{eff}$=0.0 [kW/m$^2$]  $x_{in}$=0.78 [-], $q_{eff}$=12.9 [kW/m$^2$]  $x_{in}$=0.78 [-], $q_{eff}$=15.6 [kW/m$^2$]  $x_{in}$=0.78 [-], $q_{eff}$=16.9 [kW/m$^2$]

$x_{in}$=0.87 [-], $q_{eff}$=0.0 [kW/m$^2$]  $x_{in}$=0.87 [-], $q_{eff}$=12.9 [kW/m$^2$]  $x_{in}$=0.87 [-], $q_{eff}$=15.6 [kW/m$^2$]  $x_{in}$=0.87 [-], $q_{eff}$=16.9 [kW/m$^2$]

$x_{in}$=0.95 [-], $q_{eff}$=0.0 [kW/m$^2$]  $x_{in}$=0.95 [-], $q_{eff}$=7.7 [kW/m$^2$]  $x_{in}$=0.95 [-], $q_{eff}$=10.3 [kW/m$^2$]  $x_{in}$=0.95 [-], $q_{eff}$=13.0 [kW/m$^2$]

**Fig. 46:** Images downstream of the small obstruction at G=130 kg/m$^2$-s with dry wake area highlighted in red.

G=150 [kg/m²-s]



**Fig. 47:** Images downstream of the small obstruction at G=150 kg/m²-s with dry wake area highlighted in red.

G=170 [kg/m$^2$-s]

$x_{in}$=0.63 [-], $q_{eff}$=0.0 [kW/m$^2$]   $x_{in}$=0.63 [-], $q_{eff}$=13.0 [kW/m$^2$]   $x_{in}$=0.63 [-], $q_{eff}$=26.1 [kW/m$^2$]   $x_{in}$=0.63 [-], $q_{eff}$=28.7 [kW/m$^2$]

$x_{in}$=0.70 [-], $q_{eff}$=0.0 [kW/m$^2$]   $x_{in}$=0.70 [-], $q_{eff}$=12.9 [kW/m$^2$]   $x_{in}$=0.70 [-], $q_{eff}$=23.4 [kW/m$^2$]   $x_{in}$=0.70 [-], $q_{eff}$=24.7 [kW/m$^2$]

$x_{in}$=0.78 [-], $q_{eff}$=0.0 [kW/m$^2$]   $x_{in}$=0.78 [-], $q_{eff}$=12.9 [kW/m$^2$]   $x_{in}$=0.78 [-], $q_{eff}$=18.2 [kW/m$^2$]   $x_{in}$=0.78 [-], $q_{eff}$=19.5 [kW/m$^2$]

$x_{in}$=0.86 [-], $q_{eff}$=0.0 [kW/m$^2$]   $x_{in}$=0.86 [-], $q_{eff}$=10.3 [kW/m$^2$]   $x_{in}$=0.86 [-], $q_{eff}$=12.9 [kW/m$^2$]   $x_{in}$=0.86 [-], $q_{eff}$=15.6 [kW/m$^2$]

$x_{in}$=0.94 [-], $q_{eff}$=0.0 [kW/m$^2$]   $x_{in}$=0.94 [-], $q_{eff}$=5.1 [kW/m$^2$]   $x_{in}$=0.94 [-], $q_{eff}$=9.0 [kW/m$^2$]   $x_{in}$=0.94 [-], $q_{eff}$=13.0 [kW/m$^2$]
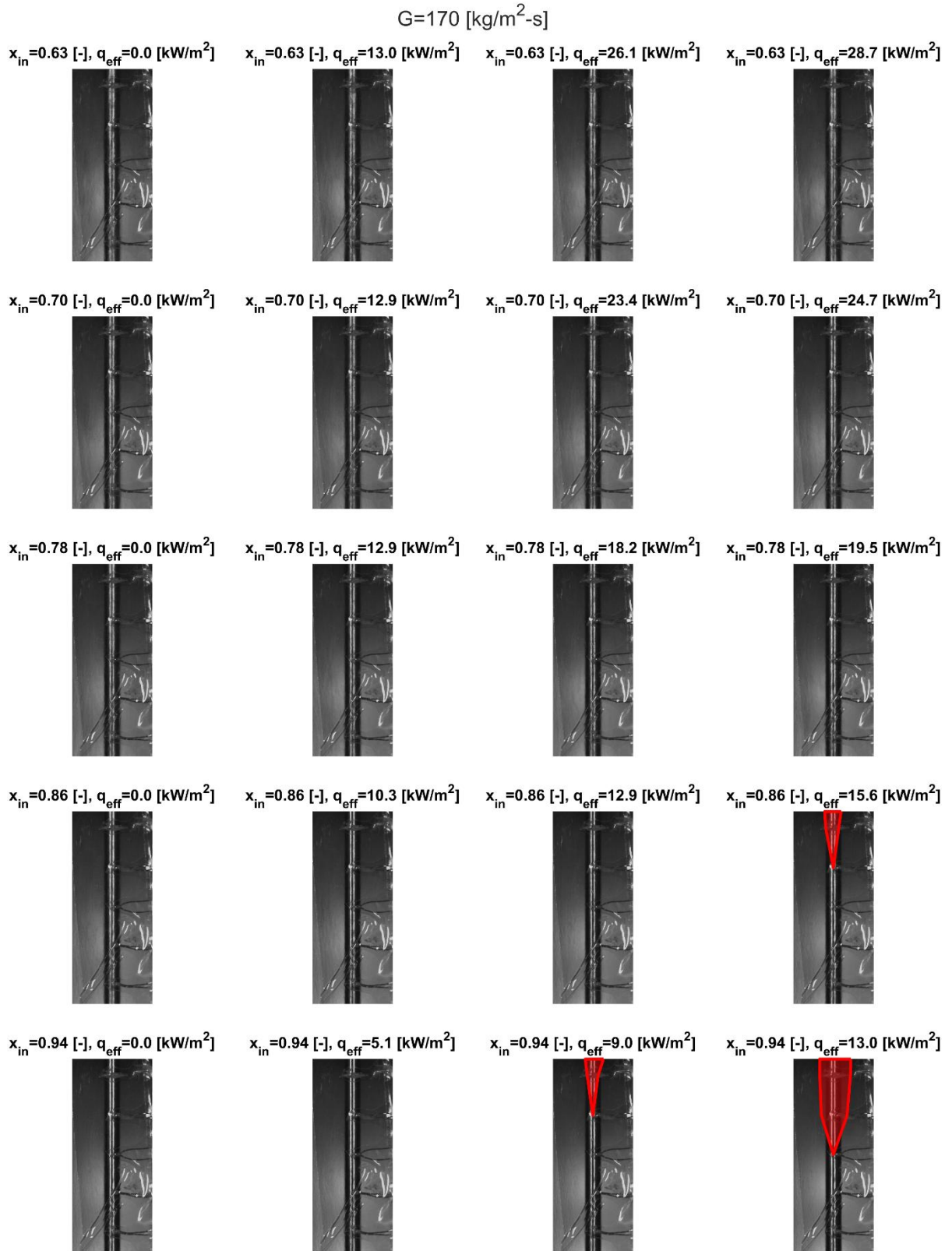
**Fig. 48:** Images downstream of the small obstruction at G=170 kg/m$^2$-s with dry wake area highlighted in red.

A comparison of the dry wake width at each measurement point at all test conditions and obstruction diameters can be seen in Fig. 49. This figure shows the half wake width taken as the average between the distance from the left and right side of the wake to the center of the flow. The measurement locations can be seen in Fig. 63 with positions 0 and 6 being the bottom and top of the viewable area of the camera respectively. A subset of this data is shown in Fig. 23.
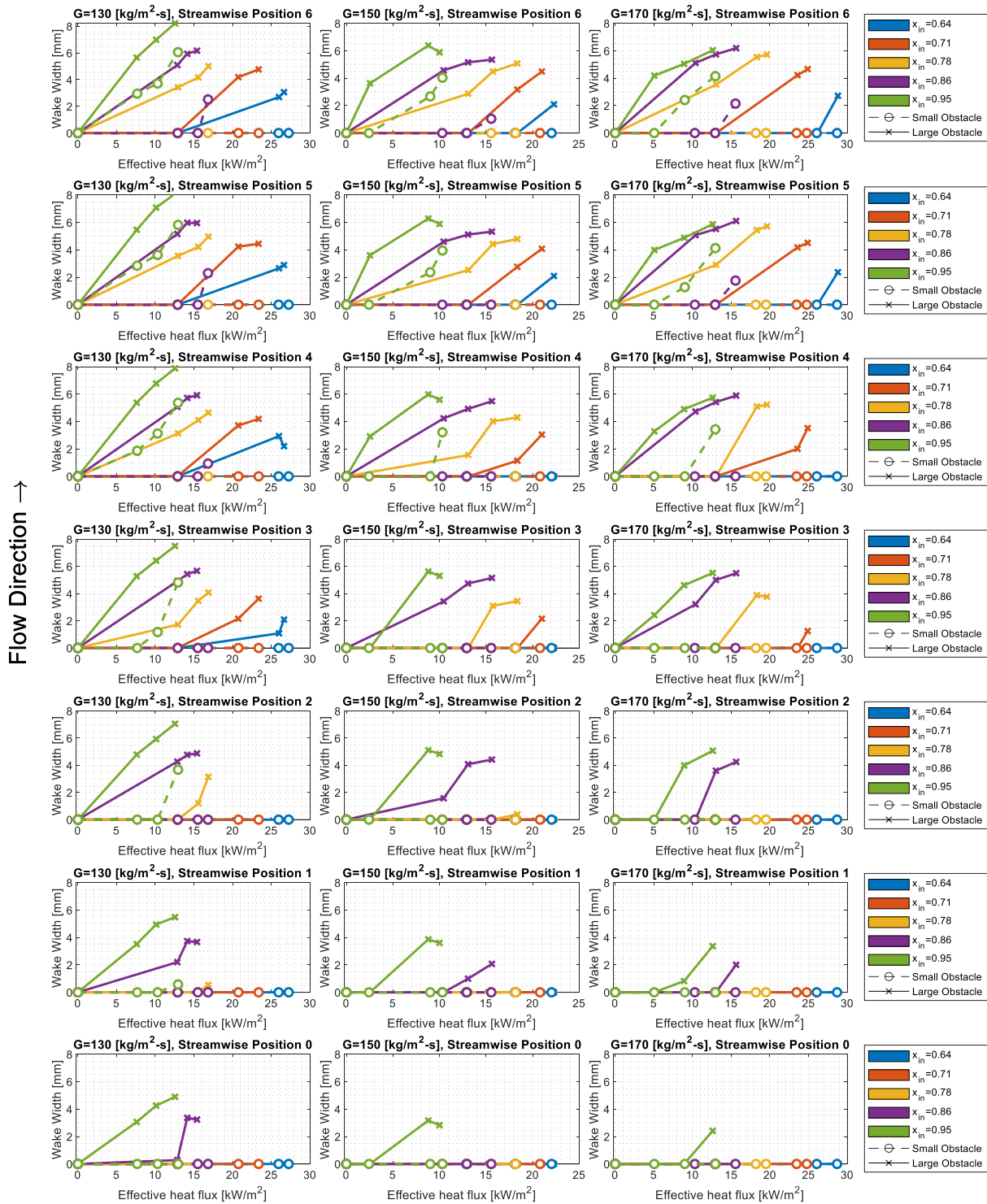
**Fig. 49:** Averaged half-wake width at all measurement positions and flow conditions

# APPENDIX C: FILM THICKNESS PROGRAM DESCRIPTION

## 1. Optical Theory

The total internal reflectance film thickness sensor relies on the difference in the index of refraction between the liquid film and the vapor core. When light passes from the high index liquid ($n_1$) into the low-index vapor ($n_2$), the angle of transmission ($\theta_2$) will be larger than the angle of instance ($\theta_1$) according to Snell's law (equation (23)).

$$n_1 \sin(\theta_1) = n_2 \sin(\theta_2) \tag{23}$$

When the incident angle is sufficiently large for a given index ratio, the angle of transmission can reach 90°. When this occurs, the light is totally internally reflected at the interface. The required incident angle for total internal reflection is called the critical angle, and computed by rearranging equation (23) for a transmission angle of 90°:

$$\theta_{crit} = \sin^{-1}\left(\frac{n_2}{n_1}\right) \tag{24}$$

Our film thickness sensors rely on the critical angle to deduce the liquid film thickness, as illustrated in Fig. 50. The sensor contains a light source, some optics, and a high-speed camera. Incident light originating from a light source (in our case, a 10 mW, 632 nm HeNe laser) is diffused by tape adhered to the outside of the test section window. The diffused rays then propagate in the liquid before reaching the liquid-vapor interface. When the incident angle is greater than the critical angle (equation (24)), the light totally internally reflects and is directed back towards the light source.
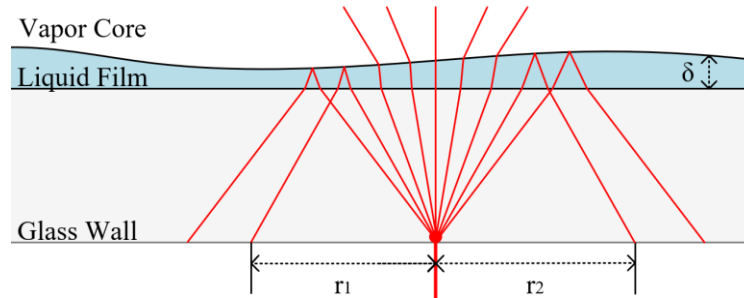
**Fig. 50:** Theoretical light paths from a point light source when using the total internal reflectance film thickness measurement technique

The reflected light rays eventually reach the diffusing tape, forming a ring. This ring is not perfectly circular, rather, each light ray will reflect independently, meaning the radial distance, $r$, between the center of the incident light and the edge of the light ring yields film thickness measurement for that specific ray. In practice, groups of radii or all radii are often averaged or fit to an ellipse to yield higher accuracy measurements. These light rings can be captured using high-speed video so that individual frames can be analyzed with an image-processing algorithm to measure changes in film thickness over time. To be meaningful, however, two calibration procedures are required. First, an object of known size (typically some sort of high-accuracy ruler) must be imaged at the diffusing tape to provide a conversion value, $c_{pixel}$, between the number of pixels and the actual distance. Second, the ring formed in a dry test section must be imaged and its radii, $r_{dry}$, measured. The actual thickness of the liquid film is a function of the difference between the dry and wet radii. Using Snell's law, the film thickness, $\delta$, can be calculated using equations (31). Fig. 51 combined with equations (25)-(30) show the derivation of equation (31).
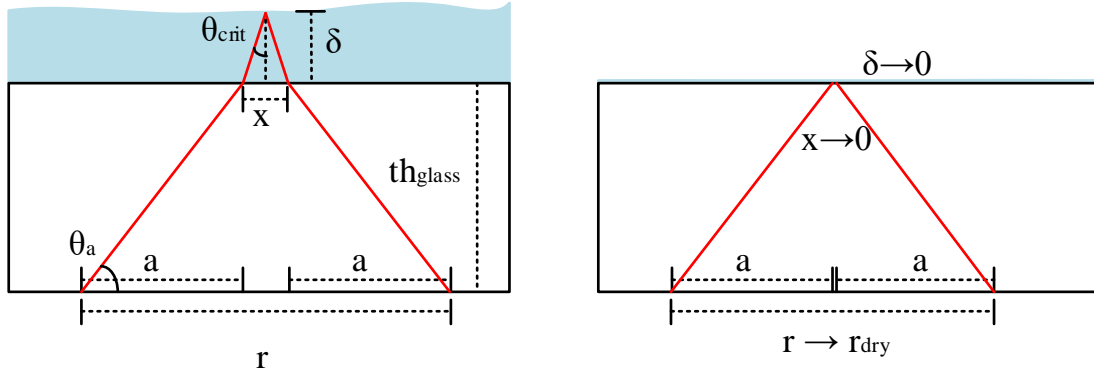
**Fig. 51:** Diagram of a single light path for film thickness equation derivation

$$n_{glass} \sin(90 - \theta_1) = n_{liquid}\sin(\theta_{crit}) \tag{25}$$

$$a = \frac{th_{glass}}{\tan(\theta_1)} \tag{26}$$

$$x = 2\delta\tan(\theta_{crit}) \tag{27}$$

$$r = 2a + x \tag{28}$$

In the limit that $\delta$ approaches 0, the distance x approaches zero, and the radius measure approaches the dry radius so that,

$$r_{dry} = 2a \tag{29}$$

$$r - r_{dry} = 2\delta\tan(\theta_{crit}) \tag{30}$$

$$\delta = \frac{(r - r_{dry})}{2\tan(\theta_{crit})}c_{pixel} \tag{31}$$

### 2. Image Processing

The image processing algorithm works by taking the image of the light ring and extracting four rectangular slices (upper, lower, right, and left) to form a cross. It takes the gradient of brightness of the pixels in each slice, averaged across the width of the rectangle. The maximum value of the gradient is used to identify the edge of the light ring. The image is then rotated according to the user specified number of measurement points (see Fig. 54) and the gradient of a new range of pixels is measured. Fig. 52 shows an example of these rectangular slices and the

pixel gradient measurement. The parameters listed below are different ways of interacting with the program to best detect the light ring.
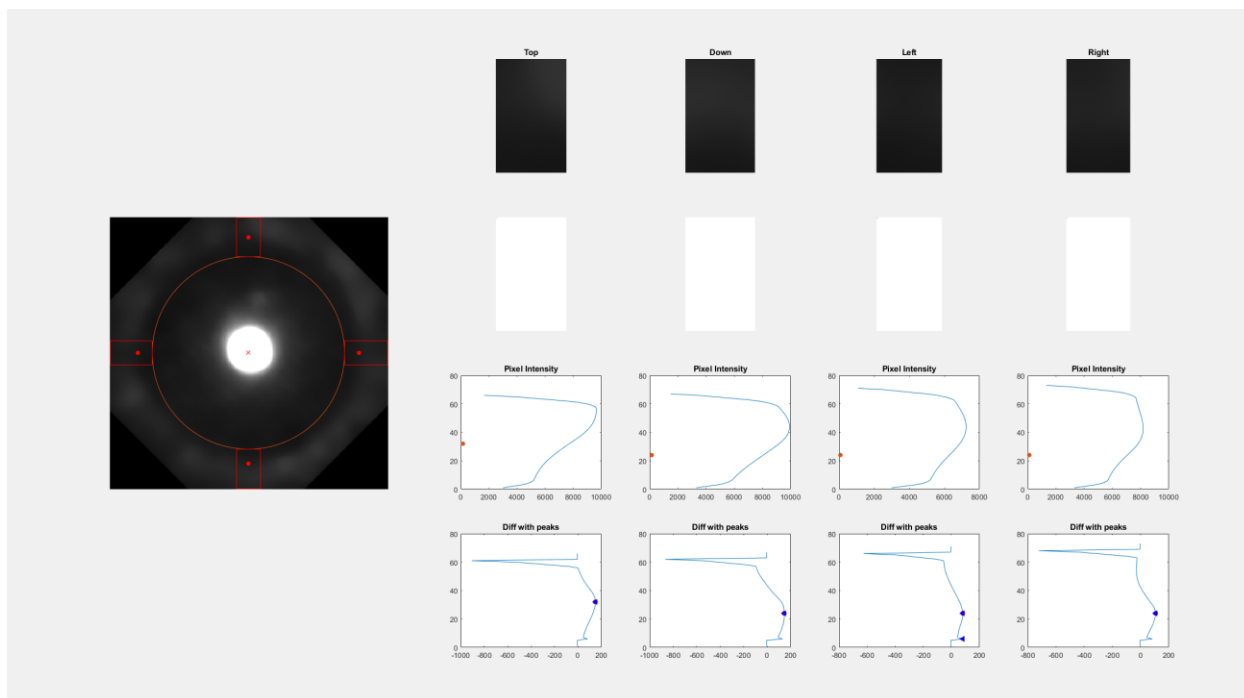


**Fig. 52:** Basics of the image processing algorithm

To initiate data analysis, first the captured high-speed video must be converted to TIF files and saved to folders based on the test conditions. The processing algorithm will process and save data in files named according to the folder name from which it collects the images. To begin pre-processing, open and run ImageAdjuster_App.mlapp, ensuring the rest of the image processing files are in the current folder path. This app is a GUI that allows the user to interact with the image-processing MATLAB files. The ImageAdjuster app will load presets which may be altered by editing the ImageAdjuster_App.mat file.

Once the GUI is open, load film thickness images into the app using the files dropdown in the upper left corner. This dropdown also allows the user to save the parameters they use to process their images or load in parameters used previously. After all parameters have been selected, they must be saved as they will be used for the data post-processing. We will go through each option

and panel in the app and describe their functionality before discussing the processing algorithm in *Appendix C Section 3*. The main hub for image pre-processing and processing is the ImageEngine.m file. This will direct user inputs through the ImageProcess.m file while automatically running through TIF images or the ImagePreprocess.m file during the setup stages.

**2.1 Detection**

The detection panel changes the settings that the processing algorithm will use to alter the images and detect the light ring. An example image in the detection panel is shown in Fig. 53.
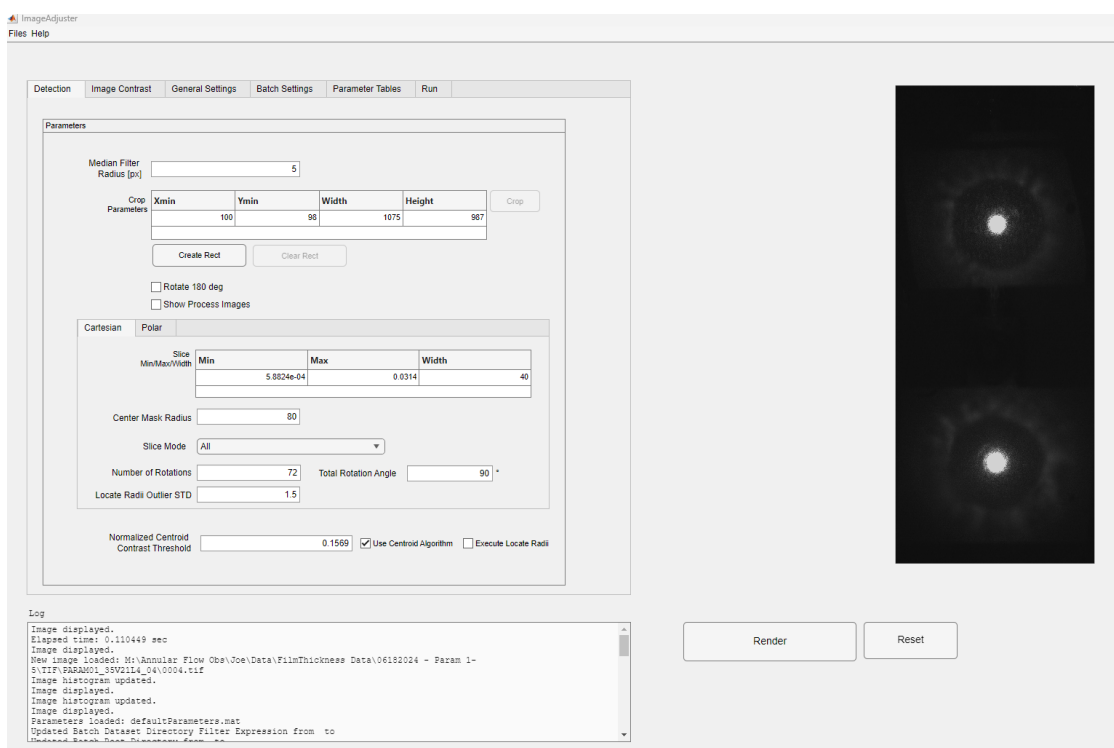


**Fig. 53:** The detection panel

The median filter radius box allows the user to smooth out some of the noise in the light ring image. This uses the MATLAB function medfilt2 to clean up random noise. Medfilt2 takes the sets a pixel value to the median value of pixels within the range specified by the user. This filter should not be overused as it does change the image but can be useful for getting more consistent

measurements and preventing outliers in the data. For a dry test section, a filter around 20 works well, with a range close to 5 working well for wet test sections.

The crop parameters box allows the user to create a rectangle that will act as the crop area for image processing. The user may pre-define the size and location of the rectangle in the table or can manually fit the rectangle to the desired part of the image. To manually resize the crop area, click Create Rect and manipulate the create object as desired. When finished, the user must click Crop to reduce the full image and save the selected data. To view the cropped image or reset back to the original image, select Render or Reset respectively.

The Rotate 180-degree checkbox will rotate the rendered images by 180 degrees. The Show Process Images checkbox will show all the intermediary steps used to determine the light ring location. This can be useful when determining how well the algorithm is identifying the light ring using the selected input parameters. This checkbox was selected when generating Fig. 52.

The Cartesian box allows the user to set many important parameters. The "Slice" table allows the user to manipulate how the rectangular slices are taken and interpreted by the program. The width box allows the user to set the width of the rectangular slices used to detect the ring as seen in Fig. 52. The algorithm averages the pixel intensity over the width of the rectangle, so a large width may not give an accurate measurement due to the curvature of the ring, but a small width may be too narrow to detect a peak. The min box allows the user to set the minimum pixel gradient peak height that will be accepted as the edge of the ring. The code uses the MATLAB function findpeaks to find the local maxima, which can be filtered to only return peaks higher than a minimum peak height value. The max box allows the user to exclude peaks higher than some maximum value, eliminating obvious outliers. For our experiments, a minimum value of

$5.8824*10^{-4}$, a maximum value of 0.0314, a width of 30-50 for wet test section images, and a width of 5-10 for dry test section images tend to work well.

The center mask radius sets a radius of pixels from the center that will not be considered when calculating the pixel intensity. This ring can be seen in Fig. 52. Maximizing the size of this center mask allows the code to run faster as it does not have to take the intensity of as many pixels, and it may eliminate some false peaks from the data. The center mask radius must at least be large enough to cover the entirety of the bright spot caused by the incident laser.

The slice mode drop-down box is another very important input. This allows the user to select which points they want to be included in the final fitting to the light ring. When using the All mode, every detected point is used to fit an ellipse. The major and minor radii (reported as Rx and Ry) of this ellipse will then be exported after processing. The Top-Bottom slice mode only uses the radii from the top and bottom rectangles. In this processing mode, the radii detected at the top and bottom of the ring are averaged to yield a single value for the top and bottom radius. The Left-Right slice mode operates in the same way using the left and right sides of the ring. The Individual-Points slice mode is currently an experimental feature that has not produced reliable results. The idea is to report the radii of each reported point separately categorized by their angle from the right horizontal. The program can successfully report these radii, but there is too much variability in the data to get a usable profile across the entire radius.

The image is rotated around the center of the crop box specified by the user with the number of rotations and total rotation angle being used to manipulate which parts of the ring the rectangular slices will measure. The number of rotations controls the number of data points taken between the maximum and minimum angles. The total rotation angle controls how wide of a field the rectangles

will cover which is ± ½ of the total rotation angle centered on the x and y axes. An example diagram of this can be seen in Fig. 54.
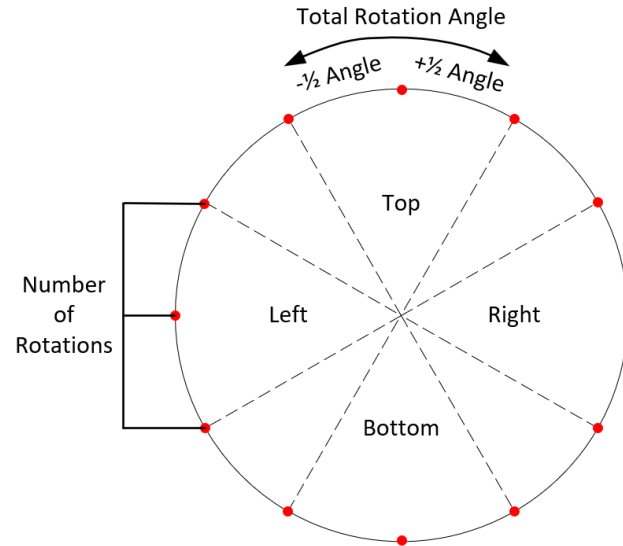


**Fig. 54:** Measurement point placement diagram

The Locate Radii Outlier STD box allows the user to remove outlier measurement points which are a certain number of standard deviations away from the mean radii. Any radii beyond the number of deviations specified by the user will be labeled as outliers and not considered in the data.

The Normalized Centroid Contrast Threshold and the Use Centroid Algorithm check box are legacy features that are no longer actively used in the code, but their structure is available if desired. Previously, the intersection of the rectangular slices was located at the centroid of the bright spot at the center of the light ring. The normalized threshold allowed the user to manipulate which pixels were considered when calculating the centroid. Currently, the intersection of the rectangular slices is located at the x and y center of the rectangular crop box.

The Execute Local Radii selection box will render the detected light points when the user clicks the render button and reports the major and minor radii as well as the root mean squared (RMS) error between the existing radii and the ellipse fit by the program.

## 2.2 Image Contrast

The Image Contrast tab shown in Fig. 55 allows the user to adjust the minimum and maximum pixel intensity. Pixels below the minimum value will be set to 0 while pixels above the maximum are set to 1, with all other pixels between the setpoints preserving their original values. This function can be useful for eliminating noise and getting a cleaner edge for the light ring.
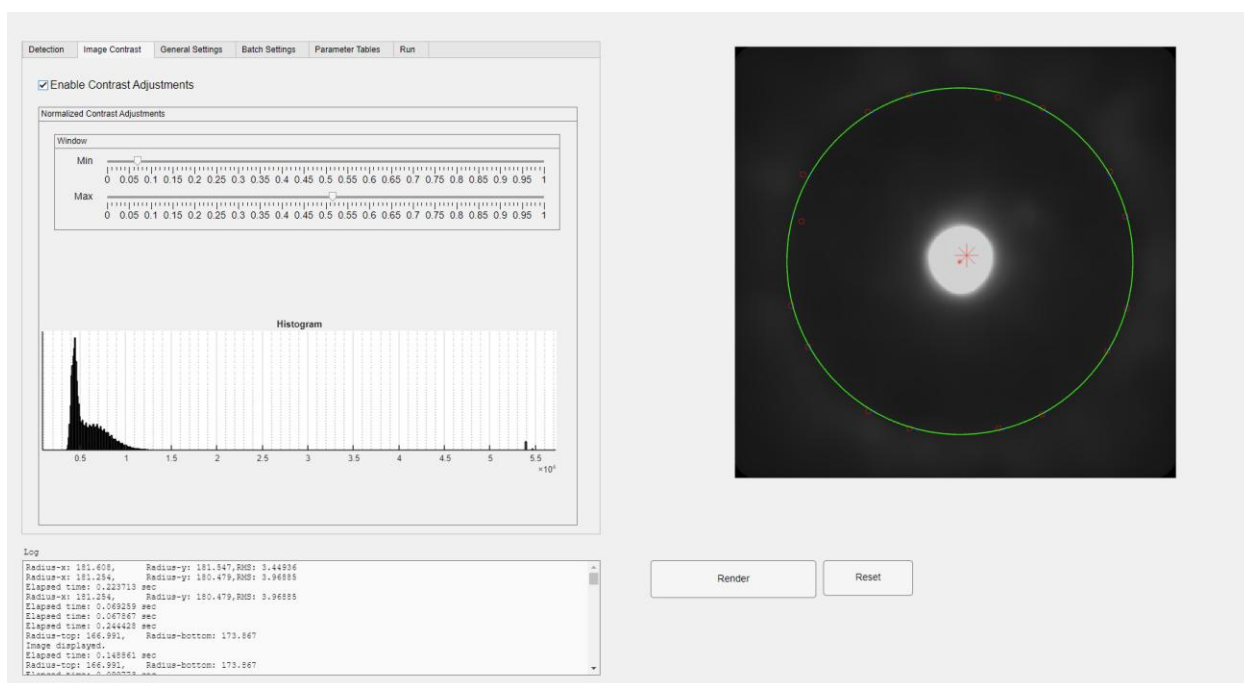


**Fig. 55:** Image contrast adjustment Panel

## 2.3 General Settings

The general settings tab is for loading in the image folder file paths and setting other calibration values. Clicking "browse" next to any of the four directory or image rows will open the file explorer. Pixel Calibration should path to a single TIF image used for pixel scaling. The Dry Calibration Directory should path to the folder of TIF images of the light ring created in a dry

test section. The First Pass Image Directory should path to a folder containing TIF images of the light ring to be measured. This is usually a subset of images that you want to use to test how well the set parameters measure the light ring. The Result File Directory should path to a folder where the results are to be saved.

The Image Filename Regex Expression is used to filter the TIF images inside each filter. Any strings in this box should follow the Regex structure. For example, the expression seen in Fig. 56 will allow the algorithm to be fed in files with an optional "FilmThickness" string followed by exactly 6 digits between 0 and 9 and ending with .tif. It will match files such as 123456.tif or FilmThickness123456.tif. If no files following the Regex naming structure are found in the folder, the program will yield an error.

The next few elements are related to the pixel calibration. When the user selects Run Pixel Calibration, the program will render the image from the path given above. Then, the user must create a rectangular crop box on the newly rendered image seen in the image display. After the image has been cropped, the user will select several pairs of points equal to the Pixel Calibration Trials box that are a known distance apart in micrometers listed in the Pixel Reference size box. After all pairs have been selected on the image, the program will automatically update the Pixel Size box with the pixels-to-microns conversion factor.

The lowest set of boxes allows the user to set the refractive indexes. These values will be used to calculate film thickness according to equation (31), so they should be precise. For our current experiments, the glass window is 3 mm thick and has an index of refraction of 1.5216, liquid R245fa has an index of 1.2576, and vapor R245fa has an index of 1.0006.

The final dropdown box allows the user to select the image bit depth of the selected files. If this value is set incorrectly, the program will read an image full of static. Our current experiments use 16-bit images.

The three checkboxes on the right of the pixel calibration area are for high-speed processing of images. This will allow the user to accelerate the processing with the GPU or using parallel cores. The Asynchronous file download box allows the user to run the program without future input.
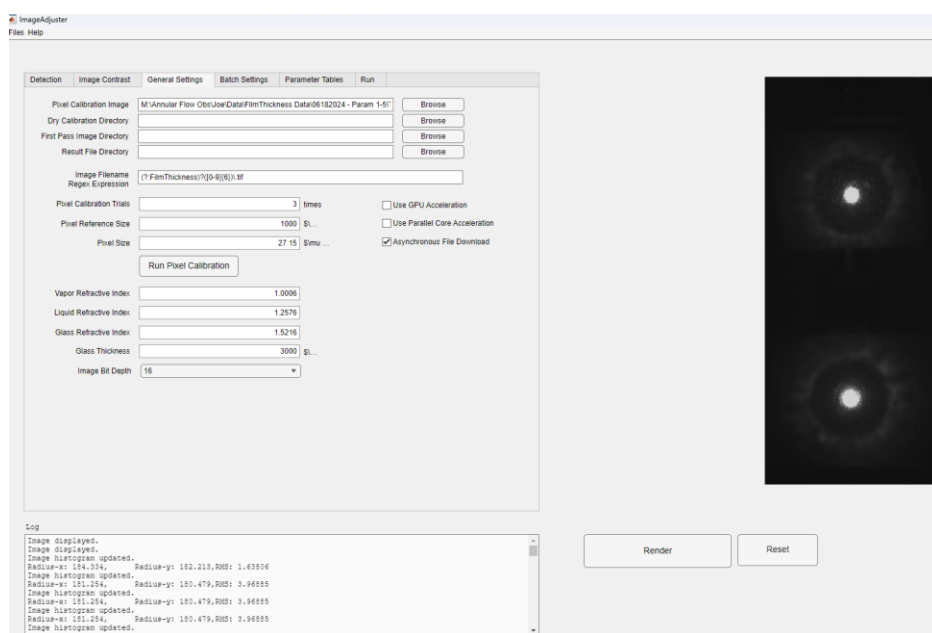


**Fig. 56:** General settings tab

### 2.4 Batch Settings

In the Batch Settings tab, the user gives the file path to the root directory where the subfolders containing the TIF files to be processed are held. This list of subfolders can be further filtered through the Batch Dataset Directory Filter Expression or by manually selecting the folders to be processed after selecting List. In the filter expression, the user can input a statement like "PARAM10*" which would limit the number of processed folders to those containing the string PARAM10. To reset manually selected folders, simply click list again. Standard rules following

multiple file selection through the control and shift keys may be used. By default, the program will attempt to process every folder in the batch directory.
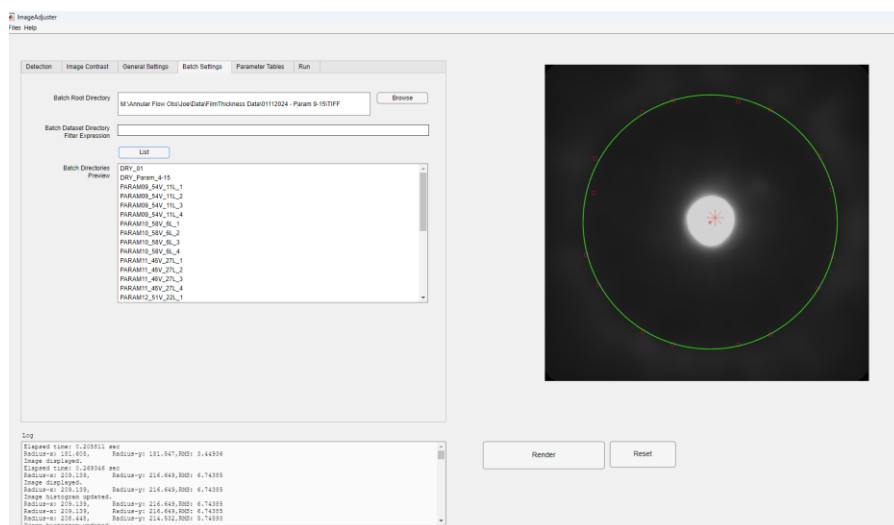


**Fig. 57:** Batch settings tab

## 2.5 Final Checks

The existing parameters can be viewed in the Parameter Tables Tab. The parameters should be tested on a few loaded images to ensure accuracy across the image test set. When all parameters have been tuned to their final values, the user should save the parameters by using the Files dropdown. To run the program, use the Run tab and select Batch Run or First Pass to run through the given folders as described previously. A progress bar will be displayed in the Log as the program runs. While a run of many images will take time, the algorithm can be sped up with GPU acceleration, parallel computing, or by limiting the number of data points taken using the total number of rotations.

## 3. Data Post-Processing

### 3.1 Results File

The files produced by the image processing program will be saved to the supplied results folder as listed previously named "results_struct_XXX". This file is a structure with three fields.

The first field is an ID that matches the name of the folder from which the images were pulled. The second field is titled "procs" and contains the calculated radii in pixels. The title of the subfields of procs will depend on the mode used to run the program. For example, if the Top-Bottom mode is used, the procs will contain fields titled Rtop, Rbottom, RMS, and intVals. Rtop and Rbottom give their respective radii in pixels, while RMS gives the root means squared of how well the ellipse used by the program fits the ring. In the case of the Top-Bottom mode, the no ellipse is fit to the ring, so this value is NaN. The intVals field contains other useful information about the location of the measured film thickness points. The first and second columns contain the x and y coordinates of the film thickness points on the image for possible future reference. The ninth column lists the special coordinates of the points more clearly. Along with the x and y coordinates, the radii, rotation angle, and quadrant (top, bottom, left, or right listed as 4, 2, 3, and 1 respectively) are listed. The functionality for the postprocs field is currently not implemented.

### 3.2 FilmThickness Program

Over years of gathering film thickness data, our lab has created many scripts for processing data. These, however, were highly personalized to the needs of the time. Therefore, only two programs, FilmThickness.m and combineFTresults.m, will be described.

FilmThickness.m is a Class that allows for quick calculation and plotting of the film thickness results from the image processing algorithm. To interact with the film thickness file, the user must first use the combineFTresults.m script. This script is simple and serves to combine different results files into an easily interpretable format. The user needs to supply the results file directory as well as any naming filters using the same filter format used in Batch Settings. The filtered files must contain the result structure generated for the dry test section. The program will yield a file named results_composite that will be saved to the workspace and should be subsequently saved to

the user's results folder. This script has been marked for future integration either directly into the imaging processing algorithm or into the film thickness program but remains separate for now.

The film thickness program is mostly automated with the exception that the fps should be manually set. Incorrectly setting the fps will not affect the film thickness measurements but will yield incorrect time scaling when the results structures are plotted. FilmThickness.m being a Class means it is not run like a normal script and can be called in other scripts. Data can be loaded into the program using the Command Window through a command similar to

ft = CoreProcessors.FilmThickness("results_struct.m", "ImgParams.m")

where results_struct is the file path to the composite results structure from the combining script and ImgParams is the file path to the parameters file saved from the image processing GUI. The program will then save a structure of data named ft (ft can be renamed as desired) to the workspace.

The film thickness program does several things when it is called. First, it interprets the supplied files and throws an error if inappropriate files are supplied. If the correct files are supplied, the program will find the mean radius of the dry ring. This dry ring should be a perfect circle with a constant radius. However, the manual crop around the dry ring means the center of the measurement points is not necessarily the center of the ring, creating a consistent offset between the measured radii and the actual radii. The film thickness program takes the mean of the dry radii and creates an offset between the measured radii and the mean radii to move the measured ring center to the actual ring center. This offset is saved and applied to all wetted measurements. The program then uses equation (31) to convert the supplied radii measurements in pixels to an actual film thickness.

The resultant structure from the program will be a combination of the supplied composite structure beginning with the results from the dry calibration. Each substructure contains a name,

the mean dry radius, the offset used, the raw ring radii, the full raw results_struct and imgparameters data, the fps used, individual film thickness, mean thickness, and standard deviation in film thickness. These results can be visualized through the integrated plotFT function. This function has many preset plotting options which can be manually changed in the program or specified when called. For example, the supplied command

ft.plotFT('plotAverageFT', true, 'movingAverageWindow', 30)

will plot the average calculated film thickness over the supplied radii using the movmean function to smooth the data by calculating the mean between 30 neighboring points. Many options can be used to quickly customize and manipulate the plotted data. If FilmThickness.m is in the current file path, it can be called in subsequent scripts to consolidate the processing of film thickness data.

## APPENDIX D: SUPPORT ASSEMBLY VALIDATION

A recurring concern has been whether the large support assembly securing the obstruction contributes more to the observed dryout physics than the obstruction itself. Particularly, this issue resurfaced as the experimental range of the test section was expanded, necessitating a validation study. Fig. 58 presents the temperature measured in what would be the far downstream wake region of the flow if the obstruction cylinder were present. The figure compares temperature data from a plain test section with those from a test section containing only the support assembly (excluding the obstruction cylinder) under conditions spanning the experimental range discussed in *Chapter 5*. As seen in Fig. 58 (b) and (c), the support assembly has no discernible effect on temperature. A very minor temperature difference (<1 °C) is observed in Fig. 58 (a) at the lowest inlet vapor quality tested. These findings, supported by visual evaluation of the flow, confirm with high confidence that the obstruction cylinder alone is the primary cause of the dryout phenomenon reported.
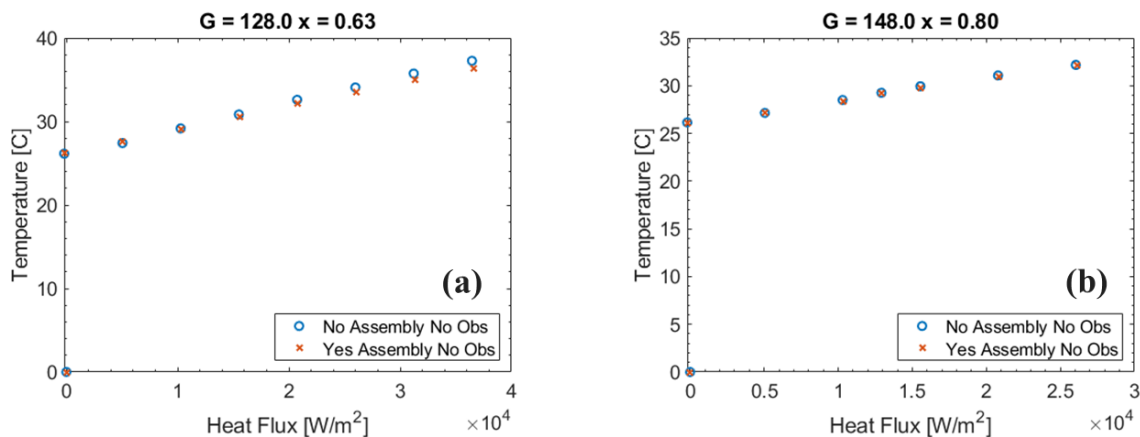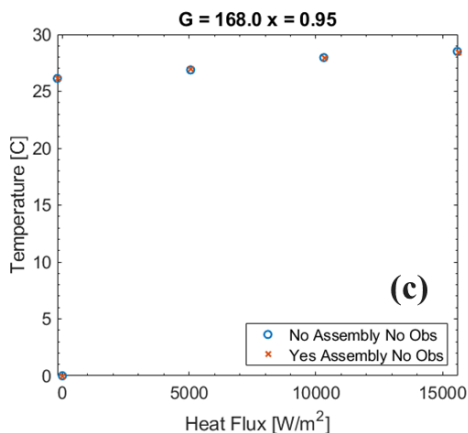
**Fig. 58:** Comparison of temperature measured in a totally unobstructed test section and a test section with the obstruction assembly but no cylinder at the range of conditions tested in *Chapter 6*

This study was expanded slightly to evaluate the broader range of operating conditions that are possible with the loop upgrades. The results of this study, shown in Fig. 60 and Fig. 61, indicate that within the previously tested range, mass flux has a minor effect whereas small variations in vapor quality have a more pronounced impact. This trend is shown in Fig. 59 (a) and (b). In Fig. 59 (a), the support assembly yields an approximately 2 ℃ temperature difference at the maximum tested heat flux. As the vapor quality is increased to the conditions shown in Fig. 59 (b), this temperature difference shrinks to approximately 1.5 ℃. If a significant influence on the wall temperature is defined as a difference exceeding 1 ℃, the support assembly becomes significant at inlet vapor qualities below 0.55. The relationship between the support assembly and the wall temperature is likely linked to the droplet deposition rate. Specifically, the support assembly may have a greater influence on the droplet deposition rate at low compared to high vapor qualities.
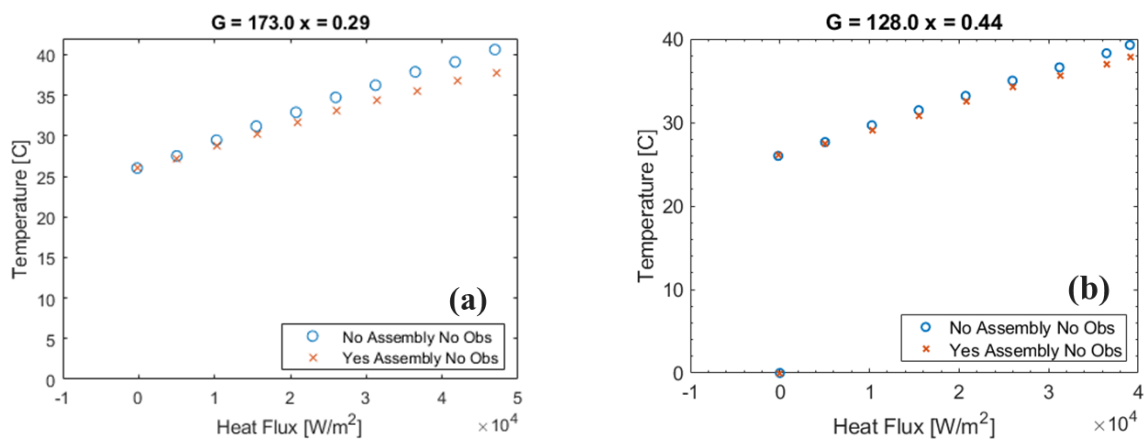
**Fig. 59:** Comparison of temperature measured in a totally unobstructed test section and a test section with the obstruction assembly but no cylinder at low inlet vapor quality
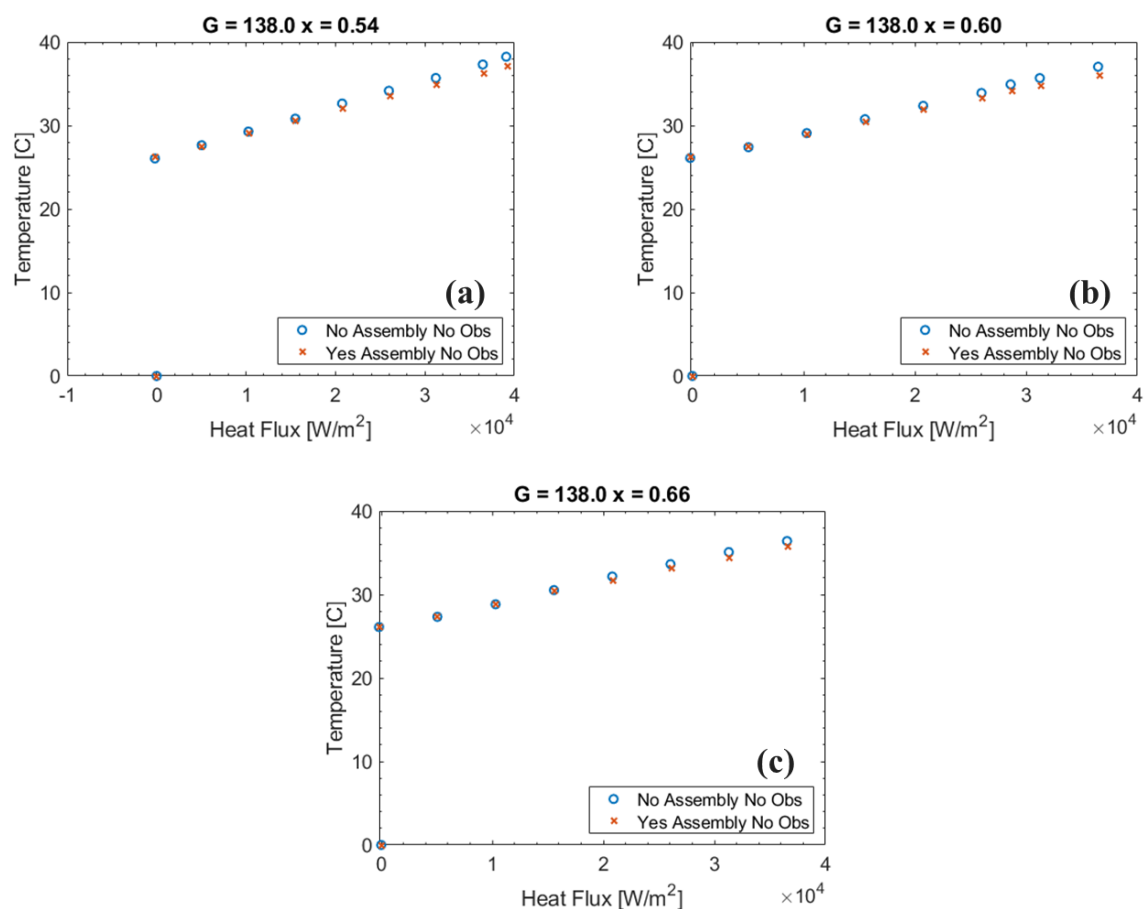


**Fig. 60:** Comparison of temperature measured in a totally unobstructed test section and a test section with the obstruction assembly but no cylinder at a constant mass flux and varying inlet quality
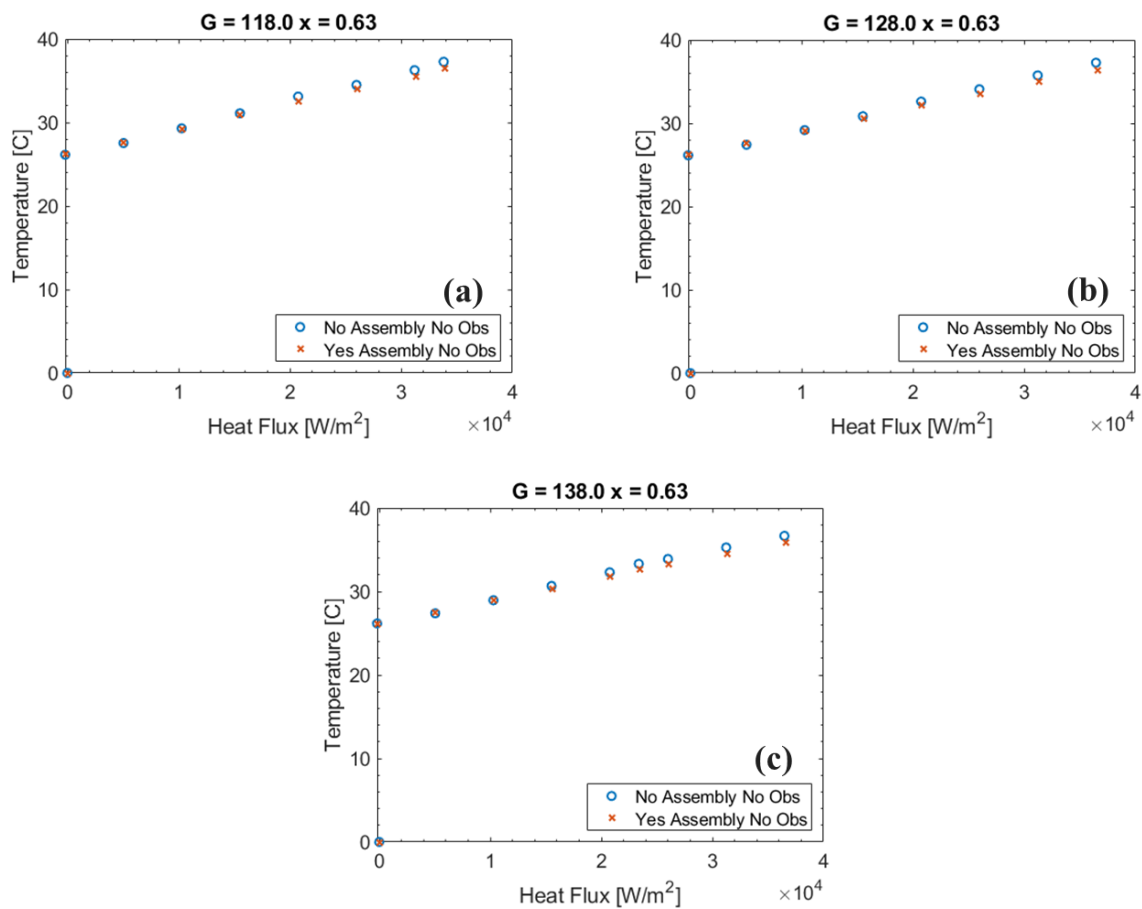
**Fig. 61:** Comparison of temperature measured in a totally unobstructed test section and a test section with the obstruction assembly but no cylinder at a constant inlet quality and varying mass flux

# APPENDIX E: TEMPERATURE TIME-TRACE DATA

## 1. Large Diameter Obstacle (2.5mm)

G=148 [kg/m²-s], x_inlet=0.64

G=148 [kg/m²-s], x_inlet=0.71

G=148 [kg/m²-s], x_inlet=0.78

G=148 [kg/m²-s], x_inlet=0.86

G=148 [kg/m²-s], x_inlet=0.95
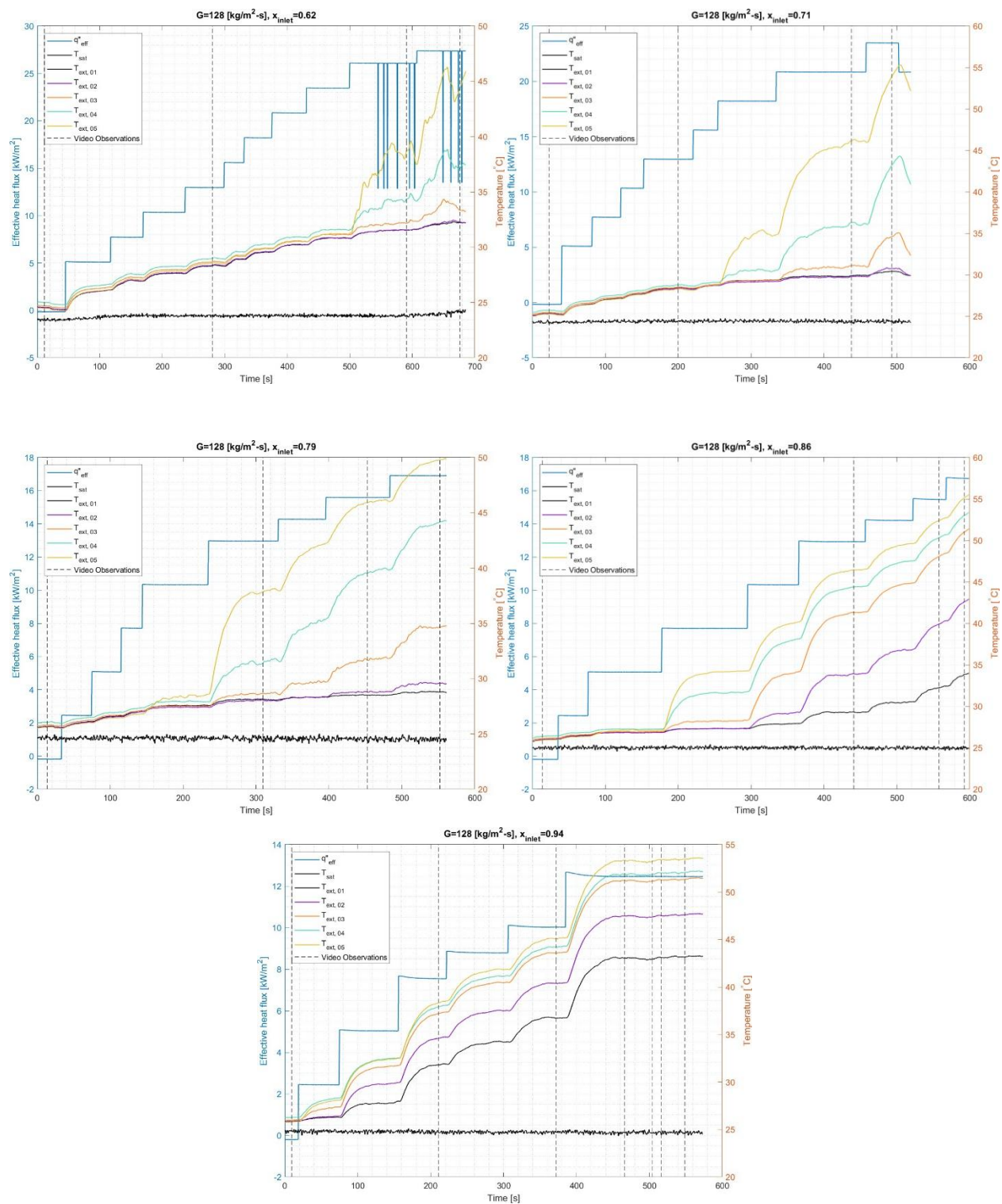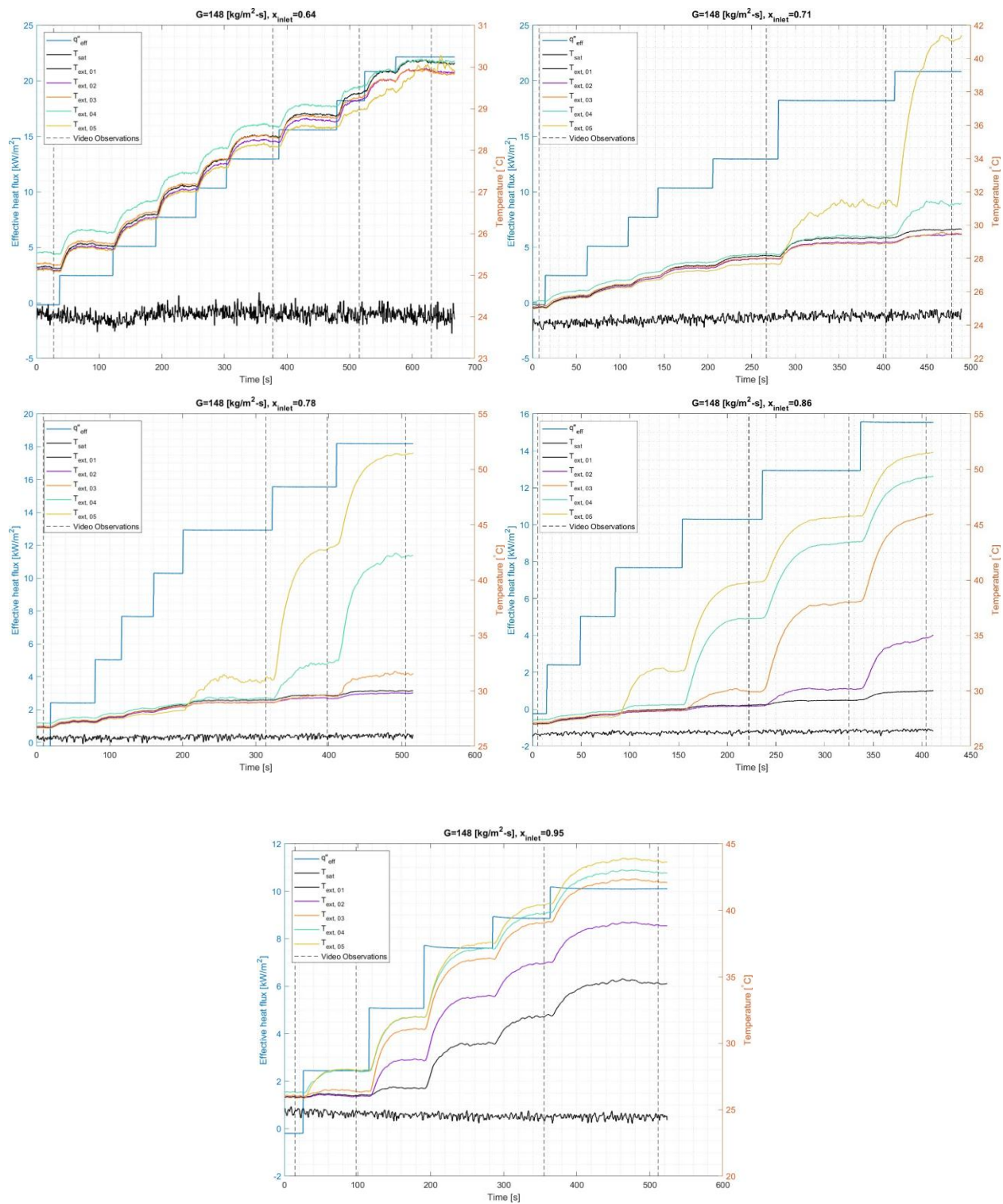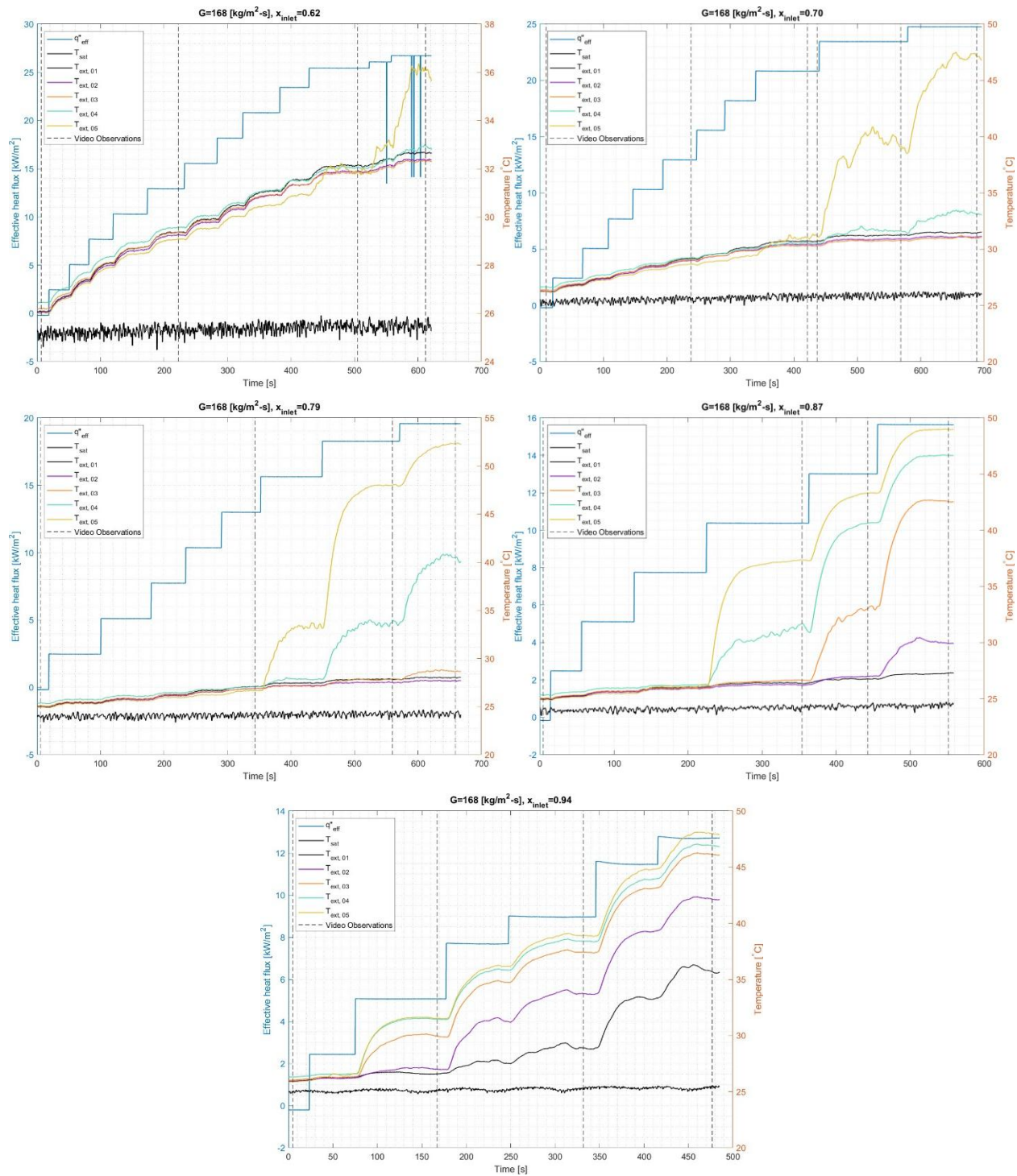
## 2. Small Diameter Obstacle (1.25 mm)

Effective heat flux and temperature versus time for G=148 [kg/m²-s] at various inlet qualities: $x_{inlet}=0.62$, $x_{inlet}=0.70$, $x_{inlet}=0.78$, $x_{inlet}=0.86$, and $x_{inlet}=0.94$.

G=168 [kg/m²-s], x_inlet=0.63



G=168 [kg/m²-s], x_inlet=0.70



G=168 [kg/m²-s], x_inlet=0.78



G=168 [kg/m²-s], x_inlet=0.86



G=168 [kg/m²-s], x_inlet=0.94
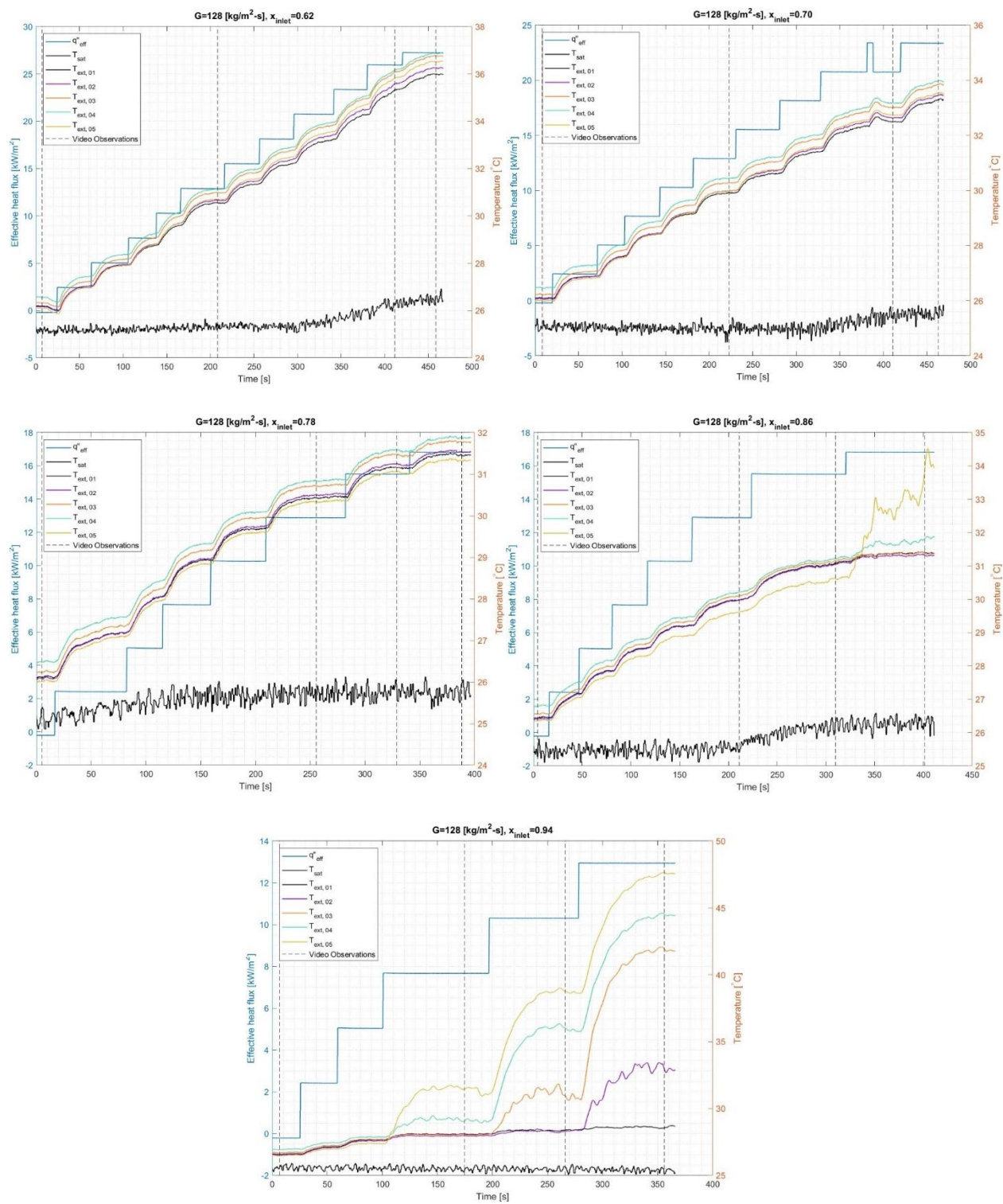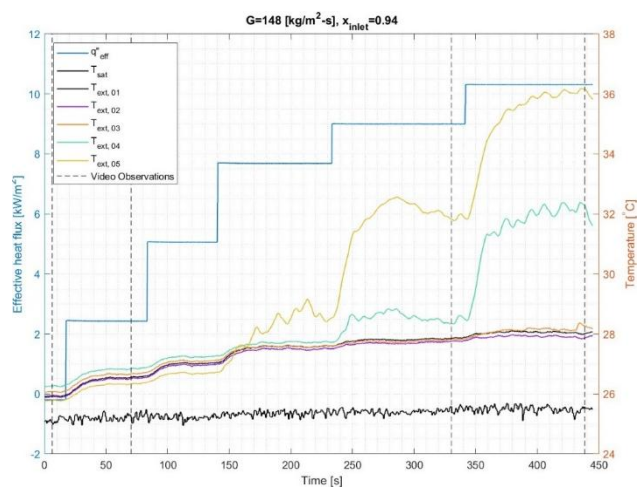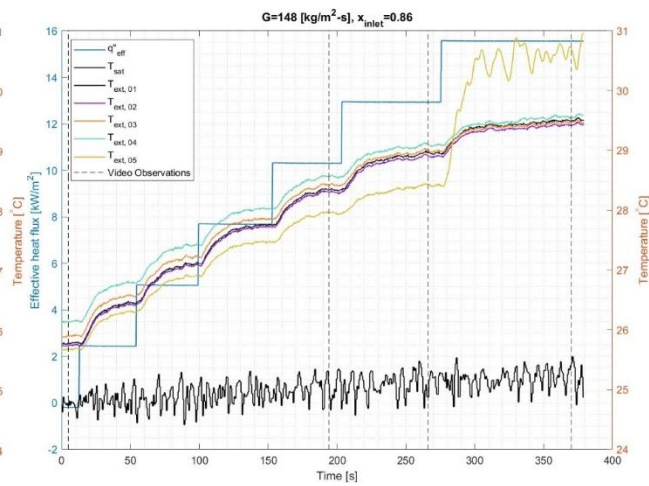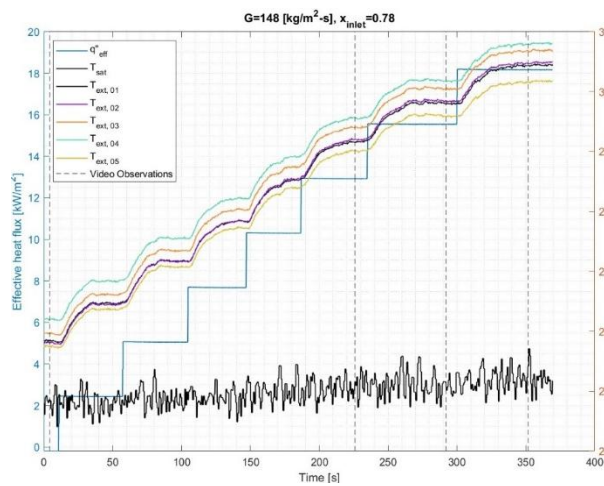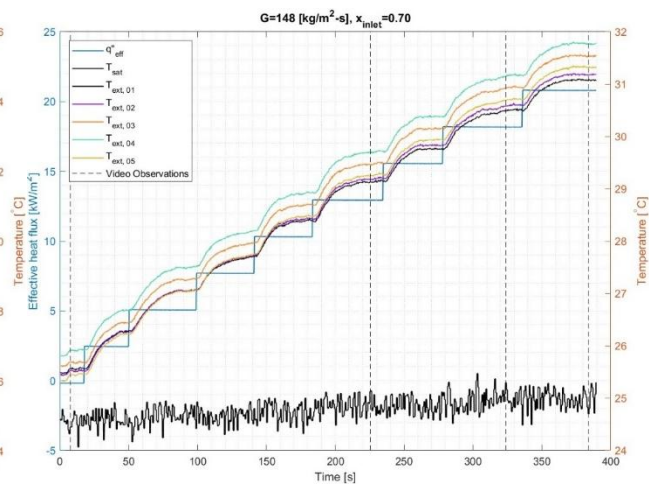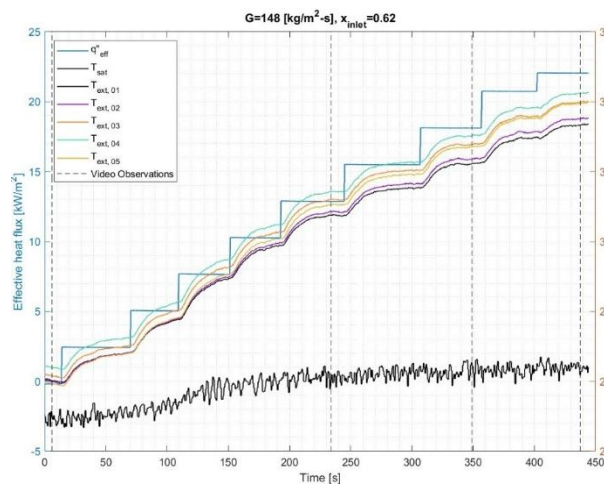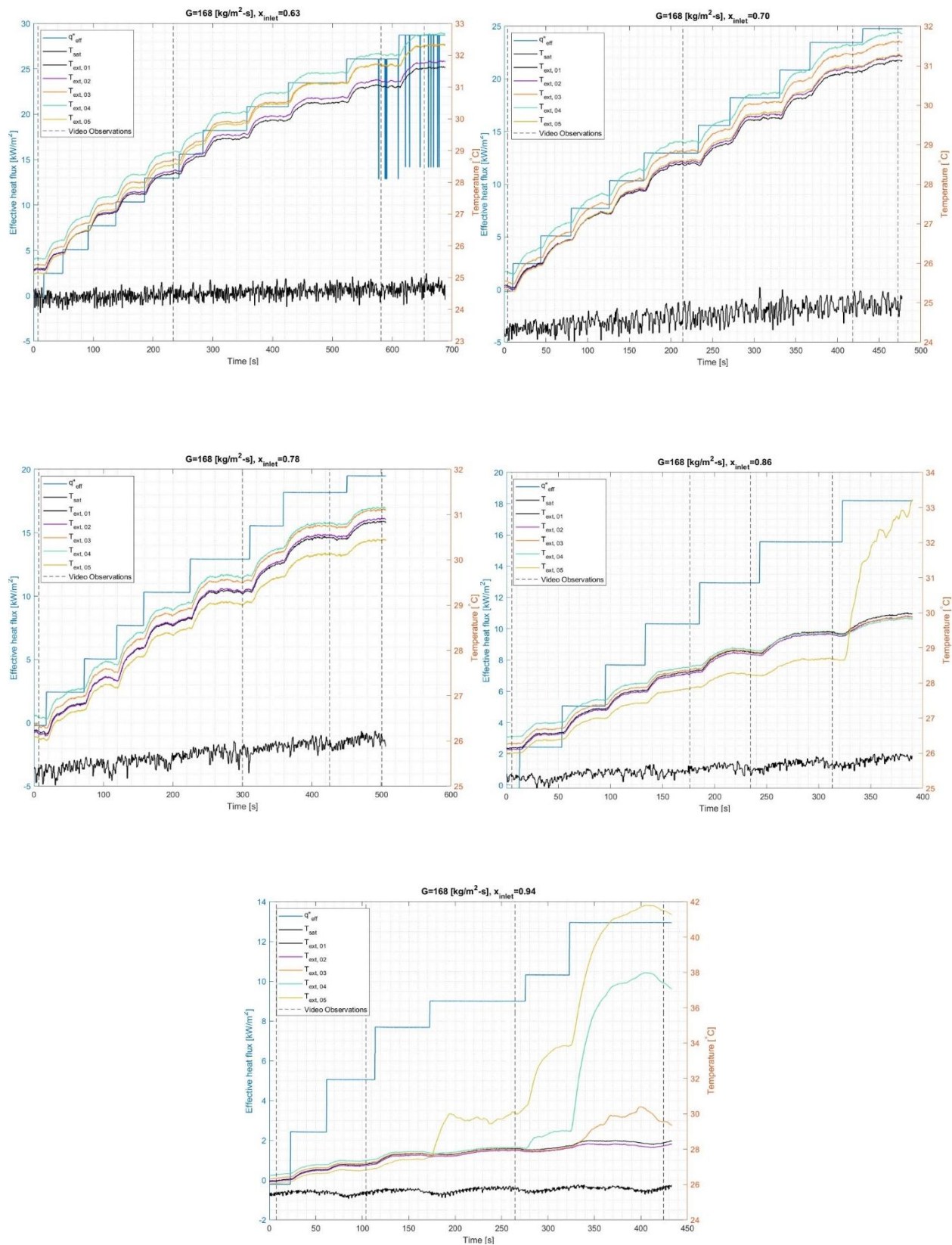
## 3. Nucleate Boiling Conditions, Constant G=130 kg/m²-s vary x$_{in}$, Temperature Time-Trace
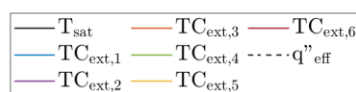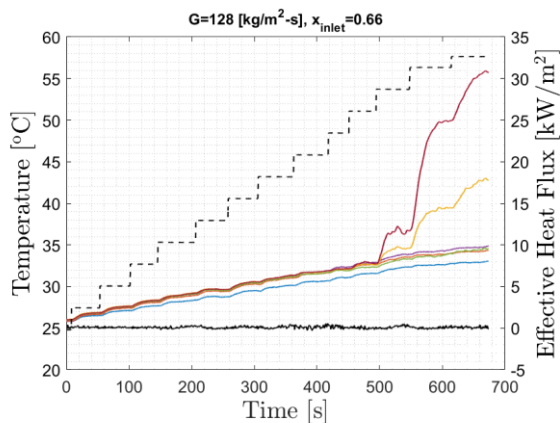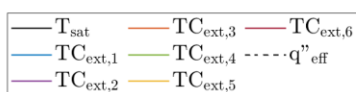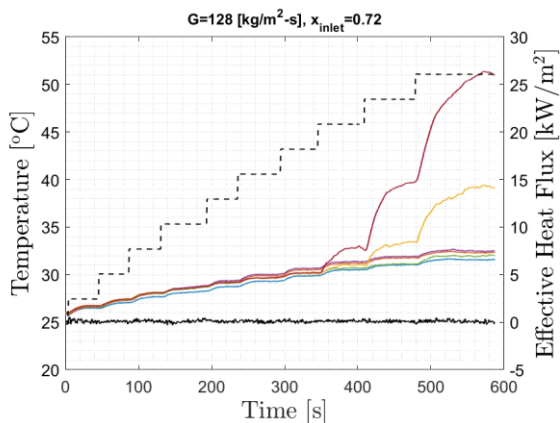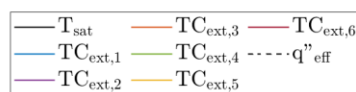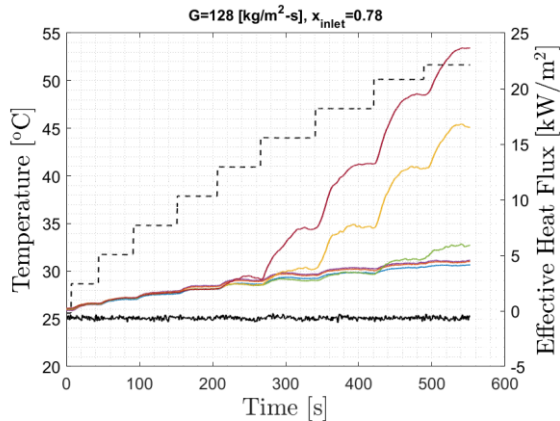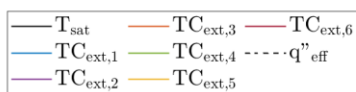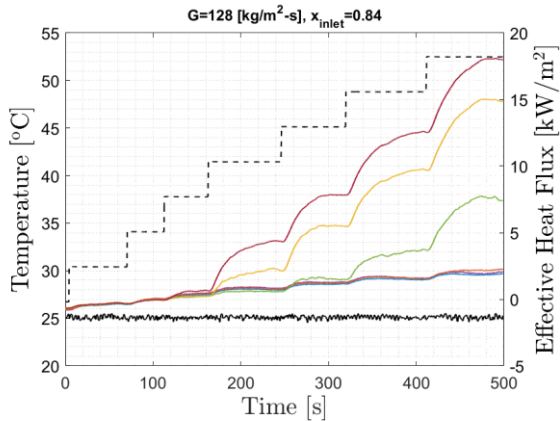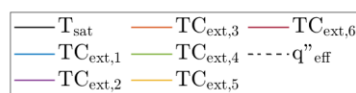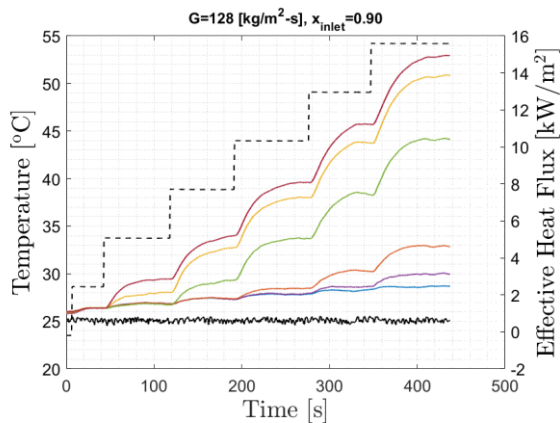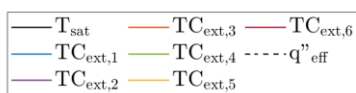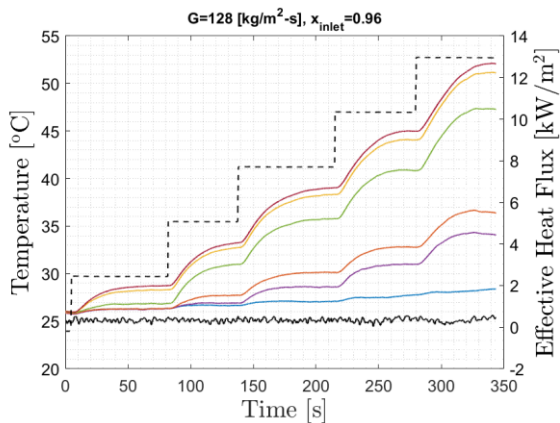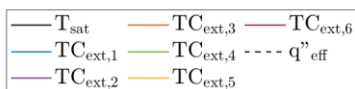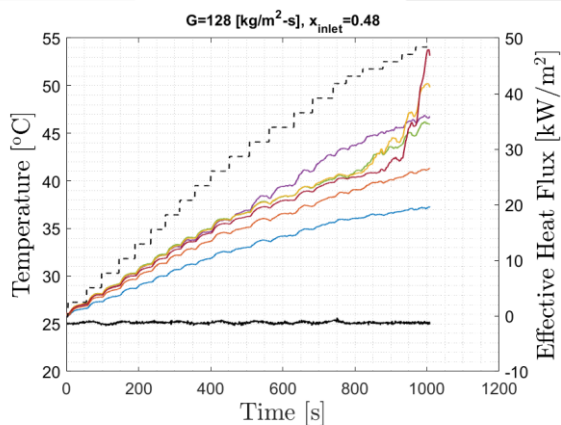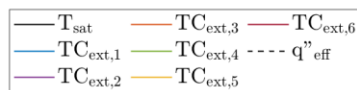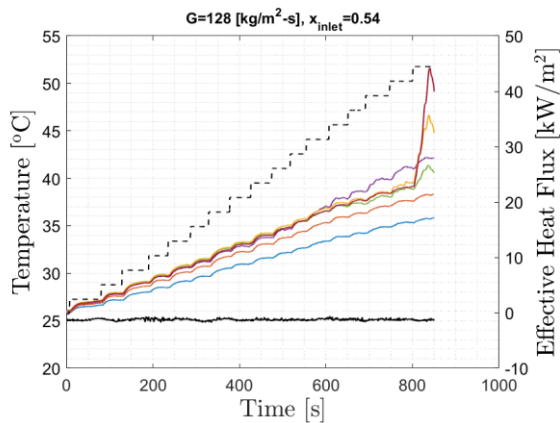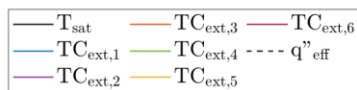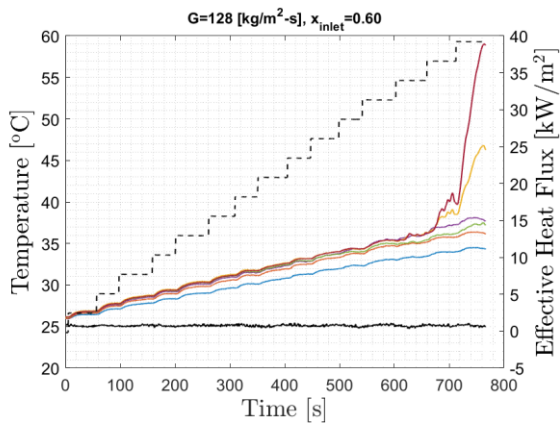
## 4. Nucleate Boiling Conditions, Constant G=140 kg/m$^2$-s vary x$_{in}$, Temperature Time-Trace
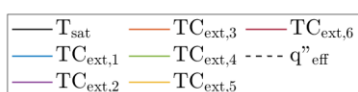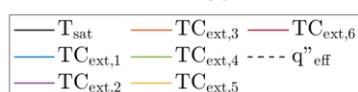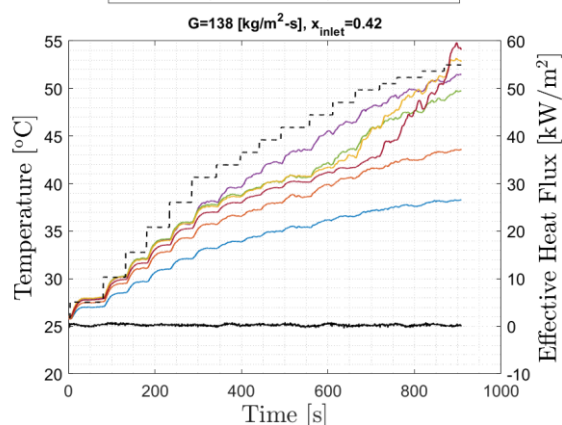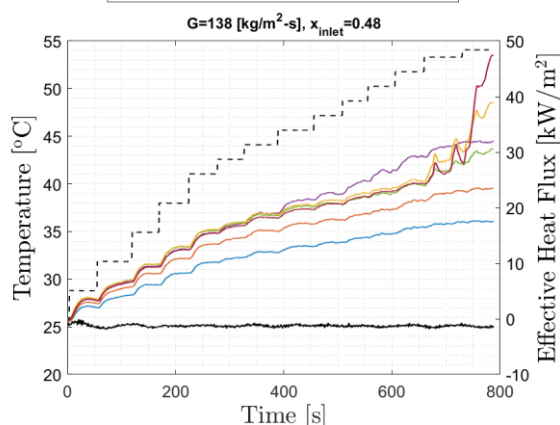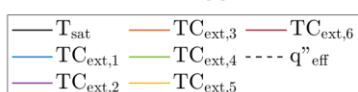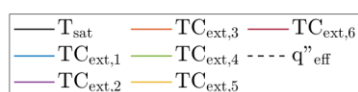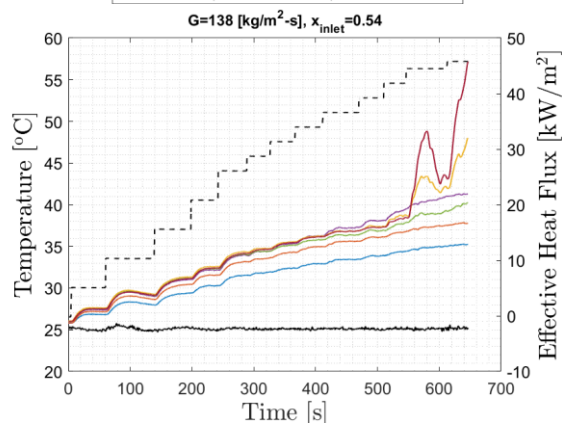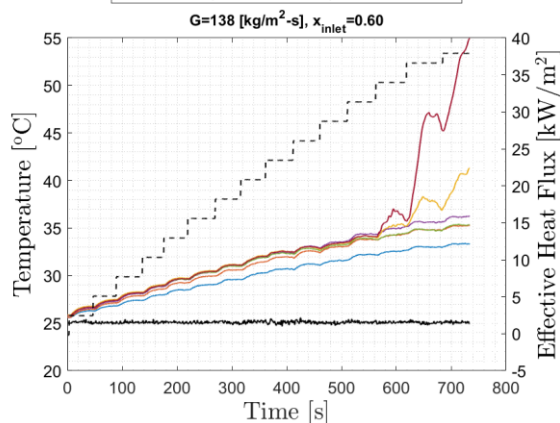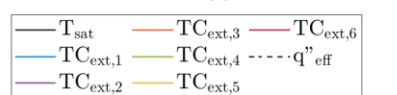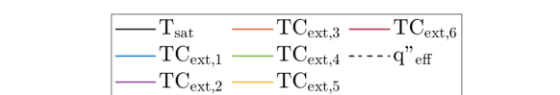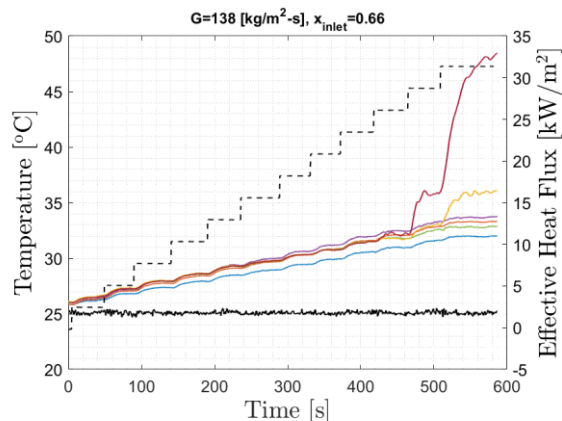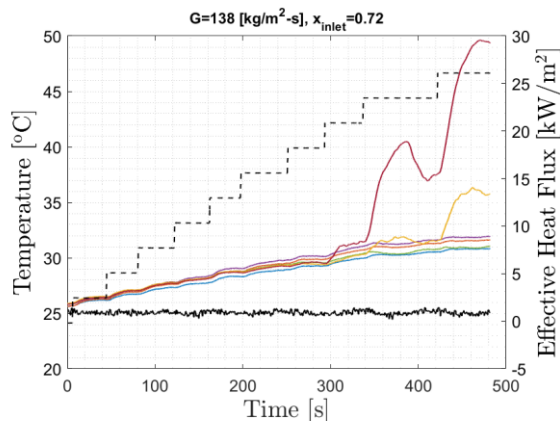
## 5. Nucleate Boiling Conditions, Constant $x_{in}=0.63$ vary G, Temperature Time-Trace
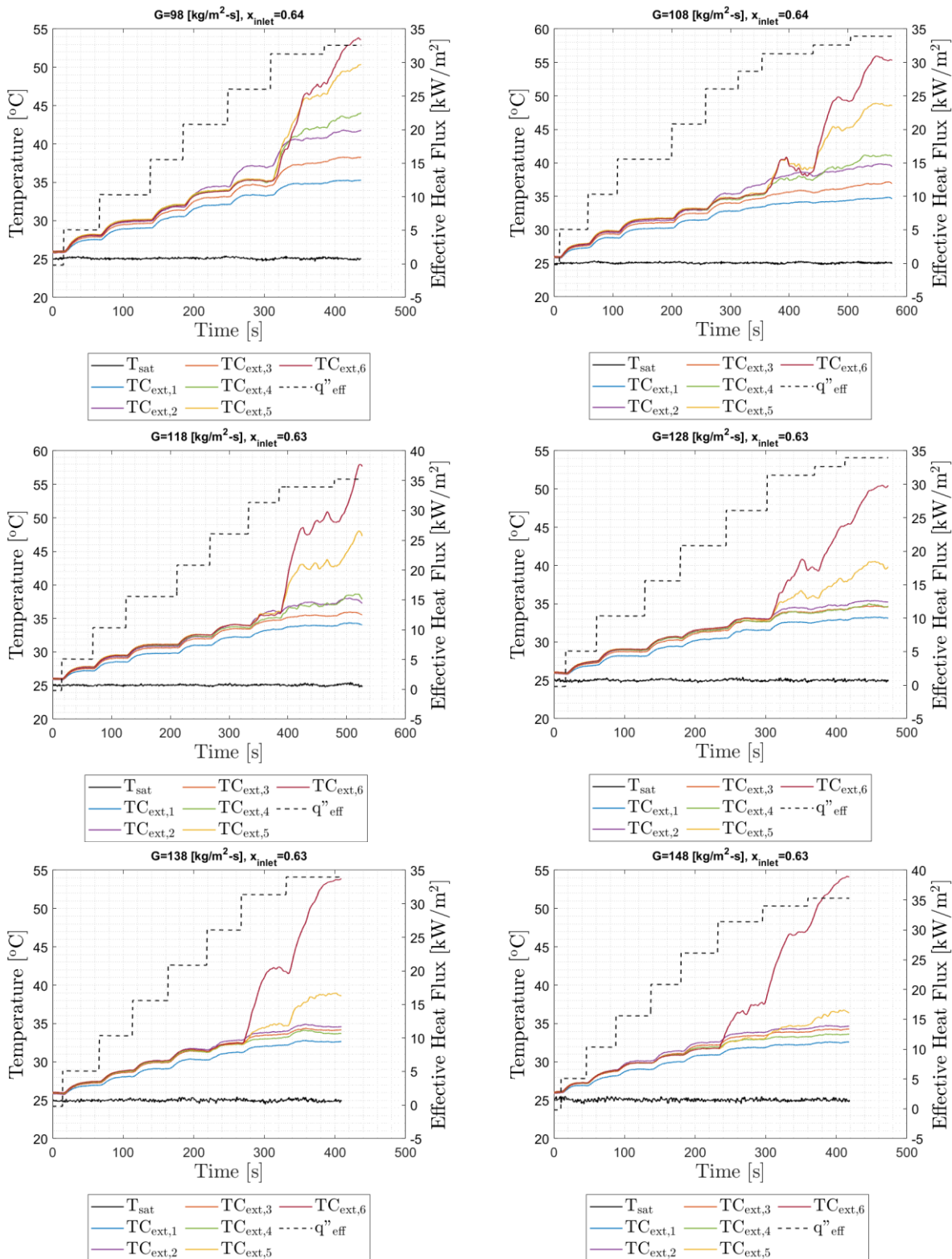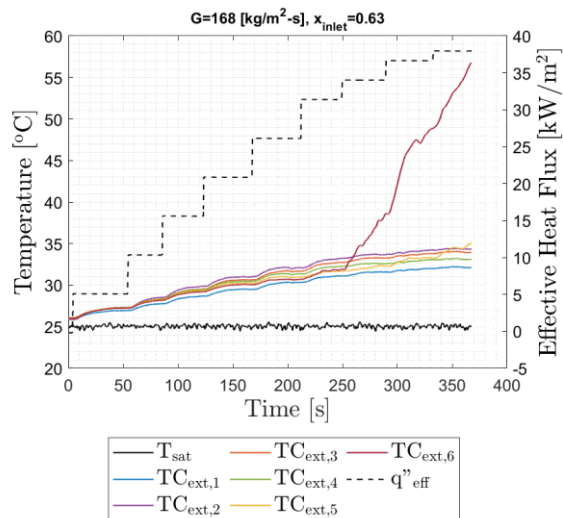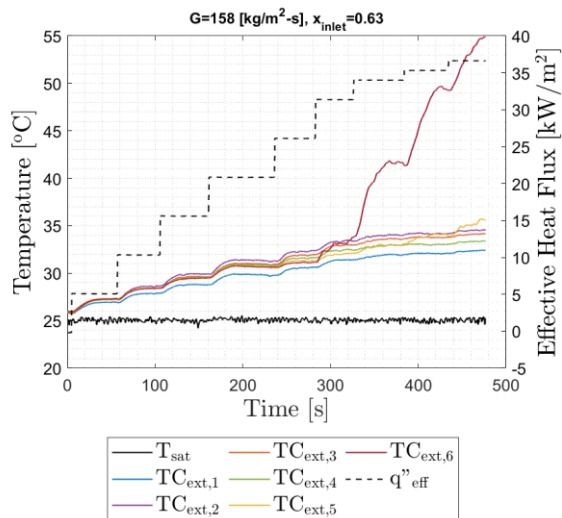
# APPENDIX F: DRYOUT MODELING DATA



Constant G=130 kg/m$^2$-s Varied Inlet Quality



Constant G=140 kg/m$^2$-s Varied Inlet Quality

Constant Inlet Quality x=0.63 Varied Mass Flux
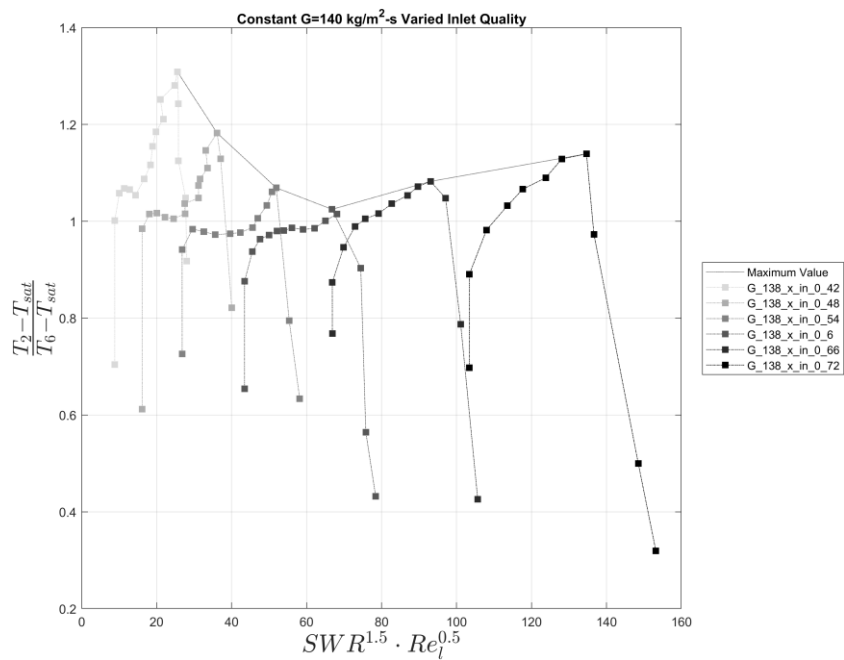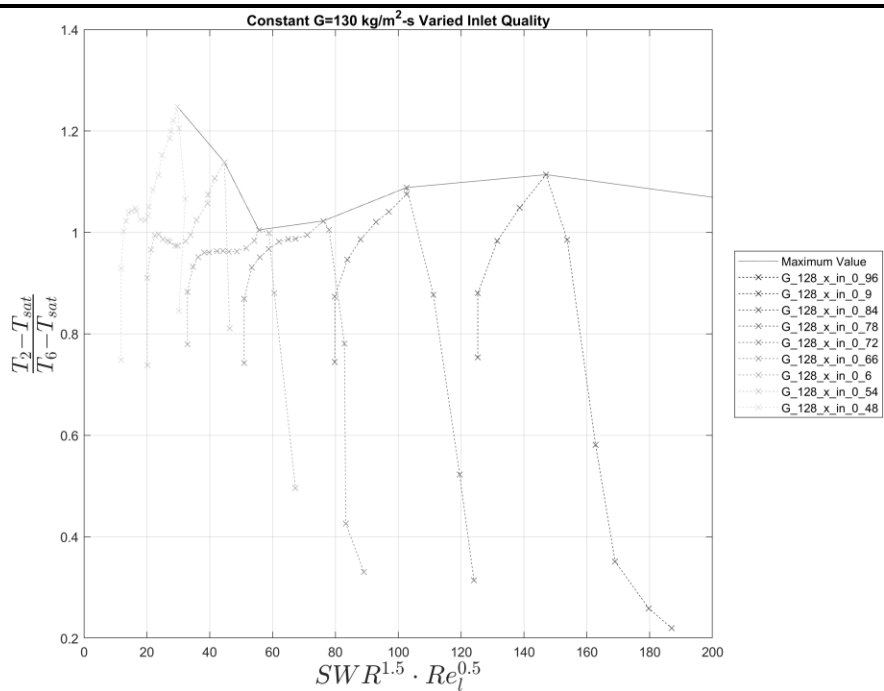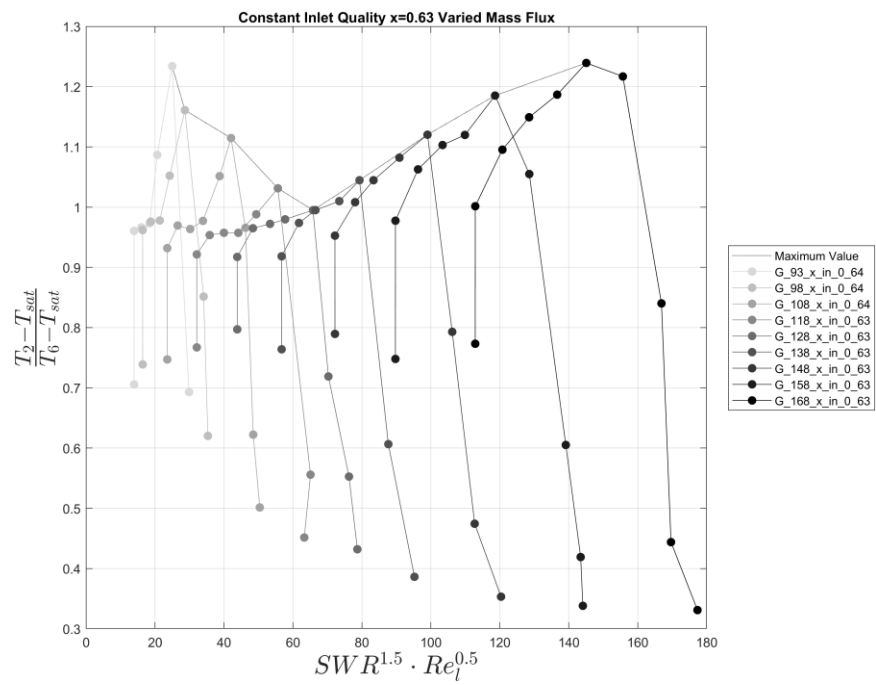
# APPENDIX G: MEASUREMENT TECHNIQUES

## 1. Film Thickness Measurement

All measurements of liquid film thickness were performed using the total internal reflectance method. This non-intrusive, optical measurement has been repeatedly demonstrated to be an effective and accurate way to determine liquid film thickness [2], [4], [45], [46], [93], [94]. Incident light originating from a 10 mW, 632 nm HeNe laser was diffused by tape adhered to the outside of the test section window. With this technique, the light refracts as it moves between the different layers as defined by Snell's law (Fig. 62(a)). At the critical angle, there is total internal reflection at the liquid-vapor interface, resulting in light reflecting towards the light source. The effect creates a ring of light, the radius of which changes with variations in film thickness. A diagram of the light paths can be seen in Fig. 62(a), and an example of the resulting light ring is shown in Fig. 62(b). The light ring was captured using high-speed video, and an edge detection algorithm was used to identify the radius of the ring. These measurements were converted to film thickness using equation (32), where the ring's radius, $R$, was compared to calibration images of the ring's radius as it appeared in a dry test section, $R_{dry}$. $\theta_{crit}$ is the critical angle at the refrigerant liquid-vapor interface in the flow as calculated through Snell's law. Finally, a conversion factor, $c_{pixel}$, was used to convert the measurement from pixels to microns.

$$\delta = \frac{(R - R_{dry})}{2\tan(\theta_{crit})} c_{pixel} \tag{32}$$
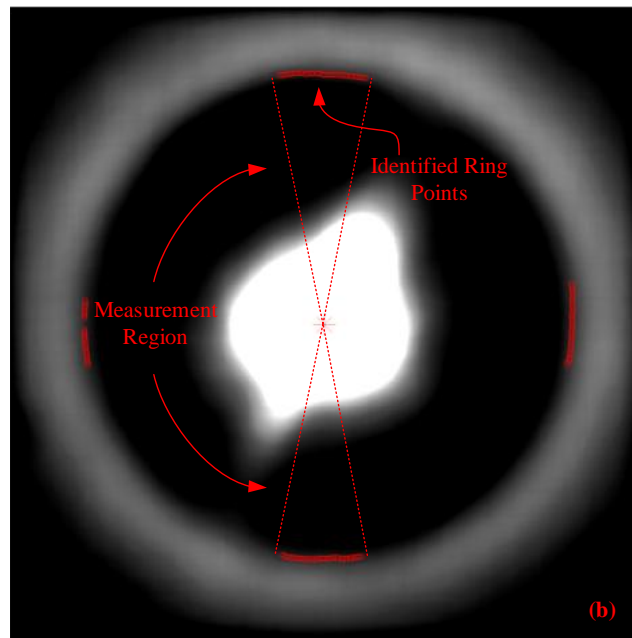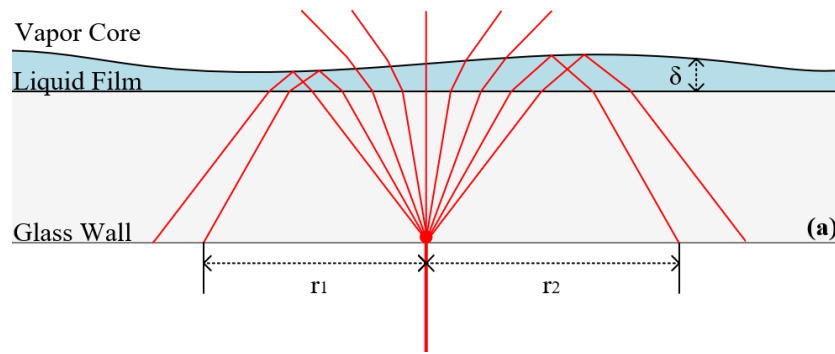
**Fig. 62:** Light paths from a point light source when using the total internal reflectance film thickness measurement technique, adapted from [94], and (b) Edge detection algorithm results for a dry test section ring with measurement region and example identified edge points marked.

In past work, an average radius was used to determine film thickness, assuming the film does not change significantly over the circumference of the ring. In this experiment, the assumption of a uniform film thickness is not obviously valid due to the obstacle, particularly if the ring passes in and out of the wake. To combat this, only a subsection from the top and bottom of the ring was used to determine film thickness. More explicitly, the ring detection algorithm identifies radii within a ±10° range centered on the top and bottom of the light ring. An example of one frame of edge detection can be seen in Fig. 62(b). All reported film thickness values are

then averaged over the thin band upstream and downstream of the light source. The resulting film thickness is then either reported for each frame captured or averaged over the 4000 frames of data gathered for each measurement.

Film thickness measurements for the large obstruction were centered 17.5 mm downstream of the obstruction, which equates to 7 large obstruction diameters. The measurements were taken 15 mm downstream, corresponding to 12 small obstruction diameters, for the small obstruction. The downstream measurement location was determined based on the observed distance required for any recirculation in the immediate wake to decay. Upstream film thickness measurements were consistently taken at a location centered approximately 17 mm upstream of the obstructions.

## 2. High-Speed Video

Optical film thickness measurements and observations of liquid film behavior downstream of the obstruction were recorded using a Phantom VEO-E 340L high-speed camera equipped with a Nikon AF FX Micro-NIKKOR 200mm f/4D lens. All recordings were taken at 2000 frames per second, 300 μs exposure, and a resolution of 1920x800 unless otherwise stated. The high-speed video captured the light ring for film thickness measurements, the behavior of the wake immediately downstream of the obstruction, and the dryout behavior far downstream of the obstruction.

The dry wake widths presented were manually measured from time-averaged images. To obtain these, eight consecutive high-speed images from each image set were averaged. Including more images to the average blurs the dry-wet interface of the wake region. This is mainly due to the oscillatory movement of the dry region border. As disturbance waves pass, the dry border recedes, reducing the dry region area and vice versa.

## 3. Temperature Measurements

Type-E 30-gauge thermocouple (TC) sensors were calibrated using a Pt100 resistance temperature detector and surface mounted to the exterior wall of the test section using Kapton (polyimide) tape. The thermocouples are horizontally centered on the wall and evenly spaced 1 cm apart vertically beginning 4 cm downstream of the obstruction, as shown in Fig. 63. Each thermocouple is numbered, which is used to refer to different downstream locations in the results sections.
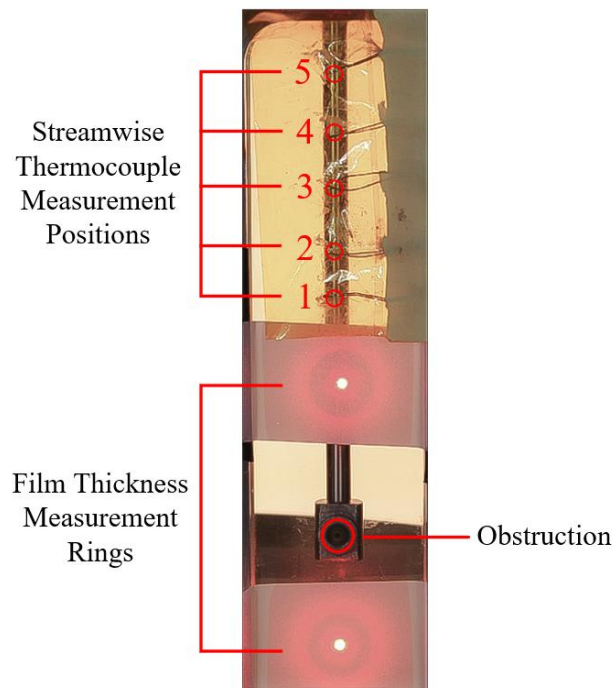


**Fig. 63:** Film thickness measurements and wake region external wall temperature sensors

# APPENDIX H: ADDITIONAL LINKS AND PROGRAMS

List of Videos (Videos may be found at the LET+S website https://lets.engr.wisc.edu)

- SmallObstructionCloseup - This video shows a closeup of the recirculation region that forms behind the small obstruction. The recirculation region seen here can be contrasted with the recirculation region that forms behind the large obstruction. The video was taken at 3600 fps with a 20 fps playback. The flow conditions are G=170 kg/m^2-s, x_in=0.63, Q = 0 W.Recirculation region of large obstruction

- LargeObstructionCloseup - Similar to the small obstruction video, this video shows the recirculation region that forms behind the large obstruction. The video was taken at 3600 fps with a 20 fps playback. The flow conditions are G=170 kg/m^2-s, x_in=0.63, Q = 0 W.

- Disturbance Waves Annotated - This video shows the flow downstream of the obstruction while highlighting disturbance waves. The lines moving up the video mark the back of the disturbance waves as they can be hard to differentiate from the rest of the flow. Disturbance waves have been shown to control the critical heat flux.

- LargeObstructionUnedited - This is an unedited video of the downstream wake behind the large diameter obstruction. This video particularly shows the shape and movement of the dry wake that forms behind the obstruction. The video was taken at 2000 fps with a 20 fps playback. The flow conditions are G=150 kg/m^2-s, x_in = 0.80, and Q = 350W.

- Whirlpool – This video shows the recirculation pattern for a thick film at $G=140$ kg/m$^2$-s, $x_{in}=0.45$, and $q=0$ W/m$^2$ captured at 2100 fps with 10 fps playback. A whirlpool structure forms and is highlighted.

- Droplet deposition induced bubble growth – This video shows a flow at $G=175$ kg/m$^2$-s, $x_{in}=0.342$, and $q=52.9$ kW/m$^2$ taken at 4000 fps with 1 fps playback. It shows the path of an entrained liquid droplet as it impacts the liquid film, entrapping vapor and leading to bubble growth.

- Wake boiling – This video shows a flow at $G=100$ kg/m$^2$-s, $x_{in}=0.63$, and $q=21.1$ kW/m$^2$ taken at 2100 fps with 10 fps playback. It highlights bubble growth in the wake of the obstruction.

- Wave nucleate boiling – This video shows a flow at $G=176$ kg/m$^2$-s, $x_{in}=0.342$, $q=63,492$ kW/m$^2$ captured at 4000 fps with 10 fps playback. It circles three active nucleation cavities just upstream of the obstruction and clearly demonstrates the oscillation of state during the passage of a disturbance wave.

- Dual Dryout – This video shows a flow at $G=140$ kg/m$^2$-s, $x_{in}=0.55$, $q=45.0$ kW/m$^2$ captured at 5200 fps with 20 fps playback. It shows the entire obstruction wake with the location of all thermocouples as well as the regions of the flow as diagramed in Fig. 4. This video was taken simultaneously with Upstream Dryout.

- Upstream Dryout – This video shows a flow at $G=140$ kg/m$^2$-s, $x_{in}=0.55$, $q=45.0$ kW/m$^2$ captured at 2100 fps with 10 fps playback. It focuses on the upstream dryout region and was taken simultaneously with Dual Dryout.

An example of the film thickness processing code may also be found at the link above.